

INTEGRATION OF MULTI-FUNCTIONAL OXIDE THIN FILM
HETEROSTRUCTURES WITH III-V SEMICONDUCTORS

by

Md Shafiqur Rahman, B.S, M.S.

A dissertation submitted to the Graduate Council of
Texas State University in partial fulfillment
of the requirements for the degree of
Doctor of Philosophy
with a Major in Materials Science, Engineering, and Commercialization
May 2017

Committee Members:

Ravi Droopad, Chair

R. K. Pandey

Clois E. Powell

Maggie Chen

Tom Zirkle

COPYRIGHT

by

Md Shafiqur Rahman

2017

FAIR USE AND AUTHOR'S PERMISSION STATEMENT

Fair Use

This work is protected by the Copyright Laws of the United States (Public Law 94-553, section 107). Consistent with fair use as defined in the Copyright Laws, brief quotations from this material are allowed with proper acknowledgement. Use of this material for financial gain without the author's express written permission is not allowed.

Duplication Permission

As the copyright holder of this work I, Md Shafiqur Rahman, authorize duplication of this work, in whole or in part, for educational or scholarly purposes only.

DEDICATION

I would like to dedicate this dissertation to my mother and to my late father for all the guidance, encouragement and hard work since I was young.

ACKNOWLEDGEMENTS

I would like to express my sincere gratitude to my supervisor Dr. Ravi Droopad for his support and supervision throughout my PhD degree, providing an excellent lab facility and freedom to work on different topic of my own research interest. His proper guidance benefited me in several ways such as the direct help to solve many problems, correction of my papers and thesis.

I would especially like to appreciate the guidance and support from Dr. Juan Salvador (post-doctoral scientists of Droopad's research lab) for training me on the use of the MBE system for the epitaxial growth of STO on GaAs substrate. I appreciate his commitment to solving scientific challenges for epitaxial growth of III-V semiconductors. A special thank also goes to Nate England and Dr. Casey Smith for their training and assistance on various measurements and processes.

I also want to acknowledge the help from various colleagues from Droopad's research lab. Susmita Ghose and Dr. Javad Gattabi often assistance with various measurement and data analysis. In particular, Susmita's contribution in the measurement and analysis of the XPS spectra is greatly appreciated. I am thankful to Dr. Robert Klie and Liang Hong from University of Illinois for providing TEM support.

On the financial side, the support from Materials Science, Engineering & Commercialization (MSEC) program and doctoral research support fellowship from Texas State University is gratefully acknowledged. I also want to acknowledge my dissertation committee members for their valuable suggestions.

TABLE OF CONTENTS

	Page
ACKNOWLEDGEMENTS.....	v
LIST OF FIGURES	viii
ABSTRACT.....	xiii
CHAPTER	
I. INTRODUCTION.....	1
1.1 Literature Review.....	5
1.1.1 Multiferroic Property	5
1.1.2 Magnetoelectric Effect.....	6
1.1.3 Single Phase Multiferroic Materials	8
1.1.4 Exchange Bias.....	13
II. CRYSTALLINE FUNCTIONAL OXIDE GROWTH AND CHARACTERIZATION TECHNIQUES	18
2.1 Introduction.....	18
2.2 Molecular Beam Epitaxy	19
2.3 Pulsed Laser Deposition	25
2.4 Laser Materials Interactions.....	29
2.5 Structural Characterization	32
2.5.1 X-Ray Diffraction	33
2.5.2 Scanning Electron Microscopy	35
2.5.3 X-ray Photoelectron Spectroscopy	38
2.5.4 Atomic Force Microscopy	41
2.6 Electrical Characterization.....	43
2.6.1 C-V and Dielectric Measurement	43
2.6.2 Ferroelectric Characterization.....	45
2.6.3 Piezo-response Force Microscopy	46
2.7 Magnetic Characterization	47
2.7.1 Vibrating Sample Magnetometer	47

III. GROWTH AND CHARACTERIZATION OF STO ON GaAs AND BiFeO ₃ THIN FILMS ON STO/GaAs.....	50
3.1 Introduction.....	50
3.2 Growing SrTiO ₃ on GaAs (001) by Molecular Beam Epitaxy.....	52
3.2.1 Experiment.....	53
3.2.2 Results and Discussion	55
3.3 Experimental Design and Characterization of BFO Growth	57
3.4 Result and Discussion.....	58
3.5 Conclusion	70
IV. BiFeO ₃ /La _{0.7} Sr _{0.3} MnO ₃ HETEROSTRUCTURES WITH III-V SEMICONDUCTOR	71
4.1 Introduction.....	71
4.2 Experimental.....	73
4.2.1 Thin Film Deposition and Device Fabrication.....	73
4.2.2 Characterizations.....	74
4.3 Results and Discussions.....	76
V. BiFeO ₃ /La _{0.7} Sr _{0.3} MnO ₃ SUPERLATTICES FOR ENHANCED INTERFACE INDUCED PROPERTIES	89
5.1 Introduction.....	89
5.2 Experimental.....	91
5.3 Results and Discussion	93
5.4 Resistive Switching in BFO/LSMO Superlattices	98
5.4.1 Electrical Characterization.....	99
VI. CONCLUSION AND FUTURE WORK.....	104
6.1 Conclusion	104
6.2 Contributions of This Work.....	104
6.3 Future Work	105
REFERENCES	109

LIST OF FIGURES

Figure	Page
1.1: Illustrating the inter-connection between applied forces (electric field E, magnetic field H, and stress σ) and associated material properties (electric polarization P, magnetization M, and strain ϵ).	2
1.2: Arrangement of oxides: The biggest circle denotes different types of oxides, some of which represent electrically (green ellipse) and others illustrate magnetically switchable materials (orange ellipse).	3
1.3: Number of papers from 1950-2008 using magnetoelectrics or multiferroics as keywords [24]	9
1.4: (a) Schematics of BFO crystal orientation	10
1.5: Schematic representation of ferroelectric polarization [111] direction perpendicularly to the G-type antiferromagnetic plane of BFO	11
1.6: Effects of parasitic or secondary phases on BiFeO ₃ epitaxial thin films [36]	12
1.7: The interfacial effects due to coupling between AFM-FM systems are depicted in which the hysteresis loop undergoes a shift when field cooled.....	13
1.8: Schematic of a simple model to describe exchange bias along with interface spin structure and the effect on the magnetic hysteresis curve is presented.....	15
2.1: (a) Schematic of an oxide molecular beam epitaxy system [64]	23
2.1: (b) Oxide molecular beam epitaxy system connected to the clyster system through buffer line at advanced functional materials laboratory of Texas State University	24
2.2: (a) Schematic of a basic pulsed laser deposition system [69].....	26
2.2: (b) Pulsed laser deposition system installed at Texas State University	27

2.3: Schematic of the energetic plasma plume [74].....	30
2.4: Schematic illustration of the shape of a plasma plume created by pulsed laser deposition.....	32
2.5: Schematic diagram of the geometries of thin film X-ray diffraction measurement, showing relations between the lattice planes of a thin film sample and X-ray geometries [76]-[78].....	34
2.6: The state of the art in highly automated, fully modular, multipurpose Rigaku SmartLab X-ray Diffractometer of Texas State University	34
2.7: (a) Schematic scanning electron microscope overview [82]	36
2.7: (b) Helios NanoLab 400 for Scanning Electron Microscope imaging	37
2.8: (a) Schematic drawing of a typical XPS setup with different photon source such as X-rays, UV-light, laser and Synchrotron radiation, a sample manipulation with different linear and rotational degrees of freedom, electron optics, an energy dispersive analyzer and a detector.....	39
2.8: (b) X-ray photoelectron spectroscopy from SPECS Surface Nano Analysis	40
2.9: (a) Typical schematics of atomic force microscope for working in different modes [92].....	42
2.9: (b) Park XE7 atomic force microscope which is the most affordable research grade AFM with flexible sample handling	43
2.10: (a) Semiconductor device analyzer of Keysight B1500A with multi-probe station, an all in one analyzer supporting IV, CV, pulse/dynamic IV which is designed for all-round characterization from basic to cutting-edge applications	44
2.10: (b) Precision impedance analyzers 6500B from Wayne Kerr electronics	45
2.11: (a) A typical ferroelectric hysteresis loop showing the spontaneous polarization (P_s), the remnant polarization (P_r) and the coercive field (E_c) [95].....	46

2.11: (b) Precision LC II ferroelectric test system from Radiant technologies inc.....	46
2.12: Depiction of PFM operation.....	47
2.13: (a) Typical schematic of vibrating sample magnetometer [98].....	48
2.13: (b) Physical Prosperities Measurement System (PPMS) from quantum design	49
3.1: (a) RHEED patterns along GaAs [110] and [010] azimuth for c(4x4) As stabilized GaAs surface. (b) RHEED patterns along GaAs [-110] and [110] azimuth for (2x4) As stabilized GaAs surface. (c and d) RHEED pattern shows surface reconstruction changed to a (2x1) after the deposition of the Ti pre-layer along the [-110] and [110] for c(4x4) and (2x4) GaAs surface respectively. (e and f) RHEED pattern shows surface reconstruction changed to a (2x2) after the deposition of the Sr pre-layer along the [-110] and [110] for c(4x4) and (2x4) GaAs surface respectively.....	55
3.2: RHEED patterns along the [110] and the [010] respectively after the deposition of 100Å STO	56
3.3: XRD theta-2theta scan of the STO on GaAs showing (001) oriented oxide film.....	57
3.4: XRD pattern of BFO films grown on STO buffered GaAs.	59
3.5: XPS survey spectrum performed on a BFO film.....	60
3.6: High resolution spectrum of Bi 4f core level of BFO films	61
3.7: High resolution spectrum of Fe 2p core level of BFO films	62
3.8: High resolution spectrum of O 1s core level of BFO films	63
3.9: 12 x 12 μm ² micrographs showing (a) topography, (b) PFM out-of-plane phase, and (c) out-of-plane amplitude of BFO thin film	64
3.10: (a) Ferroelectric and (b) magnetic hysteresis loop measured at room temperature for the BiFeO ₃ thin film.....	65

3.11: The measured and fitted ellipsometric spectra for the BFO film	68
3.12: Plots of $(\alpha^*E)^2$ vs photon energy E for the BFO thin film	69
4.1: Shows the typical θ - 2θ XRD pattern BFO/LSMO/5 nm STO/GaAs sample which indicating high quality, single phase (00l) oriented oxide films.	76
4.2: (a) Bright field cross-section TEM image of BFO/LSMO/STO /GaAs heterostructure. (b) HRTEM image of LSMO/STO /Ga ₂ O ₃ /GaAs interface. (c) HRTEM image of BFO (10 nm)/LSMO (90 nm) interface and (d) shows the HRTEM of LSMO/STO/Ga ₂ O ₃ interface.....	78
4.3: Ferroelectric domain switching observation of BFO/LSMO/STO /GaAs heterostructure	79
4.4: M-T curves of BFO/LSMO/STO/GaAs heterostructure	80
4.5: (a) Magnetic hysteresis curves measured on BFO/LSMO/STO /GaAs heterostructure after cooling the sample under ± 2000 Oe at 4K.....	82
4.6: (a) Current-voltage switching characteristics for 10 nm BFO deposited on 6 nm, 18 nm and 60 nm of LSMO.....	84
4.7: (a) Cross-sectional schematic illustration of the device. (b) Schematic diagram of a simplified model for the field effect in a p-type ferroelectric FET	87
4.8: (a) DC output I-V curves. (b) Transfer characteristics of the device	87
5.1: The sketch of the formula of BFO/LSMO superlattice structure. (a) BFO/LSMO superlattice with 16 stacking period with thicknesses of BFO=4.8 nm and LSMO=6.6 nm, (b) BFO/LSMO superlattice with 64 stacking period with thicknesses of BFO=1.2 nm and LSMO=1.6 nm respectively	92
5.2: (a) Typical X-ray diffraction pattern of the as-grown BFO/LSMO superlattices deposited on STO (001) buffered GaAs (001) substrates with a same total deposition time but different N and (b) shows the rocking curve of superlattices with N=1, 4 and 16 around (001) plane.....	93

5.3: (a) Magnetic moment vs field hysteresis loop for BFO/LSMO superlattices with zero field cooling and (b) Zero field cooled and field cooled magnetic moment vs temperature curves for various superlattices.....	95
5.3: Magnetic moment vs field hysteresis loop for BFO/LSMO superlattices during field cooling with (c) +1 Tesla and (d) -1 Tesla.....	96
5.4: Magnetic hysteresis loop shifting or exchange bias for BFO/LSMO superlattices with (a) N=2, (b) N=4, (c) N=8, (d) N=16, (e) N=32 stacking period number and (f) shows the amount of exchange bias variation with N	97
5.5: Room temperature bipolar resistive switching characteristics of BFO/LSMO superlattice at (a) linear scale and (b) logarithmic scale.....	100
5.6: Carrier injection mechanism of BFO/LSMO superlattice in logarithmic scales during (a) positive voltage sweep and (b) negative voltage sweep.....	102
6.1: Four approaches used to integrate multifunctional oxide with III-V semiconductor.....	104
6.2: A schematic illustrating the control of magnetization in a ferromagnetic material from the electric control of exchange bias.....	106
6.3: Sketch of a possible MeRAM element where two ferromagnetic layers (FM1 & FM2) are aligned.....	107

ABSTRACT

Integration of multi-functional oxide thin films with semiconductors has attracted considerable attention in recent years due to their potential applications in sensing and logic functionalities that can be incorporated in future system-on-a-chip devices. III-V semiconductor, for example, GaAs, have higher saturated electron velocity and mobility allowing transistors based on GaAs to operate at a much higher frequency with less noise compared to Si. In addition, because of its direct bandgap a number of efficient optical devices are possible and by oxide integrating with other III-V semiconductors the wavelengths can be made tunable through hetero-engineering of the bandgap. This study, based on the use of SrTiO₃ (STO) films grown on GaAs (001) substrates by molecular beam epitaxy (MBE) as an intermediate buffer layer for the hetero-epitaxial growth of ferromagnetic La_{0.7}Sr_{0.3}MnO₃ (LSMO) and room temperature multiferroic BiFeO₃ (BFO) thin films and superlattice structures using pulsed laser deposition (PLD). The properties of the multilayer thin films in terms of growth modes, lattice spacing/strain, interface structures and texture were characterized by the in-situ reflection high energy electron diffraction (RHEED). The crystalline quality and chemical composition of the complex oxide heterostructures were investigated by a combination of X-ray diffraction (XRD) and X-ray photoelectron absorption spectroscopy (XPS). Surface morphology, piezo-response with domain structure, and ferroelectric switching observations were carried out on the thin film samples using a scanning probe microscope operated as a piezoresponse force microscopy (PFM) in the contact mode. The magnetization measurements with field

cooling exhibit a surprising increment in magnetic moment with enhanced magnetic hysteresis squareness. This is the effect of exchange interaction between the antiferromagnetic BFO and the ferromagnetic LSMO at the interface. The integration of BFO materials with LSMO on GaAs substrate also facilitated the demonstration of resistive random access memory (ReRAM) devices which can be faster with lower energy consumption compared to present commercial technologies. Ferroelectric switching observations using piezoresponse force microscopy show polarization switching demonstrating its potential for read-write operation in NVM devices. The ferroelectric and electrical characterization exhibit strong resistive switching with low SET/RESET voltages. Furthermore, a prototypical epitaxial field effect transistor based on multiferroic BFO as the gate dielectric and ferromagnetic LSMO as the conducting channel was also demonstrated. The device exhibits a modulation in channel conductance with high ON/OFF ratio. The measured nanostructure and physical-compositional results from the multilayer are correlated with their corresponding dielectric, piezoelectric, and ferroelectric properties. These results provide an understanding of the heteroepitaxial growth of ferroelectric (FE)-antiferromagnetic (AFM) BFO on ferromagnetic LSMO as a simple thin film or superlattice structure, integrated on STO buffered GaAs (001) with full control over the interface structure at the atomic-scale. This work also represents the first step toward the realization of magnetoelectronic devices integrated with GaAs (001).

I. INTRODUCTION

The motivation for investigating multifunctional materials depends exclusively on the inclination for the miniaturization of devices to perform various tasks simultaneously or being able to interact with external stimuli including magnetic, electrostatic, acoustic and optical. The exploration of multifunctional materials and structures hence has been taken as an indispensable mission in numerous fields such as medical treatment, life sciences, microelectronics, information technology, energy, transportation, computer science, safety engineering and military technologies.

Complex oxide materials are fascinating from a multi-functional standpoint, owing to the fact that they may be able to display a comprehensive extent of functional properties such as ferroelectricity, ferromagnetism and ferroelasticity, and can be varied from metals, insulators, semiconductors or superconductors. Another type of complex oxides exhibiting great potential for spintronics based device applications is known as the so-called multiferroic[1]. By definition, a ferroic material possesses one of the ferroic properties: ferromagnetism, ferroelectricity, or ferroelasticity, while a multiferroic material is able to unfold more than one ferroic properties in the same phase[2]. Moreover, novel applications can also be realized from the coupling between some of these properties.

In order to explain multiferroic materials and to show the routes within an external stimulus, such as magnetic (H), stress (σ) and electric (E) fields with affiliated properties of the material, such as magnetization (M), strain (ϵ) and electrical polarization (P), a well-known triangle could be used shown in figure 1.1. A ferroelastic, ferroelectric, or magnetic ferroic material exhibits spontaneous strain, polarization, or magnetization which can be hysteretically switched by external stress, electric field, or magnetic field, respectively.

Additional interactions also arise in multiferroics by coupling between simultaneous ferromagnetic and ferroelectric domains or spins by magnetoelectric (ME) effect. These materials also known as magneto-electric multiferroics, where electric polarization can be persuaded by an applied magnetic field, on the other hand magnetization can also be introduced by an applied electric field[2], [3].

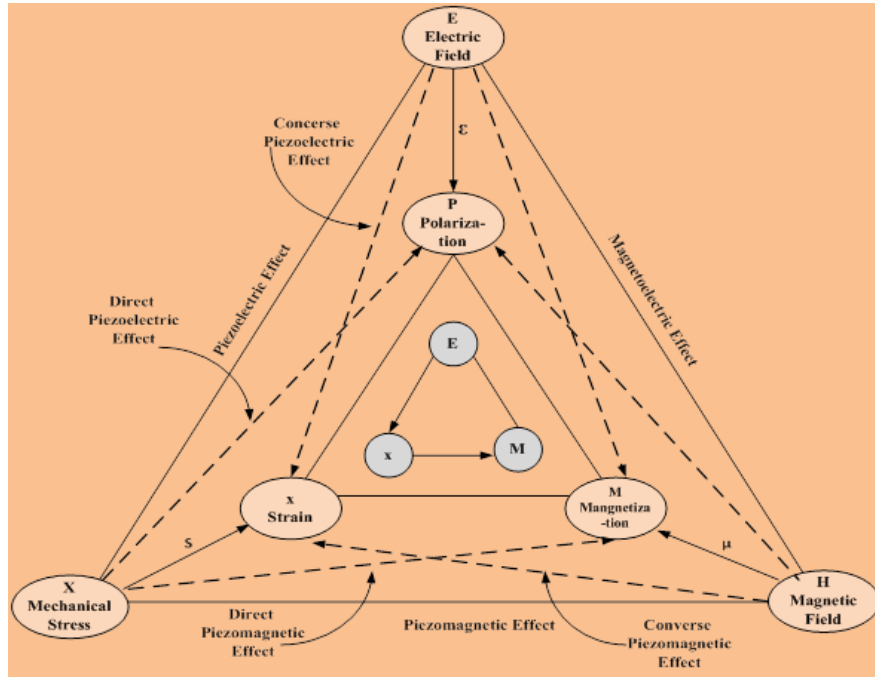


Figure 1.1: Illustrating the inter-connection between applied forces (electric field E , magnetic field H , and stress σ) and associated material properties (electric polarization P , magnetization M , and strain ϵ). The coupling coefficients within internal material properties and external applied forces, e.g. magnetic susceptibility (χ_M), electric susceptibility (χ_E) and compliance tensor (S) are also shown[3].

It should be mentioned that not all ferromagnetic-ferroelectric multiferroics exhibit ME coupling[4]. Besides, existence of ME coupling is not only limited to material with ferromagnetic and ferroelectric ordering, but may also exists in any electric and magnetic field dependent polarizable material[2], [4]. Figure 1.2 demonstrate a relevance between multiferroic and ME oxides. Multiferroic materials with switchable spontaneous

polarization and strain (ferroelectric-ferroelastics) are extensively implemented in transducers based on piezoelectricity. Similarly, materials presenting direct coupling within switchable spontaneous magnetization and strain (ferromagnetic-ferroelastics) are used in magneto-mechanical actuators[5]. Multiferroics with ME coupling ability further demonstrates significant promise for

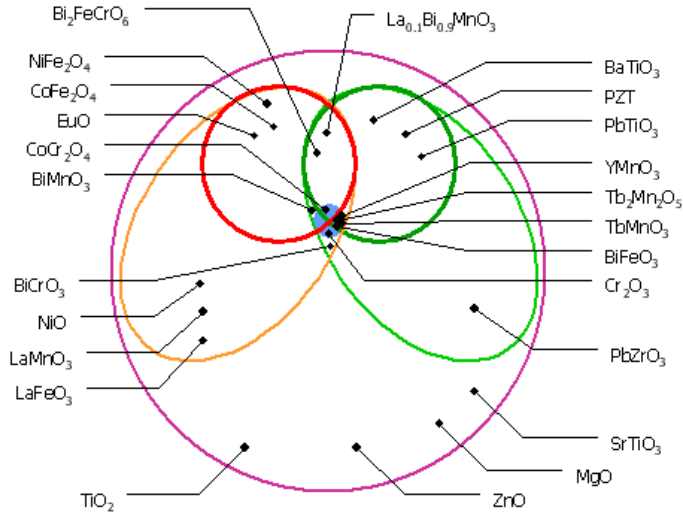


Figure 1.2: Arrangement of oxides: The biggest circle denotes different types of oxides, some of which represent electrically (green ellipse) and others illustrate magnetically switchable materials (orange ellipse). The circle within each ellipse illustrates materials which shows ferroelectricity, ferro and ferri-magnetism. The intersection among the ellipses represents multiferroics materials. The smallest circle in the middle represents multiferroics with magnetoelectric coupling ability.

implementation of smart devices, such as multi-state memory elements, electric field controlled ferromagnetic resonance devices and transducers with magnetically modulated piezoelectricity[5], [6]. The interactions between magnetic and electrical orders in these ME multiferroics provides a feasibility to control electric polarization by applying a magnetic field and vice versa. These paves the way for the implementation of new classes of storage devices, such as magneto-electric random access memory (MeRAM)[7], wherein data can be read magnetically and written electrically. The use of an electric field

in the writing procedure of magneto electric random access memories (MeRAMs) gives an appealing opportunity to combine the best qualities of ferroelectric random access memories (FeRAMs) and magnetic random access memory (MRAMs) including fast low-power electrical write operation, non-destructive magnetic read operation, significantly less energy waste in the form of heat and miniaturization of memory devices. It is worthy to mention here that multiferroics having ME coupling effect at room temperature are exceptionally rare and nearly all of them are antiferromagnets or weak ferromagnets[8]. Moreover, the ME coefficient is typically small because single phase multiferroics usually demonstrate weak magnetization and/or ferroelectricity. However, the magnetoelectric coupling may also arise indirectly into a multiferroic hetero-structure through mechanical strain within two separate phases, namely ferroelectric and ferro/ferrimagnetic. This method permits one to select ferroelectric and magnetic materials with necessary parameters individually and to design and fabricate multiferroic hetero-structure with ME coupling effect several orders of magnitude greater than that observed for single-phase multiferroic materials. These thin film hetero-structures shows multiferroicity which have extensive possibility for applications in multifunctional devices, such as sensors, actuators, magneto-electric transducers and heterogeneous read/write devices[9].

A serious concern in the advancement of commercial devices based on multifunctional oxides is the integration of high quality single crystalline epitaxial oxide thin films with semiconductors. Monolithic integration of oxide with semiconductors will facilitate both the sensing and logic functionalities to be incorporated on a single chip. However, semiconductors promptly form an amorphous oxide layer at the surface if exposed to oxygen ambient and this is considered to be one of the major challenges behind

the integration of oxides with semiconductors. The formation of an amorphous oxide layer impedes epitaxial growth of oxides on commonly used semiconductor substrates. Therefore, the oxide films deposited directly on semiconductors exhibit poor crystallinity and are not suitable for device applications. To overcome this challenge, the direct epitaxial growth of single crystal perovskite SrTiO₃ (STO) on Si (001) using ½ monolayer (ML) of Sr deposited on a clean Si (001) surface as a template provides the necessary breakthrough for single crystal oxide growth[10], [11]. Moreover, aggressive scaling of Si devices to comply with Moore's law has reached a bottleneck. The subsequent STO deposition on semiconductors has unlocked a new avenue for complementary metal oxide semiconductor (CMOS) technology for materials other than Si, e.g. Ge and GaAs because the feasibility of fabricating functional oxide hetero-structures utilizing ferroelectricity, superconductivity, and magnetism in a reasonably wide range of temperatures and oxygen partial pressures[12]. Researchers are exploring novel devices structures, technologies and materials to suffice scaling following Moore's law for sub 10 nm technology nodes. As a result, multifunctional oxides monolithically integrated onto III-V compound semiconductors such as GaAs, GaN are becoming progressively important because it offers a prospect for devices development that addresses the Si “end of roadmap” concerns by adding functionalities to CMOS devices[12].

1.1 Literature Review

1.1.1 Multiferroic Property

Materials that simultaneously demonstrate several primary ferroic order parameter in a single phase is defined as multiferroics[1], [2]. Ferroelectricity, ferromagnetism and ferroelasticity are commonly known as the basic primary ferroic order parameters whereas

anti-ferromagnetism and ferrimagnetism are known as the non-primary ferroic order parameters which can also be included into the definition of multiferroics[13]. Ferroelectricity can be defined as a spontaneous electric polarization of a material which can be switched by external electric field[14]. The term ferroelectricity is analogous to ferromagnetism which is described from a simple method by which certain materials form permanent magnets and/or show strong interactions with other magnets[15]. Ferroelastic material shows a spontaneous strain when an external stress is applied which is also known as a mechanical correspondence of ferroelectricity and ferromagnetism[16]. Usually ferroelastic materials changes from one phase to an equally stable different phase e.g. tetragonal to rhombohedral. Even though researchers have put together the theoretical prediction and experimental observations for the coexistence of several ferroic order parameters in a single phase material, multiferroics as a term was used first by H. Schmid in 1994[2], and has been extended to materials that have long range magnetic ordering, a spontaneous electric polarization and/or ferroelasticity. Furthermore, few scientists claim that the multiferroics term can only be used if there coupling between the ferroic order parameters. The overlap of these properties in ferroic materials is illustrated in Figure 1.1 and 1.2.

1.1.2 Magnetoelectric Effect

The generation of electrical polarization in a material by an external magnetic field or vice-versa is known as the magneto-electric effect. The ME coupling in composites is related to the mechanical interaction within the magnetostrictive and piezoelectric phases. In single phase multiferroic materials the ME effect is described using the Landau theory by simplifying the free energy expansion F of a system in terms of an external magnetic

field H whose i^{th} component is denoted H_i , and an external electric field E whose i^{th} component is E_i could be expressed in S.I. units as[4], [17]:

$$F(E, H) = F_0 - P_i^s E_i - \mu_0 M_i^s H_i - \frac{1}{2} \epsilon_0 \epsilon_{ij} E_i E_j - \frac{1}{2} \mu_0 \mu_{ij} H_i H_j - \alpha_{ij} E_i H_j - \frac{1}{2} \beta_{ijk} E_i H_j H_k - \frac{1}{2} \gamma_{ijk} H_i E_j E_k \dots \dots \dots 1.1$$

where F_0 , P_i^s and M_i^s represents the field independent energy, spontaneous polarization and magnetization respectively. The second ranked permeability and permittivity tensors are represented by μ_{ij} and ϵ_{ij} respectively. Another second ranked tensor α_{ij} denotes linear magneto-electric coupling and the third ranked tensors β_{ijk} and γ_{ijk} denotes the higher-order magneto-electric effects. The system polarization and magnetization may then be calculated by simply differentiating equation 1.1 with respect to E_i and H_i , respectively as:

$$P_i(E, H) = - \left. \frac{\partial F(E, H)}{\partial E_i} \right|_{E_i=0} = P_i^s + \alpha_{ij} H_j + \frac{1}{2} \beta_{ijk} H_j H_k + \dots \dots \dots 1.2$$

$$\mu_0 M_i(E, H) = - \left. \frac{\partial F(E, H)}{\partial H_i} \right|_{H_i=0} = \mu_0 M_i^s + \alpha_{ij} E_j + \frac{1}{2} \gamma_{ijk} E_j E_k + \dots \dots \dots 1.3$$

The magneto-electric effect can be shown to be limited only to the geometric mean of diagonalized permittivity and permeability tensors[18], by neglecting the higher order terms in equation 1 as:

$$\alpha_{ij}^2 \leq \mu_0 \epsilon_0 \mu_{ij} \epsilon_{ij} \dots \dots \dots 1.4$$

After the theoretical prediction of the ME effect by P. Curie in 1894[19], the first practical evidence of the ME effect was demonstrated by the Russian scientist Astrov in the anti-ferromagnetic Cr_2O_3 in 1960's[20]. The single-phase magneto-electric materials are rare in nature and their ME coupling response is usually weak. However, moderately

strong ME coupling effect could be accomplished artificially in a composite consisting of piezoelectric and magnetostrictive phases in which the electric polarization results from mechanical deformation. ME coupling coefficient of 130 mV/cmOe were first observed in bulk composites synthesized using a solid-state reaction technique between cobalt or nickel ferrites with BaTiO₃ in 1970's by Van den Boomgaard[21].

1.1.3 Single Phase Multiferroic Materials

It should be noted that the field of multiferroics initially came from the study of ME based systems. Single phase multiferroics exhibiting both ferromagnetic and ferroelectric simultaneously are very rare because spontaneous ordering is difficult to be achieved at the same time for the two-dipole species to exhibit ME coupling. In fact, single phase multiferroics mostly fit to the group of transition metal oxides with perovskite structure including ferrites and rare-earth manganites such as LuFe₂O₄, TbMnO₃ and HoMn₂O₅. Other types of multiferroics are also possible such as the bismuth alloys BiMnO₃ and BiFeO₃. Moreover, some materials from outside of the oxide family are also show multiferroic property such as BaNiF₄ and spinel chalcogenides, e.g. ZnCr₂Se₄. Even though ME multiferroics was discovered in 1960's, the advancement of research for multiferroic materials remained unchanged until 2000 shown in figure 1.3 which illustrates the explosion of publications since the discovery of strong magneto-electric coupling effect in orthorhombic TbMnO₃[22] and TbMn₂O₅[23].

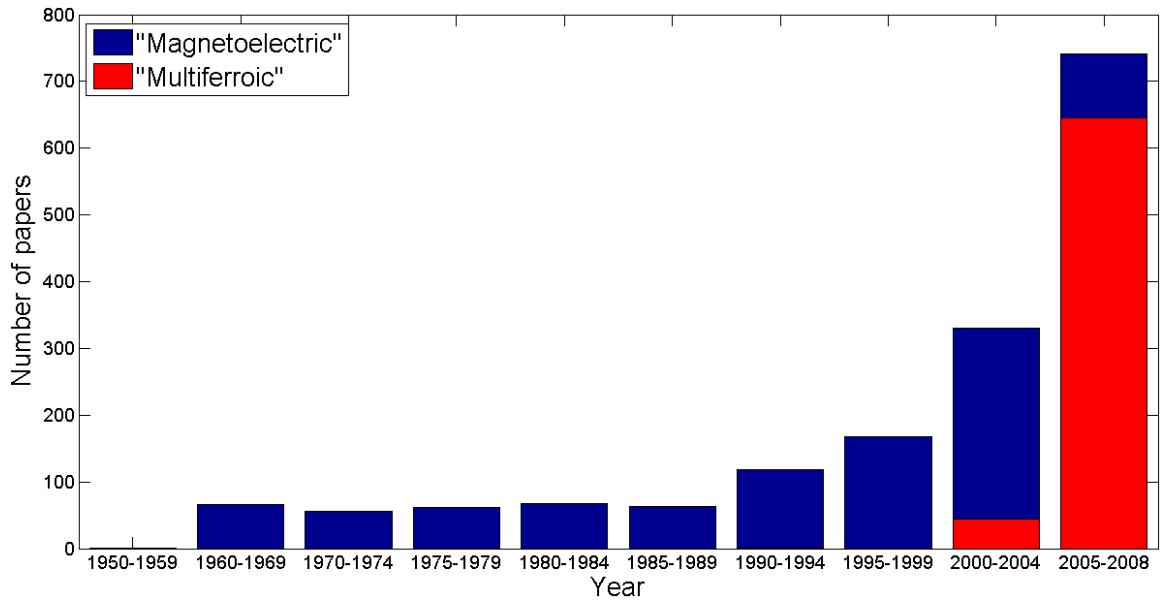


Figure 1.3: Number of papers from 1950-2008 using magnetoelectrics or multiferroics as keywords[24].

A study of MnWO_4 showed that, below ~ 13 K the magnetically ordered phase and the spontaneous electric polarization reveals this material to be a novel multiferroic material[25]. In single crystal multiferroic hexagonal manganites such as YMnO_3 a giant magneto-elastic coupling has been observed[26] representing an almost two orders of magnitude higher coupling than any other magnetic materials exhibiting multiferroic behavior. Giant magneto-electric response at room-temperature in LuFe_2O_4 upon application of a magnetic field revealed another ME coupling phenomenon with possible applications in designing magnetic storage devices[27]. Ramesh's group successfully deposited epitaxial thin films of one of the most investigated and promising, multiferroic, BiFeO_3 in 2003. Even though in BiFeO_3 , multiferroic properties are fairly weak in its bulk form it is effectively enhanced in thin-films[28]. Most importantly, the discovery of large ferroelectric polarization [28] and the realization of electric-field-controlled magnetic state[29] in epitaxial thin films of the ferroelectric-antiferromagnetic (FE-AFM) BFO

creates a new degree of freedom to manipulate the ME coupling in nano-scale and opens the possibility for using multiferroic ME materials for on-chip integration in new electronic devices. Currently as the most promising multiferroic materials, BFO has already shown its potential application in spintronics [30] and FeRAMs[31]. In fact, the theoretical calculation and experimental investigation on BFO started in 1960's[32], but its realization for practical applications remained static until the demonstration of large room-temperature ferroelectric polarization in combination with the fascinating magnetic properties of epitaxially strained BFO films. Among the few reported room temperature single-phase FE-AFM[33], BFO thin film shows the highest ferroelectric polarization of $90 \mu\text{C}/\text{cm}^2$ (figure 1.4 (b)) along its ferroelectric-preferred pseudocubic $\langle 111 \rangle$ direction and $70 \text{ pm}/\text{V}$ of out-of-plane converse piezoelectric coefficient[34].

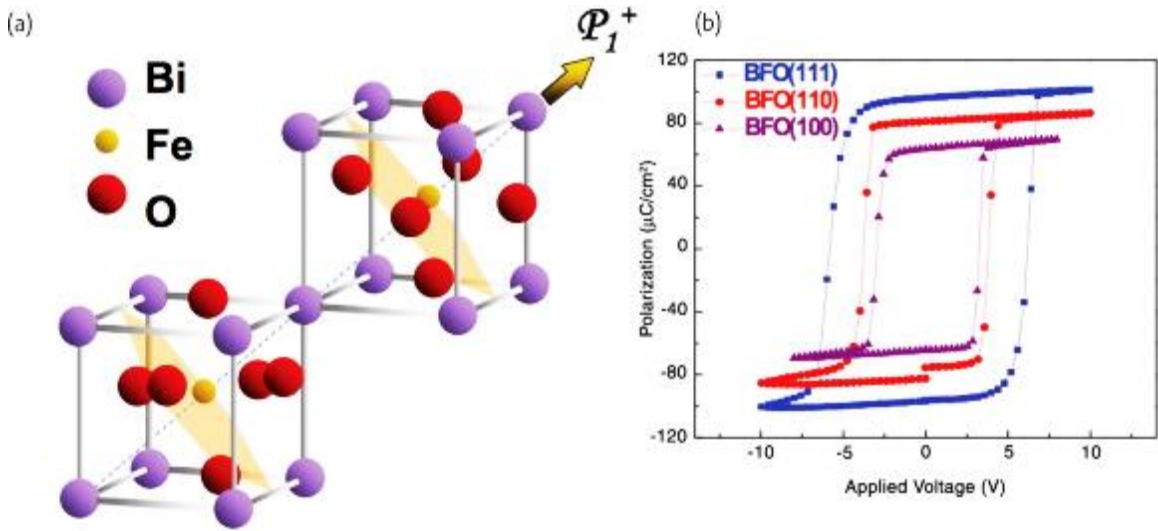


Figure 1.4: (a) Schematics of BFO crystal orientation. The antiferromagnetic plane and ferroelectric polarization are represented by shaded planes and arrow respectively. (b) Polarization hysteresis loops measured on epitaxial BFO films with different crystallographic planes[35].

Unlike other FE-AFMs, BFO possesses a very high ferroelectric Curie temperature (T_C) of $\sim 1100 \text{ K}$ and a high antiferromagnetic Néel temperature (T_N) of $\sim 640 \text{ K}$. The

structure of BFO is illustrated in figure 1.4 and consists of tilted perovskite unit cells which is connected diagonally in the pseudocubic $\langle 111 \rangle$ direction to form a rhombohedral unit cell. The ferroelectric switching is achieved by a large dislocation of Bi ions with respect to the FeO_6 octahedra. This fascinating physical structure governs the properties in two aspects: first, four structural variants along the pseudocubic $\langle 111 \rangle$ direction helps the formation of eight possible polarization variants accordingly; second, the existence of G-type antiferromagnetic ordering due to Fe magnetic moments are aligned ferromagnetically within (111) plane and antiferromagnetically between adjacent (111) planes, shown in figure 1.5. Therefore, the AFM and FE orders can be coupled together. Specifically, the switching of FE dipoles connected with the switching of AFM plane, makes this material suitable for the spintronic and multiferroic tunneling devices.

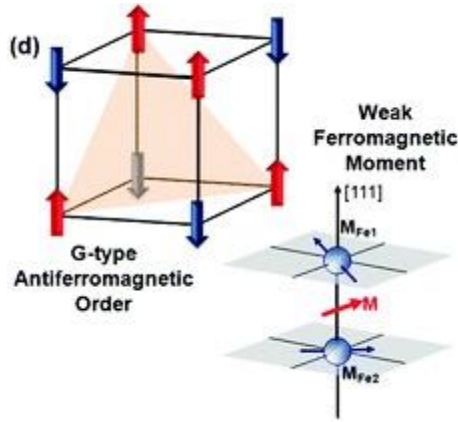


Figure 1.5: Schematic representation of ferroelectric polarization [111] direction perpendicularly to the G-type antiferromagnetic plane of BFO.

Epitaxial growth of single crystalline BFO thin films is difficult because several stable Fe oxides can form during growth and Bi is also very volatile. Béa, et al conducted a detailed investigation of the influence of growth conditions on the properties of BFO films[36]. The phase diagram of BFO films for the optimum pressure and temperature

grown by pulsed laser deposition is shown in figure 1.6 where, we can conclude that single phase BFO can only be formed in a very narrow pressure-temperature window. BFO thin films are usually ferroelectric, antiferromagnetic and insulating. The center image on the right side of figure 1.6 denotes a neutron diffraction $(1/2, 1/2, 1/2)$ peak indicating G-type antiferromagnetic order for a 70 nm BFO film grown on STO (001).

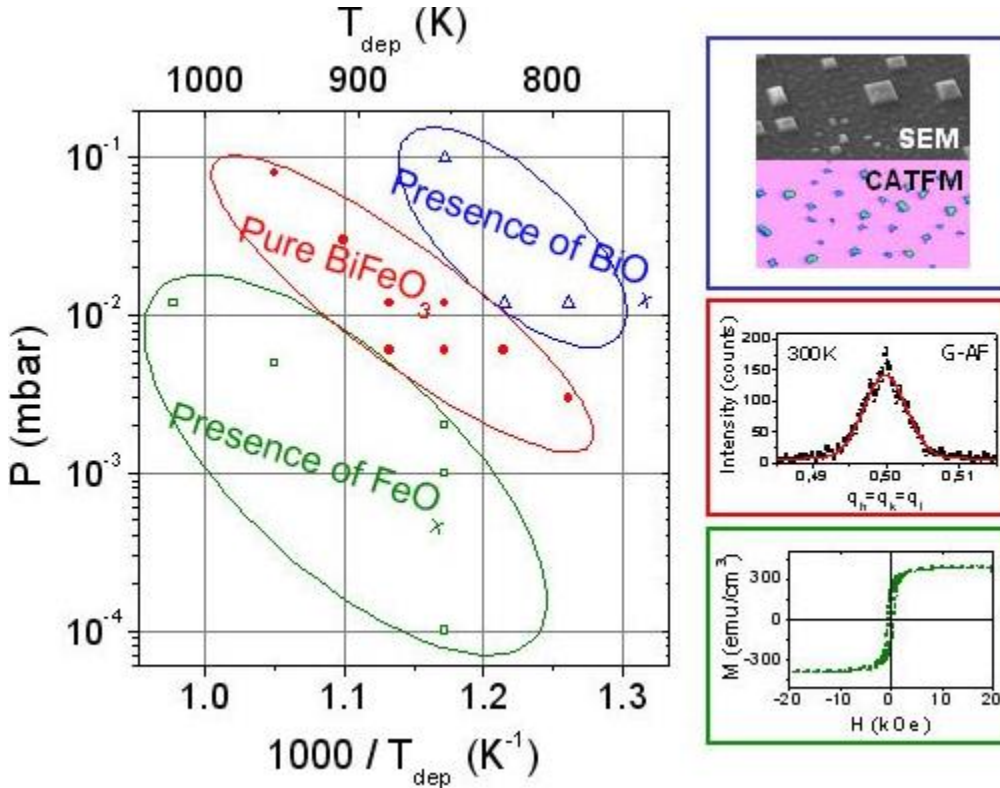


Figure 1.6: Effects of parasitic or secondary phases on BiFeO₃ epitaxial thin films properties[36].

Outside of this temperature-pressure window, Bi- or Fe-rich parasitic or secondary phases form. The top image on the right side of figure 1.6 displays scanning electron microscopy (SEM) and conductive-tip AFM images of a BFO film showing square and conductive Bi₂O₃ impurities. The magnetic hysteresis curve of a BFO film with ferrimagnetic gamma-Fe₂O₃ impurities shown in the bottom right inset of figure 1.6.

1.1.4 Exchange Bias

In a coupled antiferromagnetic-ferromagnetic system exchange bias or exchange anisotropy usually occurs; here a unidirectional shift in the ferromagnetic hysteresis curve towards the applied field axis develops due to interfacial spin effects within the AFM and FM materials. Hypothetically, adding an AFM and a FM layer together does not cause this shift in hysteresis curve instantaneously but an obvious increase in coercive field is present. However, when an exchange bias system is field cooled through the Néel temperature of the AFM layer a shift in the hysteresis loop originates in the opposite direction of the magnetic field during cooling cycle[37]. These effects are illustrated in figure 1.7. Exchange bias (H_{EB}) was first explored by General Electric (Meiklejohn and Bean) in 1956[38], and due to its effectiveness in magnetic device applications such as magnetic stabilizers used in hard disk read-write heads has received a lot of attention. However, its efficacy in magneto-electric devices has been utilized very recently[39], [40].

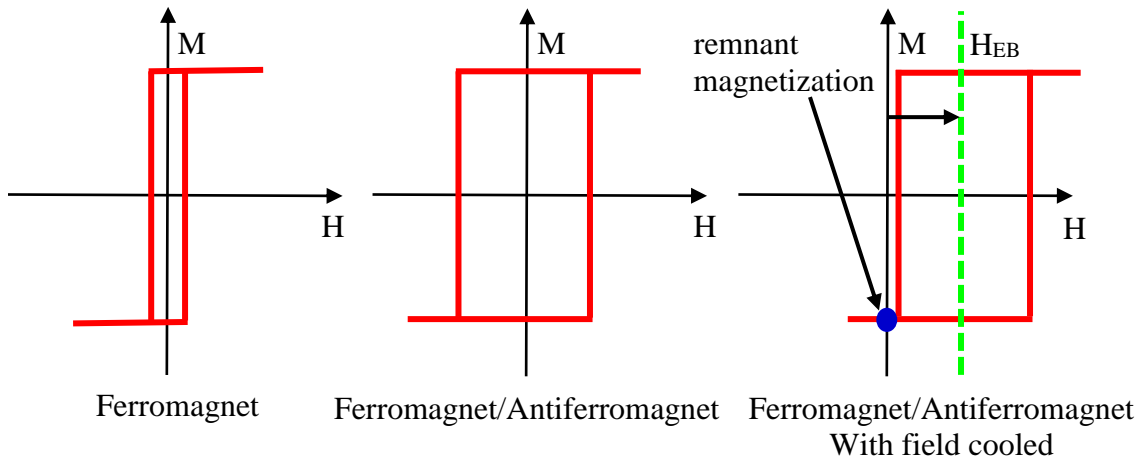


Figure 1.7: The interfacial effects due to coupling between AFM-FM systems are depicted in which the hysteresis loop undergoes a shift when field cooled. Usually FM material has a small coercivity and is symmetric with the external magnetic field axis. After adding an AFM to the FM layer, enhancement in coercive field due to a spin-drag effect is observed but the hysteresis curve remains symmetric. Field-cooling when applied to an AFM-FM system through the Néel temperature of the AFM material provides coercive field enhancement with an exchange bias and the hysteresis curve is no longer symmetric.

Despite being developed more than 50 years ago, a comprehensive understanding of exchange bias has not yet been achieved. Recent empirical and theoretical work has found many features of exchange bias that beyond the capability of simple mathematical models developed right after its discovery. In order to understand exchange bias systems from the basics we will start with the simplest early model. With an ideal interface among AFM and FM, the exchange bias can usually be explained by a simple co-linear spin system as illustrated in figure 1.8[37], [41]. First, the cooling cycle start from above the Néel temperature of the AFM to align the FM spins by an external magnetic field, where the AFM spins remained randomized (Figure 1.8a). In the next step, the temperature is decreased below the AFM Néel temperature so that AFM order starts to reposition themselves and all the AFM spins at the interface will be aligned with the FM order due to interfacial magnetic interactions (Figure 1.8b). Here, AFM spins align ferromagnetically at the interface, and depending on the type of interface interactions antiferromagnetic alignment could also be possible. At this point all the AFM spins could be frozen-in due to AFM anisotropy, so if we sweep magnetic field in the reverse direction an increase in the magnetic field will be required to switch the magnetization of FM layer because of a force that arises among AFM and FM due to interfacial interactions (Figure 1.8c). If the magnetic field is reversed then the additional force due to the AFM interfacial alignment now helps the initial spin direction so that a reduced magnetic field is necessary to switch the spins back (Figure 1.8d).

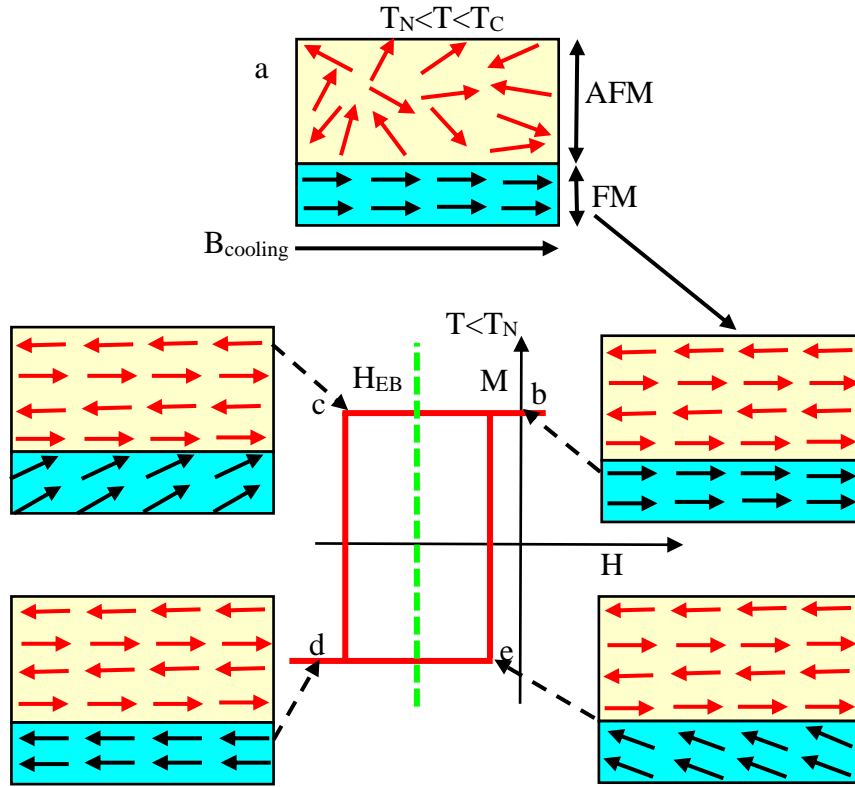


Figure 1.8: Schematic of a simple model to describe exchange bias along with interface spin structure and the effect on the magnetic hysteresis curve is presented. At first the AFM-FM system is above the Néel temperature of the AFM (a), and is field cooled to a starting state (b). Changing external magnetic field is in the reverse direction and back depicted in (c), (d), and (e).

The final outcome is a shifted hysteresis curve in the reverse direction to the original magnetic cooling field. This simple model can be explained as an effort to quantify the exchange bias field. The energy per unit area for an exchange bias system is described as:

$$E = -HM_{FM}t_{FM} \cos(\theta - \beta) + K_{FM}t_{FM}\sin^2(\beta) + K_{AFM}t_{AFM}\sin^2(\alpha) - J_{INT}\cos(\beta - \alpha) \dots \dots \dots 1.5$$

where H is the external magnetic field, M_{FM} , K_{FM} and t_{FM} is the saturation magnetization, anisotropy energy and thickness of the FM respectively, K_{AFM} and t_{AFM} is the anisotropy

energy and thickness of the AFM respectively and J_{INT} is the interfacial coupling constant. For both the FM and AFM material the anisotropy axis is assumed to be the same, and θ , β and α are the angles between H , M_{FM} , and M_{AFM} with anisotropy axis, respectively.

Now the above equation 1.5 can be simplify by assuming that K_{FM} is much smaller than K_{AFM} , which has been demonstrated experimentally.

$$E = -HM_{FM}t_{FM} \cos(\theta - \beta) + K_{FM}t_{FM} \sin^2(\beta) - J_{INT} \cos(\beta - \alpha) \dots \dots \dots 1.6$$

Equation 1.6 can be further minimized by considering the energy with respect to α and β , because these are two separate limiting cases which results in different spin behavior. Now assuming $K_{AFM} t_{AFM} \gg J_{INT}$, the energy will be minimized by keeping α small, leading to the AFM spins being pinned, and resulting in an exchange bias of:

$$H_{EB} = \frac{J_{INT}}{M_{FM}t_{FM}} \dots \dots \dots 1.7$$

In the second step, when $K_{AFM} t_{AFM} \ll J_{INT}$, the energy will be minimized by keeping ($\beta - \alpha$) small, and the AFM spins will rotate with the FM spins without developing any exchange bias. In this scenario coercivity is enhanced because the force from the interface still dragging the spins and triggering them not to switch easily. This unevenly contributing AFM spins could explain some of the interesting features of exchange bias systems such as, the low number of spins that are pinned and without enhancing the coercivity they can significantly contribute to exchange bias, while some other spins could rotate with enhanced coercivity and less contribution to exchange bias[42]. Despite the huge successes of this basic model, there are still certain inconsistencies between theory and reality.

For instance, the estimated value of exchange bias from theoretical calculations is several orders of magnitude larger than experimentally measured values. In order to explain

this obvious disparity, numerous models have since been considered that include AF domain walls forming at the interface[43], or having rough interfaces[44]. All of these models usually consider an ideal interface structure where only a small fraction of the spins in the AFM are directly contributing to exchange bias. However, recent experiments using the x-ray spectroscopy in some AFM-FM systems shows that only ~ 4 percent of interface spins are actually pinned[45]. For the simplified models the dependence on systems with uncompensated interfaces are considered as one of the failure point because they are based on the assumption that all the AFM spins at the interface lie in the same direction. It has been shown, in many exchange bias systems, that different type of antiferromagnetism could allow the interface to be magnetically compensated such that there is no net magnetization at the interface in the AFM layer. A few models have been developed trying to explain all the unknown features of exchange bias system but a full understanding has not yet occurred due to the difficulty of observing the spin structure of an atomically thin interface layer[41]–[45].

II. CRYSTALLINE FUNCTIONAL OXIDE GROWTH AND CHARACTERIZATION TECHNIQUES

2.1 Introduction

Satisfactory control of thickness, stoichiometry and oxidation conditions are the primary requirements for the growth of single crystalline complex oxide layers on semiconductors. There are few techniques at present that have been shown to be capable of providing such precise control. A brief description of these thin film deposition techniques with emphasize on the growth and characterization of multi-component oxide materials will be provided in this chapter. Multi-component complex oxides are difficult to deposit because these are composed of three or more elements. In order to grow highly crystalline device quality oxide thin films: (a) the complex composition of the compound source must be stoichiometrically transferred to the substrate when using a compound source target as in pulsed laser deposition technique or (b) precise control with monolayer or better degree of precision of the fluxes of all the elements involved due to the multi-component nature of a typical complex oxide must be achieved[46]–[50]. During the growth of complex oxides on semiconductors, except for oxygen, one cannot have an excess flux or overpressure of one element over another without also resulting in an excess formation of that element in the film, especially when the sticking coefficient is unity. Additionally, oxygen flux or pressure must be controlled precisely since excess oxygen could result in the oxidation of the underlying semiconductor substrate.

The epitaxial growth of complex oxides and its integration onto semiconductors has been developed only in the last 20 years. Shortly after high- T_C superconductors discovery, enormous development in the thin film growth of multi-component oxides was

undertaken for example, the development of the pulsed laser deposition technique[51] and the use of activated oxygen sources in molecular beam epitaxy[52]. By adapting these concepts, it is possible to deposit high quality oxide materials and investigate novel experimental pathways for integrating these oxides and semiconductor materials into a single structure with multi-functionality. Due to the multi-functional nature of complex oxides, system on chip or integrated sensor/transistor systems are now possible to develop where the transistor function could be directly coupled to environmental stimulus, such as temperature, pressure, and electromagnetic fields.

In this chapter, a brief outline of two different thin film deposition techniques which have been utilized most for this work; molecular beam epitaxy and pulsed laser deposition and have demonstrated their capability of growing oxide thin films epitaxially on semiconductor substrates will be explained. This chapter also describes the characterization techniques and measurement setups used in this work.

2.2 Molecular Beam Epitaxy

Molecular beam epitaxy (MBE) is based on the thermal evaporation of elemental sources under ultrahigh vacuum conditions and are type of physical vapor deposition process[53], [54]. Ultrahigh vacuum chamber with a base pressure around 10^{-10} Torr to reduce the unwanted impurity/defects, effusion cells that enable the highly directional flow of evaporated source materials, oxygen gas or plasma source, substrate manipulator and heater, and in situ characterization tools for continuous growth monitoring are the main components of a typical oxide MBE system. The combination of effusion cells as evaporation sources and ultralow base pressures of MBE systems ensures that the evaporated materials are in the form of atomic or molecular beams that are directed towards

the substrate. These atomic or molecular flux or beams can be rapidly turned on and off by a fast-mechanical shutter which is pneumatically actuated, allowing for the growth of complex multilayer heterostructures which can have different compositions for different layers. The flux of the atomic beam of the element to be evaporated is precisely controlled by the temperature of the crucible in the effusion cell and is also related to the vapor pressure of that material itself. Oxide growth cannot occur without additional source of oxygen and most of the cases this is either supplied as molecular oxygen, or with more reactive oxygen species such as ozone or atomic oxygen from a plasma source. The type of oxygen sources can also limit the types of oxides can be grow, for example, if only molecular oxygen used, then it will be limited only to those oxides that have metals that can readily oxidize while other oxides such as LaCoO_3 and LaNiO_3 require a reactive oxygen source for growth[49]. However, the requirement of reactive oxygen in the form of ozone or atomic oxygen demands the use of additional equipment. For simple mono-oxides, the growth is quite straightforward because a single metal flux can be used in the presence of an excess oxygen ambient. Complex oxides with multi-cation/anion sites such as the perovskite oxides, requires an additional requirements of calibrating and controlling the two metal fluxes to maintain the correct phase and stoichiometry when using co-deposition. Unlike compound semiconductors, complex oxides do not have very well-studied line compounds[48], so time consuming molecular flux calibration is a critical concern in MBE growth because a poorly calibrated metal flux often results in the formation of secondary phases or non-stoichiometry.

Flux calibration during MBE deposition is generally carried out by one of several techniques by using a: (1) quartz crystal microbalance; (2) nude ion gauge to measure

beam-equivalent pressure; or (3) atomic absorption spectroscopy. The technique of using an ion gauge or quartz crystal to monitor evaporation source fluxes requires installing the ion gauge or crystal on a retractable arm to move it to the substrate position during measurement and remove it before the growth starts. Ion gauge measures the pressure difference during opening and closing the source shutter and this pressure reading can be converted to molecular flux through a simple equation[55]. Quartz crystal microbalance measures flux by monitoring the change in frequency of a quartz crystal resonator due to a mass variation per unit area when deposition starts by the evaporated source materials[56]. The crystal's mass will increase by the material being deposited which will shift the oscillation frequency that is continuously read by an electronic instrument and performs appropriate mathematical functions to convert that frequency shift to cumulative thickness and rate simultaneously. Mostly, quartz crystal microbalance systems are water cooled because crystal's performance is highly influenced by the temperature as well as it can take more than 30 min for the crystal to stabilize. As a result, both the flux measurement by an ion gauge or quartz crystal microbalance are usually $\sim 5\%$ accurate and not enough to provide sufficient control for certain applications. Atomic absorption spectroscopy is a well-known method of measuring flux more accurately since it uses a focused light towards the beam path of the evaporating material and uses a detector to sense the amount of light has been absorbed[57]. The absorption specific to a wavelength for individual atoms allows precise measurement for different element of the cells. This provides accurate molecular fluxes with a discrepancy below 1 %. However, the key downside is the requirement of more expensive instrumentation for an atomic absorption flux monitor system and coating of windows or view ports.

Another aspect of MBE which makes it superior over other thin film deposition techniques is its ability to simultaneously change the stoichiometric ratio of alloys within the same growth run. For instance, a graded $\text{Ba}_{1-x}\text{Sr}_x\text{TiO}_3$ can be grown with MBE in a single growth while this would require a very complex growth involves multiple target changes and multiple runs with several steps using pulsed laser deposition or sputtering. Moreover, unlike the unit cell block growth mode of pulsed laser deposition or sputtering, MBE allows full control of the thin film's surface termination due to its true atomic layer-by-layer capability. The low background pressure during MBE growth even with the controlled oxygen environment provides the flexibility to continuously monitor the growth process in real time by providing information of the crystalline structure, lattice spacing, film thickness, surface roughness, and surface composition by various in situ real-time characterization techniques e.g., Reflection High Energy Electron Diffraction (RHEED), X-ray fluorescence, Auger spectroscopy, Electron Energy Loss Spectroscopy, and Cathodoluminescence[11], [58]–[61]. Additional in situ characterization methods are also commonly used in MBE systems include ellipsometry[62] and reflectance anisotropy spectroscopy[63].

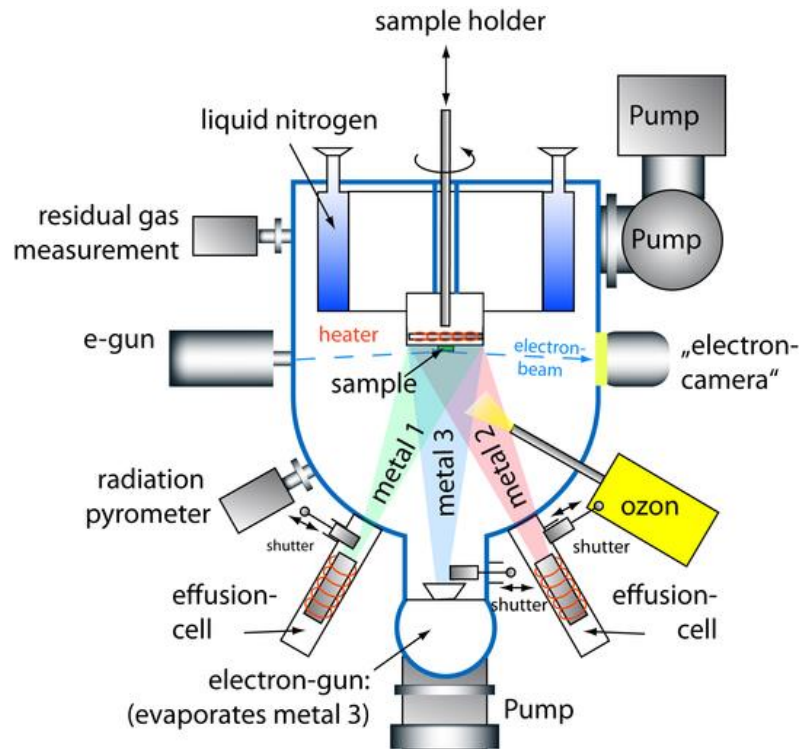


Figure 2.1: (a) Schematic of an oxide molecular beam epitaxy system[64].

A schematic and the real image of a typical oxide MBE system is shown in figure 2.1 (a) and (b). For complex oxide, transition metals are a common element and it is difficult to evaporate some of these transition metals with sufficient stable flux due to their low vapor pressure. Available high temperature effusion cells can be operated at temperatures close to 2,000 °C and can provide stable but low flux rates for some of the common transition metals such as titanium and vanadium. However, there are still a good number of transition metals whose vapor pressure is still not sufficiently high at 2,000 °C

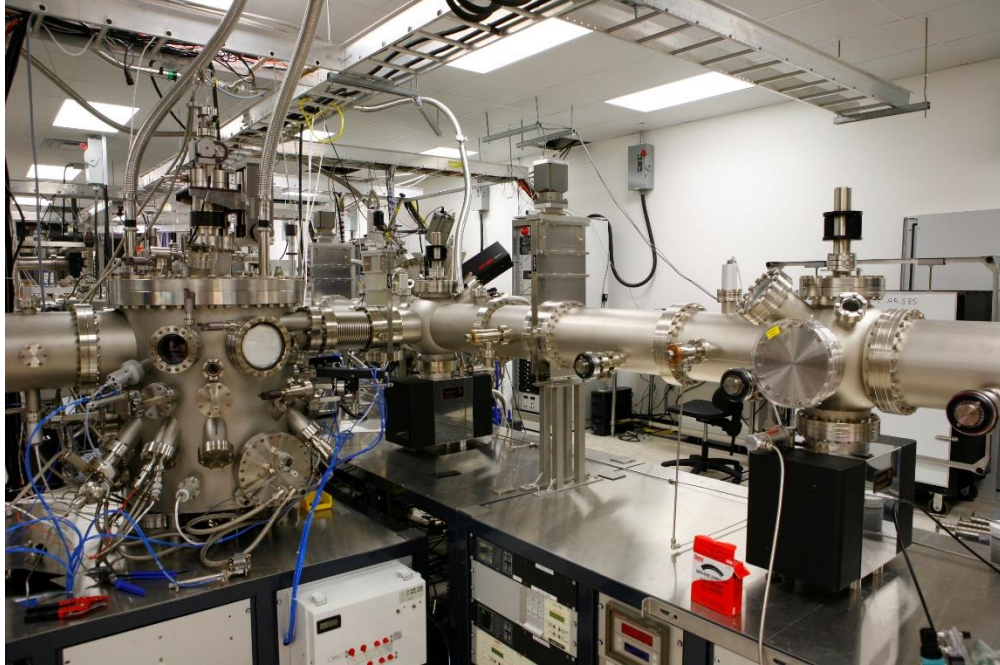


Figure 2.1: (b) Oxide molecular beam epitaxy system connected to the clyster system through buffer line at advanced functional materials laboratory of Texas State University.

such as, niobium and ruthenium. For such transition metals an electron beam evaporator is usually used other than the effusion cells[65]. However, an electron beam evaporator provides poor flux stability and run to run reproducibility. For oxide MBE growth, stable fluxes can be achieved if the vapor pressure of the material exceeds 10^{-3} to 10^{-2} Torr. Required temperature for an effusion cell to achieve necessary vapor pressure can be found from vapor pressure vs. temperature tables and charts[65], [66]. The compatibility factor between the material to be evaporated and crucible material is another concern when using effusion cells. Ideally, at high temperature, the evaporated materials should not wet the crucible and must not react with each other. Several well defined tables of evaporation compatibility that are essential to MBE users are available online[49].

2.3 Pulsed Laser Deposition

In pulsed laser deposition (PLD) thin films are deposited by a series of high energy laser pulses which rapidly evaporate the source material in the gaseous phase with subsequent transferred to the substrate. This is also known as laser ablation or laser MBE and no other deposition techniques has had as big impact as laser-ablation growth techniques in the creation of oxide materials[67], [68]. Under optimized condition it is possible to directly transfer stoichiometry of the target or source materials into the substrate as a grown film is the main advantage of PLD. This also solves the major limitation of MBE technique for not requiring the need for precise control of individual evaporation rates of different elements of a complex oxide material. A PLD system and its basic schematic is shown in figure 2.2 (a) and (b). Here a laser is used for rapidly heating the target or source materials locally and is usually installed outside the vacuum chamber and most often a high-power KrF excimer gas lasers serves as the laser source. The laser is usually focused onto the target through a combination of quartz lens of mirrors and allows the source materials to be evaporated hyper-thermally with kinetic energies ranging from 5 to 100 eV. These energetic evaporated materials once arrive at the substrate, still has sufficiently high enough energy for surface diffusion even at low substrate temperature or some cases results in re-sputtering of the substrate or the growing film in others. Unlike the drawbacks of oxide MBE, stoichiometric transfer of the source material to the substrate and the ability to use wide background O₂ pressure range from high vacuum ($\sim 10^{-7}$ Torr) to about 1 Torr are the

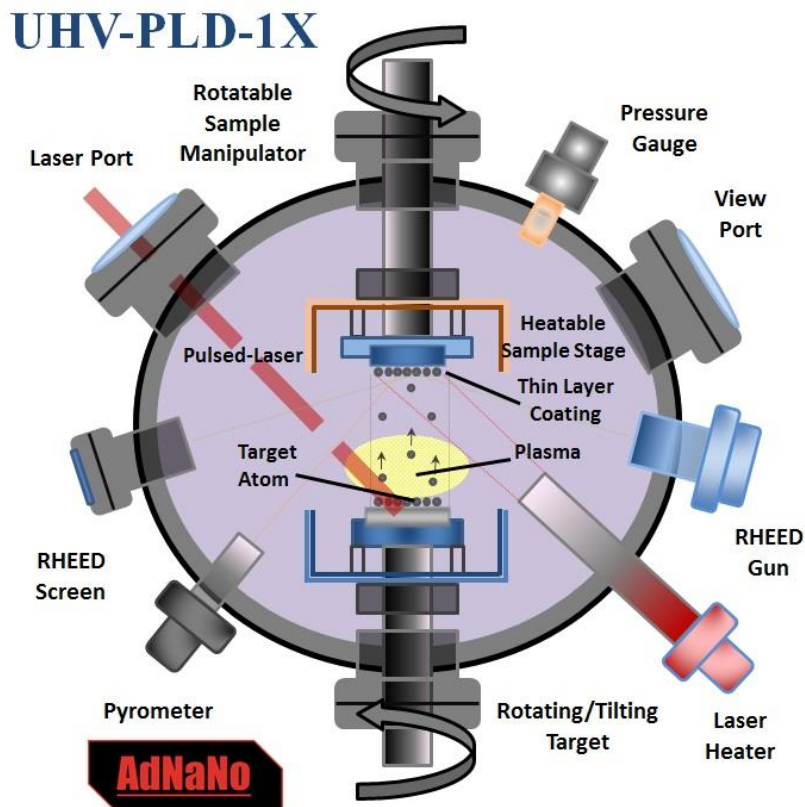


Figure 2.2: (a) Schematic of a basic pulsed laser deposition system[69].

main advantage of PLD technique[70]. For complex oxide materials, the ability to tune the oxygen partial pressure during growth over a wide range delivers more flexibility for achieving optimized growth condition to remove oxygen vacancy and maintaining complex stoichiometric ratio. However, PLD suffers from some major drawbacks and most significant is known as splashing which is the ejection of large microscopic particle from the source material. Moreover, due to the highly directional nature of plasma plume of source material, PLD techniques are unsuited for deposition on large area substrates and often suffer from composition and thickness uniformity issues. Even though most of the

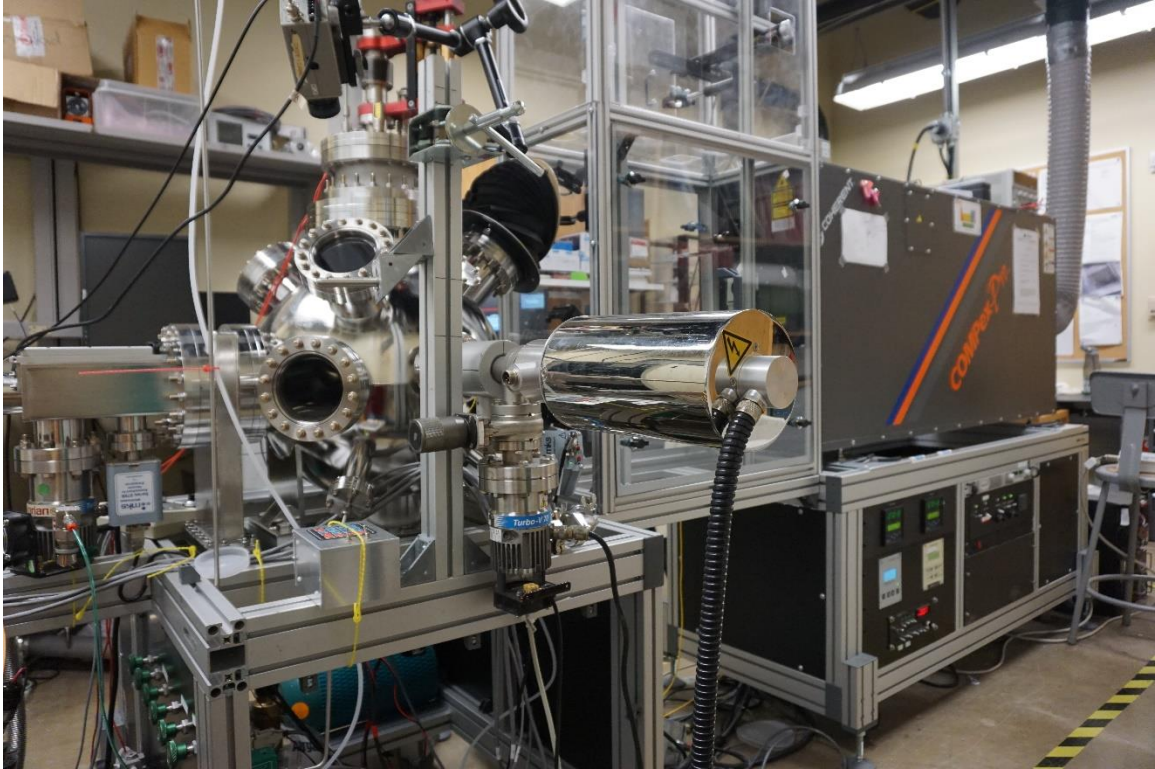


Figure 2.2: (b) Pulsed laser deposition system installed at Texas State University.

research level PLD systems are limited to 2 inch wafers, there are commercially available PLD systems that are already on the market which could easily provide 12 inch wafer deposition capability[70].

In a PLD system, the laser is the most expensive and critical piece of hardware whose, wavelength must be chosen in such a way that it will strongly be absorbed by the source material as well as being able to transfer satisfactorily high energy densities $\sim >1$ J/cm². Optimum wavelengths for PLD systems are in the range of 200–400 nm and it also possible to use standard optical elements for focusing and guiding the laser beam from outside to inside the chamber. For these reasons, PLD systems are mostly equipped with excimer lasers and are based on either KrF (248 nm) or XeCl (308 nm). For focusing and beam shaping, lenses that transmit UV light are needed to be placed between the laser and

the growth chamber. Lenses made of sapphire or UV-grade fused silica in combination with various apertures to minimize aberrations are used. Collimated and focused laser beam passes through the laser port and then enters the vacuum system of the growth chamber through a window which is optically flat and free of defects and usually made from the same material as the lenses to minimize losses due to reflections. For PLD growth, substrate temperature and growth pressure along with the geometry of vacuum chamber specifically the relative positions of the target and the beam focal point plays an important role. The laser port and the target are usually kept around 45° angle to achieve maximum beam focal point. The PLD process is also quite sensitive to the distance between substrate and target should be optimize for stoichiometric transfer during deposition.

To achieve uniform thickness, substrate stage is usually rotated during the deposition process. For single crystal epitaxial growth, the substrate needs to be heated at high temperatures so that substrate manipulator also serves as a heater. Manipulator or substrate heater must be oxygen-resistant at high temperature and yet still be capable of heating to at least 1000 °C. The final major component of a PLD system is the target holder. Most of the PLD systems utilizes a target rotation system or a laser scanning/rastering system that reduces the major part of the uneven target erosion. Due to this reason, targets are placed in such a way that are relatively easily accessible and easily mounted/dismounted. Since PLD targets are requires to be resurfaced or mechanically polished periodically to remove uneven target erosion and particulate buildup during growth. Source materials or targets usually available in disc form and are easily mounted onto the target holder by mechanical clamping, bonding, or magnets. Recent PLD systems contains the targets mounted in a multi-target carousel which allows several source

materials to be loaded at the same time. Multi-layer thin film heterostructures of complex oxides can then be easily grown by moving the carousel so that the laser hits the desired target.

Moreover, complex oxides thin film growth using PLD comprises the precise control of many processing parameters that can strongly affect the composition and microstructure such as the laser fluence and repetition rate[71]. For retaining the target stoichiometry in the film, laser fluence is a key parameter which controls the degree of ionization and the kinetic energy of the ejected particles of the target that ultimately affect the morphology of the film as a result of particulate formation[72].

2.4 Laser Materials Interactions

Laser ablation of materials is a complex process and depends on the laser parameters as well as the optical, topological, and thermodynamic properties of the source material which need to be evaporated. Electromagnetic energy of the laser first absorbed by the solid surface and then converted to a series of different energy such as electronic excitation, thermal, chemical, and even mechanical energy that finally creates evaporation, ablation, excitation, plasma formation, and exfoliation. The plasma plume usually contains a combination of energetic species including atoms, molecules, electrons, ions, clusters and even micron-sized solid particulates shown in figure 2.3. The resulting plume is highly directional and has a dense shape that quickly expands in the vacuum environment to create a jet propulsion of evaporated material directed at a normal of the target surface. For a fast deposition process with maintaining complex stoichiometry and congruent evaporation, PLD is the ideal candidate but the directed nature of the plume also limits PLD to a research level system that is difficult to scale-up to large wafers[71], [73].

Excimer lasers typically have a pulse duration of 10–30 ns and the laser ablation or the plume formation must take place within this time scale and can be described as a flash evaporation process. The plume formation can be divided into a series of events, the first of which is the photon absorption process. Absorption in any material can be defined as:

$$I = I_0 \exp(-\alpha x) \dots\dots\dots 2.1$$

where $1/\alpha$ is the absorption length and most of the time remains within ~ 100 nm for complex oxide materials. This absorption length also depends on the laser wavelengths commonly used in PLD (i.e., <400 nm). This step allows the electrons of source materials to be excited and thermalized within the picosecond time scale. The next process offers surface melting of the target by conducting heat into the bulk. Surface melting highly depends highly on thermal diffusion length and can be described as:

$$\lambda_{th} = 2(\alpha_{th} \Delta t)^{1/2} \dots\dots\dots 2.2$$

where α_{th} is the thermal diffusivity and Δt is the pulse duration. During this process, the temperature rises instantly within the top surface of the target and prepares for the evaporation.

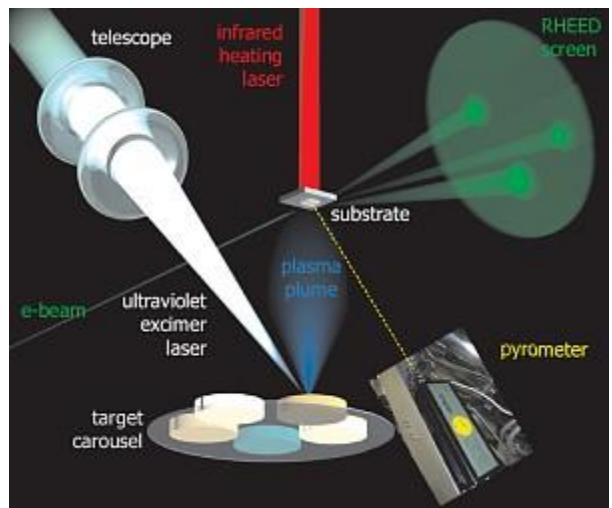


Figure 2.3: Schematic of the energetic plasma plume[74].

The actual evaporation of the target material is the next step where a multiphoton ionization of the gaseous phase creates the characteristic plasma. This process also allows the temperature of the target at the surface that well exceeds the boiling point. The final event of the process is the creation of plasma excitation during which further ionization occurs and free electrons are excited[46], [73].

The threshold of ablation, or the minimum energy density required in a material to create a plume can be considered further to take this analysis to the next level. To do that, let's start with the comparison of absorption length ($1/\alpha$) and thermal diffusion length (λ_{th}) where the thermal diffusion length is much longer than absorption length for UV lasers. Because complex oxide materials are mostly opaque and good thermal conductors. The effective volume for plume formation can be calculate which is related to the spot size times λ_{th} . If the volume of the affected material is known then a simple estimation can be used to calculate the minimum energy needed to raise this volume of material to its sublimation point as follows:

$$Q_{Heat} = C_S(T_{Melt} - T) + \Delta H_m + C_m(T_{Vap} - T_{Melt}) + \Delta H_{Vap} \dots \dots \dots 2.3$$

For equation 2.3 (moving left to right), required total heat energy is the summation of the energy needed to increase the target material temperature to the melting temperature plus the heat during its stay at the melting point and the energy required to increase the temperature of melted material to its vaporization point plus the heat of vaporization. Even though it seems like a huge amount of energy, lasers can provide more than enough energy to ablate nearly all materials because the typical power density of a single laser pulse with energy density of $\sim 2 \text{ J/cm}^2$ and 20 ns in length is nearly 10^8 W/cm^2 [46], [71], [73]. The distribution of evaporated elements or the plume's geometric shape can be explained with

two components. Of them one follows a simple $\cos\theta$ distribution and has considerable

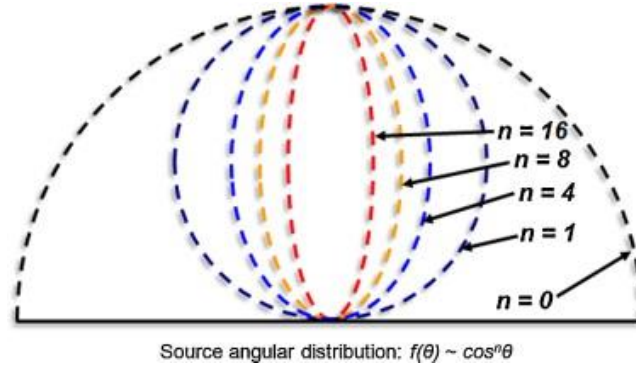


Figure 2.4: Schematic illustration of the shape of a plasma plume created by pulsed laser deposition. The angular distribution of the plume is dominated by a $\cos^n\theta$ function[73].

thermal energy but tends to be nonstoichiometric as in conventional thermal evaporation. A sharply lobed $\cos^n\theta$ distribution with n values in the range of 4–16 represents the other component[73]. This lobed component is nearly stoichiometric and has high velocity of ~ 104 m/s which is sufficiently beyond the thermal velocity and provides energetic particles of ~ 40 eV, shown schematically in figure 2.4 as a function of n . The key feature of PLD is to use this high kinetic energy to improve film crystallinity and structures, trigger reactions for the dissociation of gas molecule like O_2 , and helps to increase the stoichiometric vapor and eliminate some of the nonstoichiometric thermal components[46], [71], [73].

2.5 Structural Characterization

This section is dedicated to describing the basic principles and techniques that were utilized for the structural characterization of all the thin films. Depositing high quality thin films truly depends on finding the optimize growth conditions which could be realized by appropriate structural characterization techniques. It also helped us to measure the micro structural properties of the films such as surface morphology, crystallinity and thicknesses

and their relationship with different material properties such as conductivity, polarization and magnetization, etc. From X-ray Diffraction (XRD) analysis, different crystalline structure and phase orientation of the thin films were determined. Chemical purity, stoichiometry and bonding nature of different elements were confirmed by the Energy Dispersive X-ray Spectroscopy (EDS) and X-ray Photoelectron Spectroscopy (XPS). Surface morphology of the thin films was studied using the Scanning Electron Microscope (SEM) and the Atomic Force Microscope (AFM) and interface quality was evaluated by Transmission Electron Microscope (TEM).

2.5.1 X-ray Diffraction

X-ray diffraction (XRD) is a widely used multipurpose, non-destructive measurement technique that exhibits complete information of crystallographic structure of natural and manufactured materials[75]. In this study, XRD measurements on thin film heterostructures were carried out on a Rigaku SmartLab X-ray diffractometer operating at 40 kV and 40 mA, and equipped with Cu K α radiation at a wavelength $\lambda = 1.540562 \text{ \AA}$. For full characterization of epitaxially grown thin film heterostructures, a standard set of XRD measurements were performed which includes θ - 2θ scan, Rocking curve and in-plane Phi (ϕ) scan. The basic principle of XRD is based on Bragg’s law given by:

$$2d\sin\theta=n\lambda\text{.....}2.4$$

where θ is the angle of incidence of the X-rays, λ is the wavelength of the X-rays, and n is

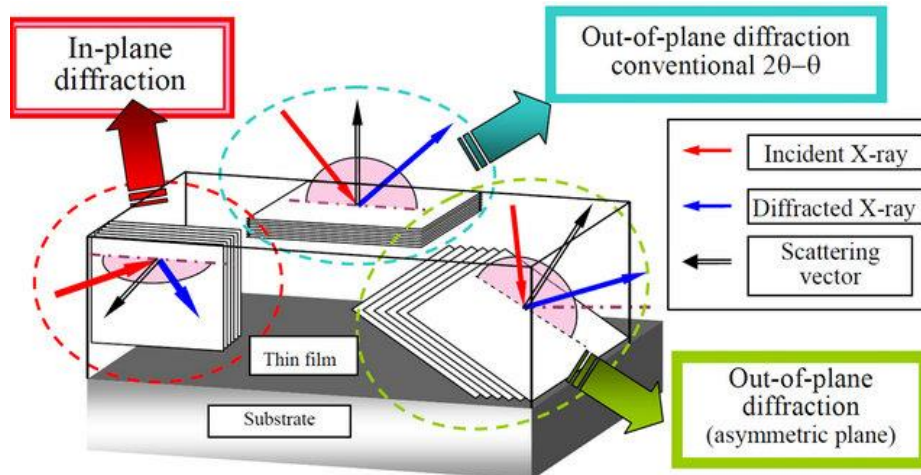


Figure 2.5: Schematic diagram of the geometries of thin film X-ray diffraction measurement, showing relations between the lattice planes of a thin film sample and X-ray geometries[76]–[78].

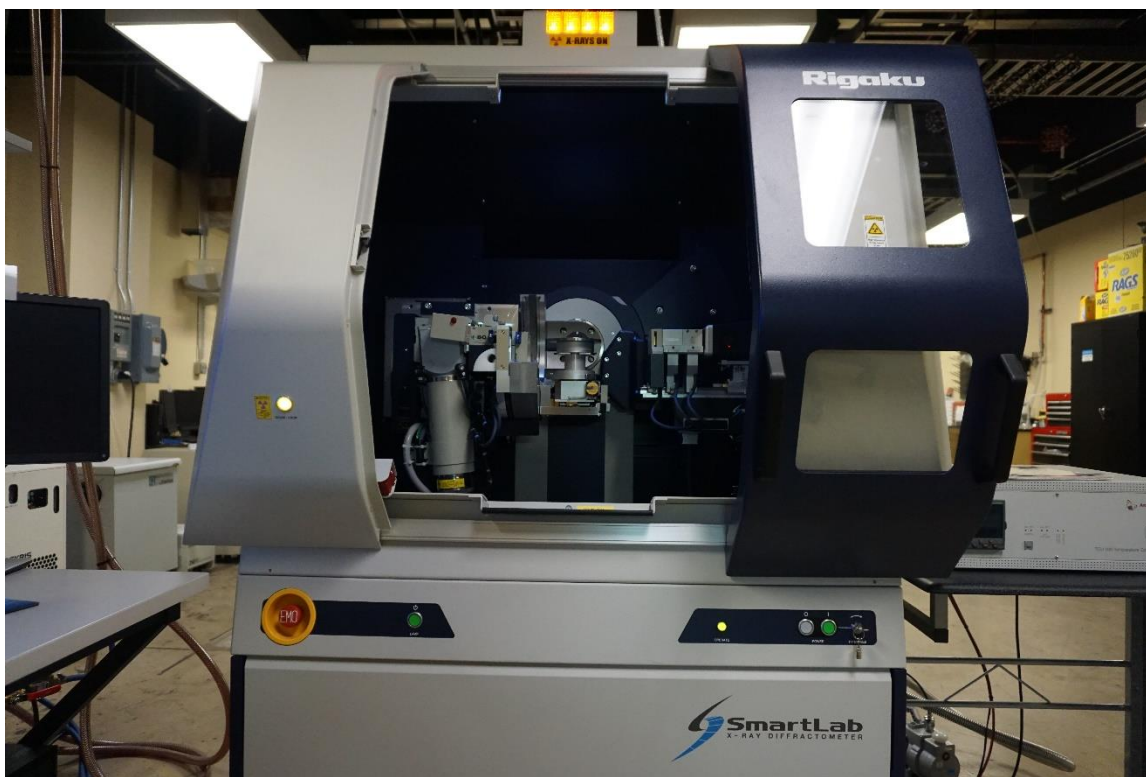


Figure 2.6: The state of the art in highly automated, fully modular, multipurpose Rigaku SmartLab X-ray Diffractometer of Texas State University.

a positive integer representing the order of the diffraction peak[79]–[81]. Figure 2.5 shows

an incident beam of parallel X-rays impinging the crystal surface at an angle θ and reflected from the parallel planes of atoms formed by the crystal lattice of the material. It also shows the measurement geometries for various types of XRD measurement such as out-of-plane and in-plane. There will be always a phase difference between two consecutive reflected beams because they travel a different path. Now, constructive interference of the reflected beams will only occur if their path difference is an integer multiple of the wavelength of the X-rays as given in equation 2.4, otherwise it will have a destructive interference. Due to the constructive interference according to Bragg's law, characteristic diffraction pattern is generated which is then collected and plotted as intensity (I) versus 2θ graph. The recorded pattern can then be compared with a known crystallographic database of reference patterns known as indexing to determine the crystal structure of the film.

2.5.2 Scanning Electron Microscopy

Scanning Electron Microscope (SEM) is one of the most extensively used techniques to characterize the surface morphology and cross-section of the thin films. In this work, all the imaging was performed using a FEI Helios NanoLab 400 DualBeam system. This is a completely digital Field Emission Scanning Electron Microscope (FE-SEM) which is coupled with Focused Ion Beam (FIB) capability. The DualBeam facility delivers the highest performance for sample preparation, imaging, 3D characterization, nano-prototyping, semiconductor failure analysis and process control. Figures 2.7 (a, b) shows a schematic diagram of the electron beam path inside the electron gun column and the major components of the SEM: the electron gun column, specimen chamber and control system. The electron gun column of SEM consists of an electron gun and magnetic lenses shown in figure 2.7 (a). The Helios NanoLab 400 comes with ultra-

high resolution electron optics which can provide optimal working distance of 0.9 nm at 15 kV operating voltage and 1.0 nm at the DualBeam corresponding point and 350 V – 30 kV beam voltage range. The base of the electron beam column is the specimen chamber which is kept at high vacuum of about $\sim 10^{-6}$ Torr during operation. The electron gun itself consists of three components which are tungsten wire filament acting as cathode, grid cap and anode (Figure 2.7 a). A reasonably high current is supplied to the tungsten filament to increase filament

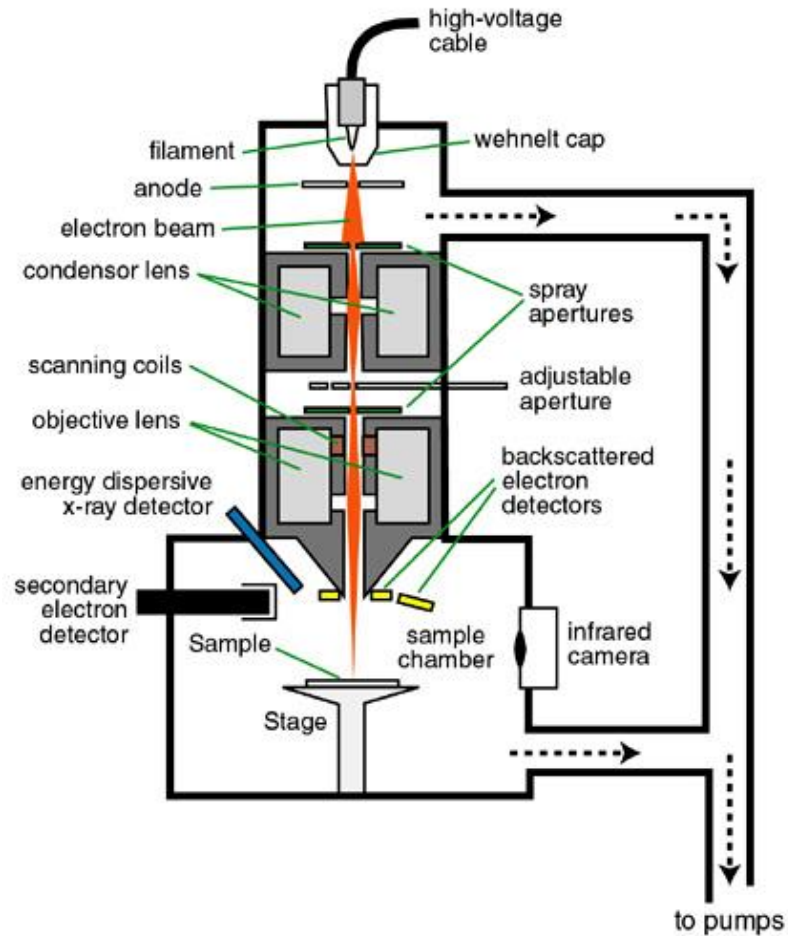


Figure 2.7: (a) Schematic scanning electron microscope overview[82].

temperature at around $\sim 2000-2700$ K by resistive heating process which generates free

electrons by thermionic emission and accelerates them to energy up to $\sim 0.1\text{--}30$ keV[83]. A combination of several different magnetic lenses is used to focus the electron beam to a small spot on the specimen and scanning the specimen for imaging. Various signals including secondary electrons (SEs), backscattered electrons (BSEs), Auger electrons, X-rays and cathodoluminescence are generated due to the interaction between the focused



Figure 2.7: (b) Helios NanoLab 400 for Scanning Electron Microscope imaging.

electron beam and sample specimen. These signals are recorded by several detectors and

can be analyzed to retrieve different types of information about the sample, for example, SEs normally contain the information about the specimen surface and mostly used for general purpose imaging[83]. However, BSEs can be used to provide information about the composition because they mostly interact with the positively charged nucleus of the specimen and are typically scattered at large angles in the range of $\sim 0^\circ$ to 180° . The Helios NanoLab 400 comes with a 5-axis motorized x-y-z-rotate-tilt stage which is piezo controlled, provide flexibility to travel 100 mm along the x and y-axes and tilt the sample in the range of ~ -10 to $+60$ degrees to capture the best quality images with high resolution. It also delivers Energy Dispersive X-ray Spectroscopy (EDS) using a 30 mm^2 Silicon Drift Detector (SDD) with less than 133 eV resolution (TEAM EDX with Apollo XL SDD). The resolution of compositional analysis is limited to 30 nm for thin samples. Moreover, it also has a retractable detector for STEM which enables scanning transmission imaging in bright field, dark field, and high-angle dark field modes with a 0.8nm resolution.

2.5.3 X-ray Photoelectron Spectroscopy

Chemical and elemental analysis of inorganic solid materials with electron spectroscopy is based on the number of secondary electrons that are emitted due to the excitation by photons, electrons, ions, or neutrals and their energy analysis[84]. X-ray Photoelectron Spectroscopy is mostly used to investigate the bonding configurations of surface atoms within the top 2-5 nm of a thin film specimen where soft X-ray radiation either from Al and/or Mg sources is directed towards the sample to induce emission of inner shell electrons[85]. Therefore, ionized states are formed which emit photoelectrons with kinetic energy given approximately by the difference between the photon energy and binding energy. The recorded photoelectron spectrum is hence a direct representation of

the binding energies of the electrons coming from different atomic levels. This binding energy can be calibrated to eV very often and lower kinetic energy gives

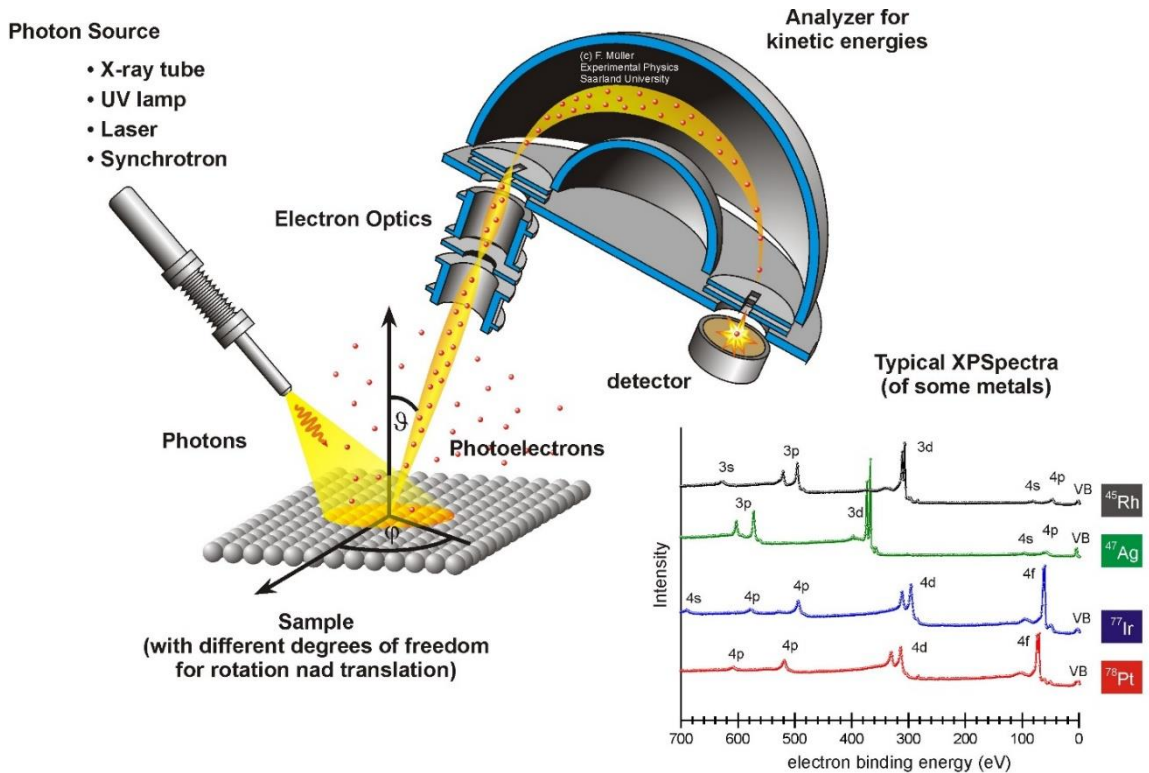


Figure 2.8: (a) Schematic drawing of a typical XPS setup with different photon source such as X-rays, UV-light, laser and Synchrotron radiation, a sample manipulation with different linear and rotational degrees of freedom, electron optics, an energy dispersive analyzer and a detector. XPS spectra (intensity vs. binding energy) are shown for four different metals with their element specific distribution of core level photoemission[86].

higher binding energy. Usually, kinetic energy is plotted on the x-axis with increasing energy to the right then binding energy should increase from right to left. By considering both the inelastic and elastic scattering mechanism, mean free path of the photoelectrons

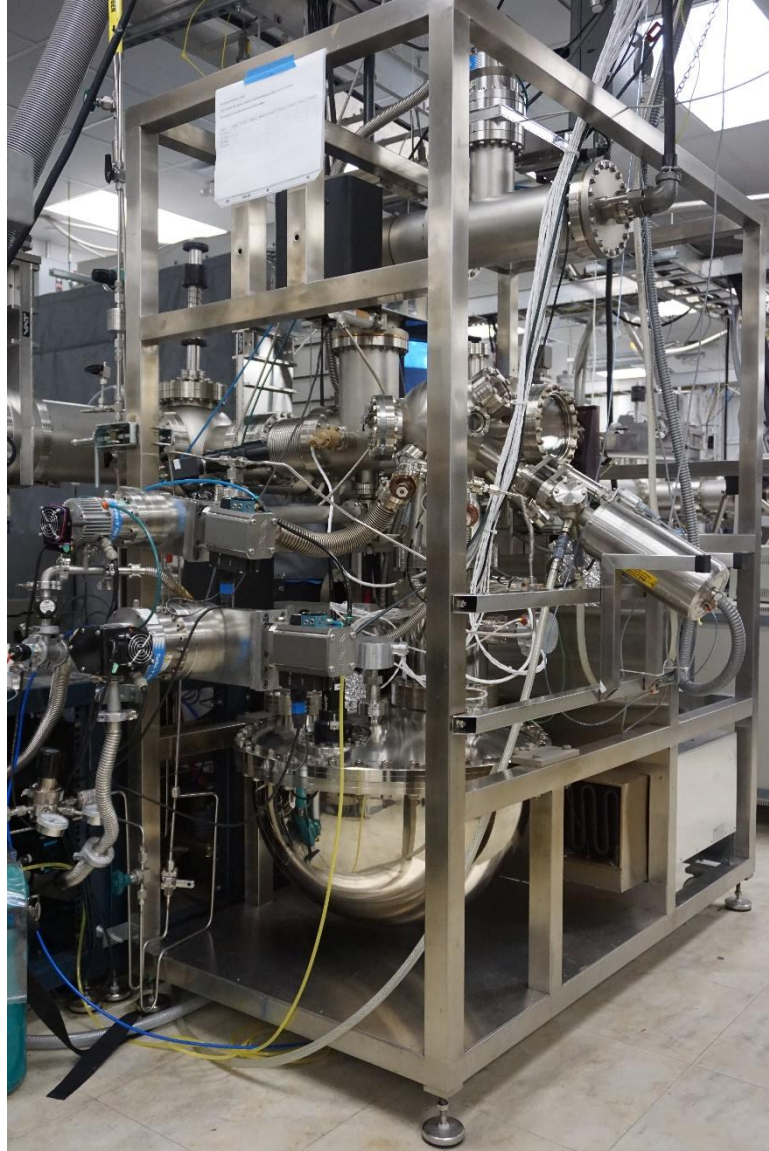


Figure 2.8: (b) X-ray photoelectron spectroscopy from SPECS Surface Nano Analysis.

can be determined from the probability of a photoelectron to suffer an energy loss. However, the attenuation length can be determined from the probability of a photoelectron to be successfully received by the electron energy analyzer[87]–[89]. In both cases, information depth is limited to the nanometer region which is determined by the kinetic energy and instrumentation matrix. As a result, XPS as well as Auger Electron Spectroscopy (AES) analysis are surface specific or sensitive. Unlike AES, there are no

primary electrons in XPS which usually allows for a much smoother background so that peaks could be readily measured directly from the spectrum.

The basic components of a typical AES or XPS instrument are an ultrahigh vacuum (UHV) chamber which contains the sample stage, electron energy analyzer and detection system shown in figure 2.8 (b). It also consists of an electron gun for AES or an X-ray source with or without monochromatic for XPS, and an ion gun for sample cleaning and depth profiling[84]. Outside the UHV system are control consoles or hardware with other electronics supply systems and a computer installed with data acquisition and processing software. The qualitative analysis of XPS spectra is comparatively easy since it only requires comparing the measured data with tabulated electron level energies and handbook spectra but quantitative analysis is more complicated due to requirement of data fittings.

2.5.4 Atomic Force Microscopy

Atomic Force Microscope (AFM) is a type of scanning probe technique that measures the surface morphology or topography of a specimen with very high resolution by utilizing a sharp tip within the close proximity and scanning area can be chosen from the surface of interest at very small spatial intervals [47]. Unlike the working principle of a phonograph or profilometer, AFM works much the same way at nano-scale [90], [91]. As shown in figure 2.9 (a), a sharp tip with a radius of few nm in combination with a cantilever is dragged on the sample surface. In AFM, the probing tip maintains a close proximity with

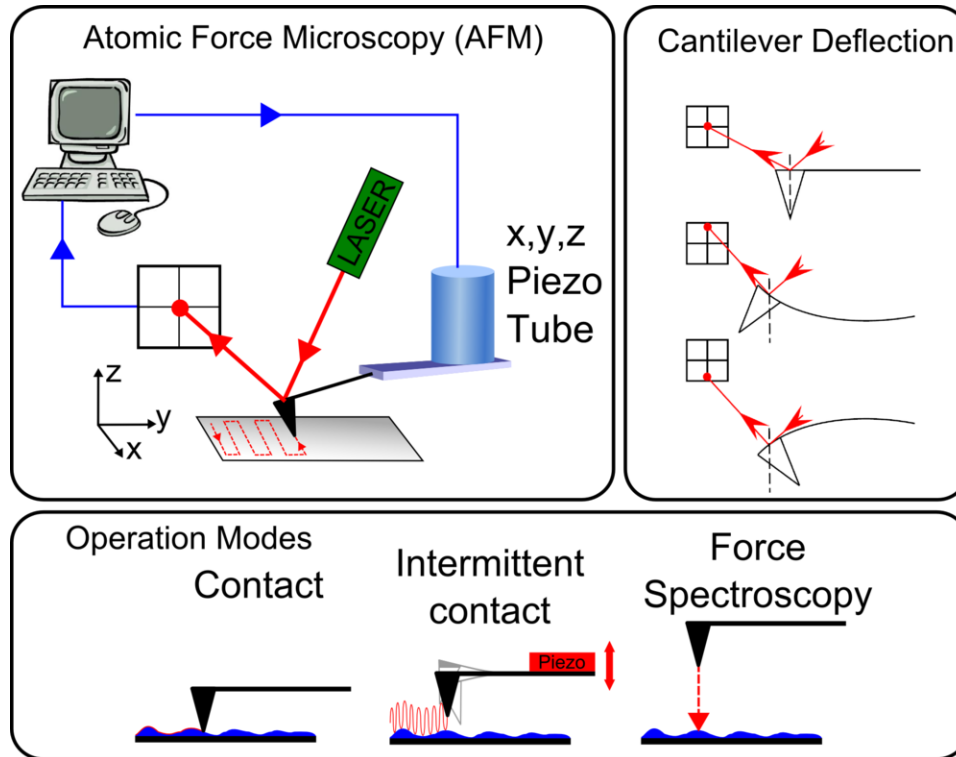


Figure 2.9: (a) Typical schematics of atomic force microscope for working in different modes[92].

the sample surface during the scan and the Van der Waals forces between the atoms of tip and the surface gets affected due to the changes of surface height. This changes of Van der Waals forces creates a vertical deflection of the cantilever which is directly reflected to the topography of the surface. This vertical deflection can be recorded as a shift of the reflected laser beam from the top of the cantilever which is sensed by a photodiode [90], [91], [93]. A three-dimensional image containing the surface features can be formed simply by collecting the height data for a succession of lines. Figure 2.9 (b) shows the major components of the Park XE7 Atomic Force Microscope that was used to scan the surfaces of the thin films in this work.

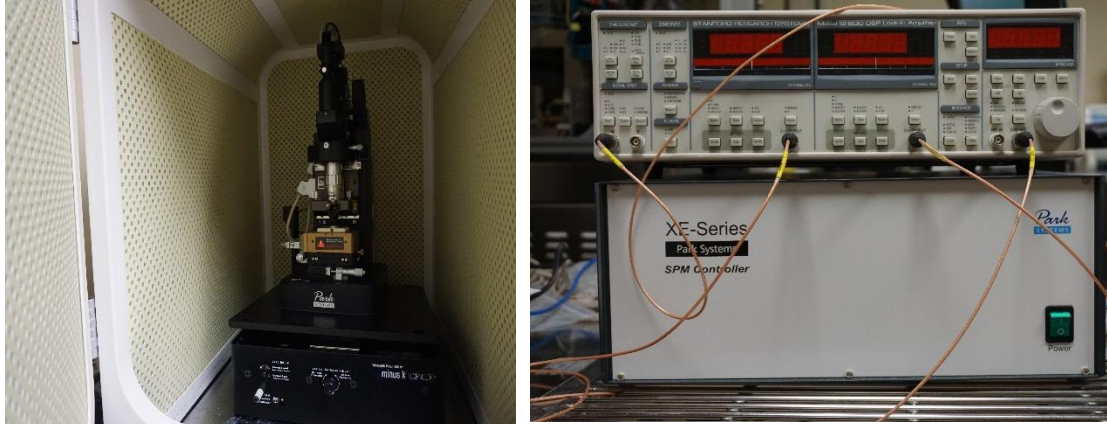


Figure 2.9: (b) Park XE7 atomic force microscope which is the most affordable research grade AFM with flexible sample handling.

2.6 Electrical Characterization

To measure electrical properties of the thin film heterostructures, Ti/Au electrode with various size and shape and a thickness of ~ 50 nm/100 nm respectively was deposited by Electron Beam deposition technique (Angstrom Engineering, EvoVac) on the top surface of the thin film covered by a shadow mask or through standard lift-off process. After post-anneal treatment under 450 °C and an Ar environment, ferroelectric, dielectric and multiferroic capacitors with good film/electrode metallization contact were formed. All the electric behaviors were measured across the thickness.

2.6.1 C-V and Dielectric Measurement

Voltage-dependent current (I-V) or current density can determine the insulating nature of the complex oxide materials. To obtain a good ferroelectric polarization, robust insulating behavior is required and I-V measurement will further predict the tolerable polling or biasing voltage limit during piezo-response force microscopy (PFM). In this

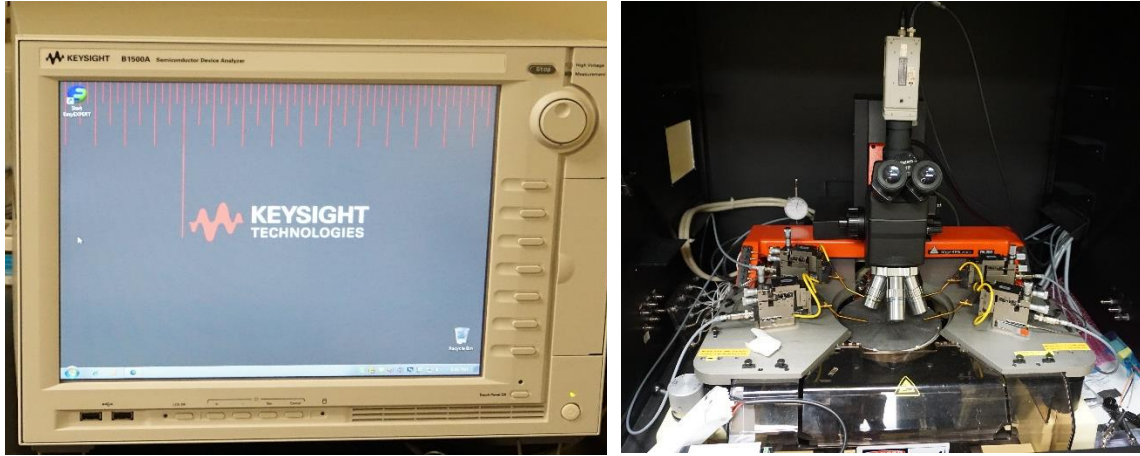


Figure 2.10: (a) Semiconductor device analyzer of Keysight B1500A with multi-probe station, an all in one analyzer supporting IV, CV, pulse/dynamic IV which is designed for all-round characterization from basic to cutting-edge applications.

work, (I-V) characteristics curve of all the thin film heterostructures were measured using a semiconductor device analyzer ((Keysight B1500A, shown in figure 2.10 (a)). Dielectric constant or relative permittivity of a material reflects its ability to store electrical energy relative to the permittivity under vacuum when an electrical potential is applied. More specifically, dielectric constant is a materials characteristic which is irrelevant to its dimension, shape, or mass. Spectroscopic dielectric behaviors of the BFO/LSMO multilayered heterostructures were measured by a precision impedance analyzer ((Wayne Kerr 6500B, shown in figure 2.10 (b)). A small ac electric field of 1.0 V was applied during the measurement and dielectric constant can be determined using the flowing expression:

$$\epsilon = \frac{Cd}{\epsilon_0 A} \dots \dots \dots 2.5$$

where ϵ is the dielectric constant, ϵ_0 the dielectric constant in free space, C the capacitance, A the area of the capacitor and d is the film thickness. The spectroscopic dielectric constant can be calculated from the measured frequency-dependent capacitance of the capacitor.

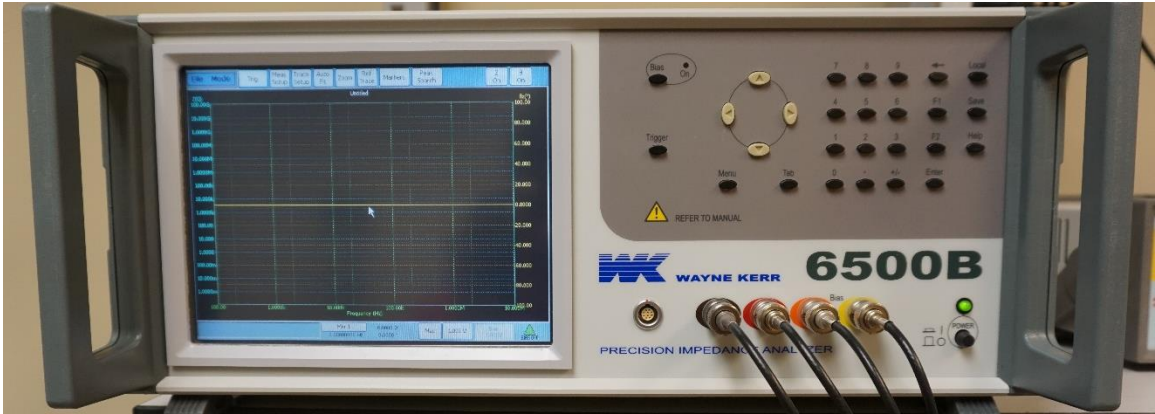


Figure 2.10: (b) Precision impedance analyzers 6500B from Wayne Kerr electronics.

2.6.2 Ferroelectric Characterization

The ferroelectric polarization and switching behaviors of materials under an electric field can be characterized by the ferroelectric hysteresis loop. Polarization-electric field (P-E) hysteresis loop of a ferroelectric or multiferroic material and the corresponding polarization state is described in figure 2.11 (a) below where P_s , P_r , and E_c are the saturated polarization, remnant polarization and ferroelectric coercive field, respectively [94]. During the P-E measurement, ferroelectric crystal initially shows polydomain structure which is also known the as-grown state but single domain state can be accomplished by applying an external electric field to cause the dipoles to align in certain direction. Ferroelectric domain will switch back if the electric field is reversed and reaches the coercive field. The ferroelectric properties of the thin films were measured using a Precision LC Materials Analyzer from Radiant Technologies shown in figure 2.11b. The precision LC materials analyzer is connected to a probe station which includes a sample stage holder with associated micro-manipulators.

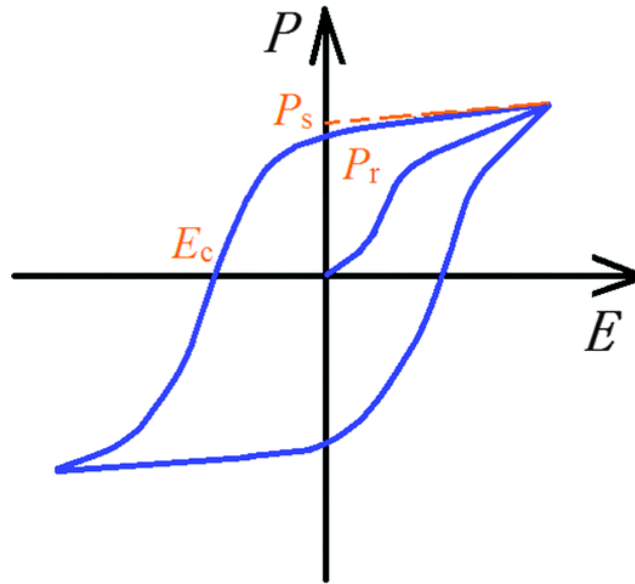


Figure 2.11: (a) A typical ferroelectric hysteresis loop showing the spontaneous polarization (P_s), the remnant polarization (P_r) and the coercive field (E_c) [95].



Figure 2.11: (b) Precision LC II ferroelectric test system from Radiant technologies inc.

2.6.3 Piezo-response Force Microscopy

For imaging and measuring surfaces on a nanometer scale down to the level of molecules or groups of atoms, scanning probe microscopy (SPM) offers numerous related techniques such as atomic force microscopy for topography imaging, piezoresponse force

microscopy (PFM) for ferroelectric domain mapping, magnetic force microscopy for magnetic domain mapping, scanning tunneling microscopy to obtain high resolution surface morphology, etc. Of them, PFM is a powerful technique that employs the piezoelectric effect of materials to generate contrast that can be used to characterize the ferroelectric and multiferroic thin films [96], [97]. The schematic of a PFM setup and its working principle is given in figure 2.12 below.

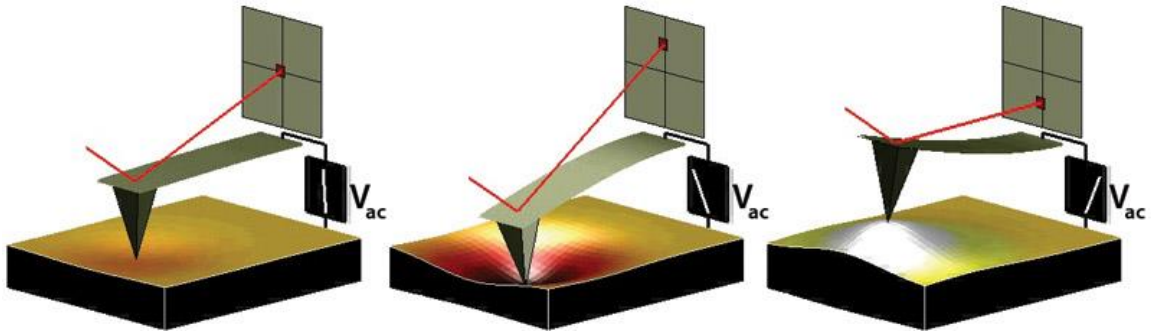


Figure 2.12: Depiction of PFM operation. The sample deforms in response to the applied voltage. This, in turn, causes the cantilever to deflect, which can then be measured and interpreted in terms of the piezoelectric properties of the sample [96].

In this study, ferroelectric domains and switching properties of all the thin film heterostructures were acquired by a scanning probe microscope (Park XE7). In our experiments, Pt, Pt-Ir, Cr-PtIr, Cr-Au and Au coated conductive probes were used for the contact mode PFM imaging.

2.7 Magnetic Characterization

2.7.1 Vibrating Sample Magnetometer

Vibrating sample magnetometer (VSM) is a scientific instrument that can measure magnetic behaviors, in which a sample is positioned in a uniform magnetic field to be magnetized. In the VSM measurement, a continuous sinusoidal vibration is applied on the sample and the pickup coil precisely record the induced voltage from the magnetic moment

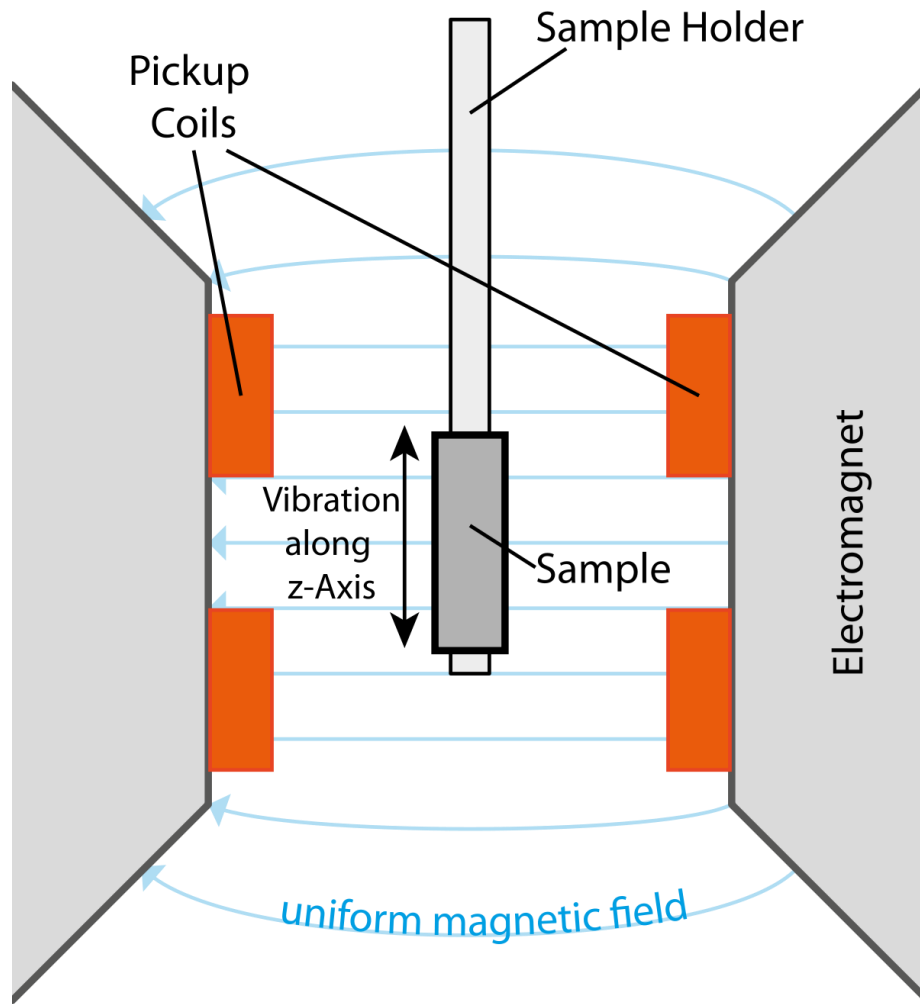


Figure 2.13: (a) Typical schematic of vibrating sample magnetometer [98].

which is also proportional to the sample's magnetization. The induced voltage does not depend on the strength of the applied magnetic field, instead it depends on the sample volume. Therefore, it is possible to measure the magnetic-field-dependent magnetization hysteresis curve of the materials by simply detecting the induced voltage. Figure 2.13 (a) shows the schematic diagram of a vibrating sample magnetometer. The magnetic hysteresis loops of multiferroic-ferromagnetic heterostructures were obtained by utilizing the VSM module of Physical Properties Measurement System (PPMS, Quantum Design) shown in figure 2.13 (b). The PPMS provides a suitable sample environment that permits various

measurements to be performed in a cryogenic temperature-field environment. Moreover, electrical and magneto-optical measurements can also be performed at temperatures from 1.9K up to 310K under magnetic fields from -9 to 9 Tesla.



Figure 2.13: (b) Physical Prosperities Measurement System (PPMS) from quantum design.

III. GROWTH AND CHARACTERIZATION OF STO ON GaAs AND BiFeO₃ THIN FILMS ON STO/GaAs

3.1 Introduction

Integration of multiferroic materials with semiconductors has attracted considerable attention in recent years, not only for the fundamental physics, but also due to their potential applications in future system-on-a-chip devices. BiFeO₃ is a unique type of multifunctional material that simultaneously exhibits two or more ferroic orders such as ferroelectricity, anti-ferromagnetism with remarkable optical properties at room temperature[4]. Consequently, BFO is emerging as a promising candidate for designing multifunctional devices that include novel high density magnetic storage memories, which can be electrically written and magnetically read; electrochemical sensors; ferroelectric photovoltaic devices; high frequency magnetic devices; micro actuators; etc.[4], [99]–[101]. Many other perovskite-type oxide materials such as BiMnO₃ and TbMnO₃ have also recently attracted attention since their magnetization and dielectric polarization are expected to be coupled because of the magnetic and dielectric interaction present in these materials[22]. However, BFO continues to be an attractive material because of its G-type antiferromagnetic structure resulting in a weak ferromagnetic ordering due to a canted spin structure with a high antiferromagnetic Néel temperature (T_N) of 643 K and a high ferroelectric ordering with a Curie temperature (T_C) of 1103 K[102]. In addition, BFO is also being considered as a “green” alternative to lead based ferroelectric materials. It crystallizes in a rhombohedrally distorted perovskite structure with the lattice constants of ($a=b=c=3.96 \text{ \AA}$ and $\alpha=\beta=\gamma=89.4^\circ$). Furthermore, it plays a key role in rejuvenating the field of magnetic ferroelectric (magneto-electric) materials[103], [104].

For practical applications, the direct growth of the BFO on commonly used semiconductors, such as Si, GaAs and GaN has been of great interest. But, because of the lattice mismatch and incompatible growth environments the epitaxial growth of BFO directly on semiconductor presents a challenge. Therefore, a buffer layer is commonly used to realize epitaxial growth of these structures on semiconductors. Generally, many related studies have focused on the use of silicon for the integration of functional materials and devices including ferroelectric field effect transistor (Fe-FET)[105], and multiferroic based spin valves[106]. These systems on silicon have demonstrated the possibility of integration of added functionality onto semiconductor devices. Recently compound semiconductors were used as substrates for the growth of ferroelectric perovskite oxides which is driven by the potential applications of multifunctional devices[107], [108]. Among these semiconductors GaAs, for example, has a high saturated electron velocity and mobility allowing transistors based on GaAs to operate at a much higher frequency with less noise compared to Si. However, the integration of functional oxides onto the III–V’s semiconductor technology still presents a significant challenge. Only a few attempts have been made so far to integrate functional oxides with GaAs for exploiting them for novel electronic device. For instance, Gao et al. reported the epitaxial growth behavior and the multiferroic properties of Mn-doped BFO grown on GaAs (001) with a Nb doped SrTiO₃ (NSTO) buffer layer[109]. Huang et al. also investigated the electrical transport property of BFO/NSTO/p-GaAs heterostructure by temperature dependent I-V characteristics[110]. These studies utilized PLD to deposit the oxide films directly on GaAs resulting a poor interface quality between the STO and GaAs. In general, the film properties are greatly dependent on interface quality. In this study, STO on GaAs (001) were epitaxially grown

by molecular beam epitaxy (MBE), and as a result obtained a high-quality interface. This facilitates the effort for integration of multifunctional oxides on GaAs by using STO/GaAs as a virtual substrate.

BFO has been studied extensively due to its interesting ferroelectric polarization, high Curie temperature, and multiferroic properties. Recently, some results suggest that BFO can also exhibit photovoltaic effect[111]. This adds to the realm of potential applications for BFO in optoelectronic devices integrated with GaAs, which is a direct band gap semiconductor with superior optoelectronic properties[112]. However, there has been only small number of reports on the investigation of BFO films grown on GaAs substrates. So far, there has been no report on the optical properties of BFO thin films grown on STO buffered GaAs substrate in spite of the fact that III-V semiconductors integration with BFO would facilitate the studies of their optoelectronic and ferroelectric properties in order to evaluate its potential for the development of novel devices encompassing multiple applications. The epitaxial growth and properties of multiferroic BFO films on GaAs (001) with STO as a buffer/template was reported in this chapter.

3.2 Growing SrTiO₃ on GaAs (001) by Molecular Beam Epitaxy

Heteroepitaxy of oxides with III-V semiconductor not only serves as potential gate dielectrics for MOSFET applications in future CMOS but can also be used as a virtual substrate for the integration of other multifunctional oxides that has ferroelectric, ferromagnet and multiferroic properties with high speed opto-electronics afforded by compound semiconductors. The deposition of high quality epitaxial oxides on semiconductor, viz. SrTiO₃ (STO) with controlled interface offers many benefits such as low defects and favorable band offset to unpin Fermi level at the oxide-semiconductor

interface[113]. Molecular beam epitaxy (MBE) has proven to be a versatile growth process for controlling deposition parameters to tailor the interfacial layer. Epitaxial growth of STO on Si (001) by MBE using 1/2 monolayer (ML) of Sr on clean Si (001) as a template was first demonstrated by McKee and co-workers[10]. The 1/2 ML coverage by Sr inhibit formation of an amorphous SiO₂ layer during the subsequent STO deposition in a relatively wide range of temperatures and pressures [10], [11].

The first reported single crystal STO growth on GaAs was carried out by MBE and structural characterization determined that the interface was sharp with a crystalline transition across the oxide/GaAs interface without the formation of an amorphous interfacial layer [114]. Epitaxial STO films were also grown on GaAs substrates without any buffer layers using laser molecular beam epitaxy technique [115]. However, STO grown on GaAs with techniques other than MBE will provide a poor interface between STO/GaAs due to the uncontrolled GaAs surface oxide removal. In this study, ½ ML Ti or ½ ML Sr as pre-layer was used on a MBE grown GaAs epitaxial layer prior to the deposition of the STO layer.

3.2.1. Experiment

Epitaxial growth of STO on GaAs were carried out in a cluster UHV system including MBE chambers for compound semiconductors and oxides. In addition, X-ray photoemission spectroscopy (XPS) chamber is also connected to the multi-chamber system for probing the surfaces and interfaces without exposure to atmosphere. For STO deposition on GaAs, this multi-chamber system is important as it keeps the GaAs surface clean and well-ordered for subsequent deposition and removes artifacts during XPS analysis. The III-V chamber was kept with base pressure of $<5 \times 10^{-10}$ mbar by using a

combination of ion and cryogenic pumping. Growth rates and temperatures for the GaAs growth were determined using typical reflection high energy electron diffraction (RHEED) oscillation technique and optical pyrometer respectively. The oxide chamber consists of 2 electron beam evaporators, 7 effusion cells, an oxygen plasma source and kept at a base pressure of $<5 \times 10^{-10}$ mbar by using a combination of turbomolecular pump and cryo pump. Sr and Ti metals from effusion cells and high purity molecular oxygen were used as deposition sources. The chamber ion gauge used to measure oxygen flux. A quartz crystal monitor was used to determine Sr and Ti flux but the growth rates and stoichiometry of STO were determined using RHEED technique.

To facilitate oxide integration, typically a layer of $\sim 0.5 \mu\text{m}$ of n-GaAs or p-GaAs doped at a level of $2 \times 10^{16} \text{ cm}^{-3}$ grown at a substrate temperature of 580°C and a growth rate of 0.8 MLs/sec on an n^+ or p^+ GaAs substrate. After GaAs deposition the wafers were cooled under As flux until the temperature is $<300^\circ\text{C}$ and then transferred into the oxide chamber for the oxide growth. Once in the oxide chamber, a $\frac{1}{2}$ ML Ti was deposited onto the c(4x4) As stabilized GaAs surface. The initial nucleation of the oxide layer was always carried out using a low flux of molecular oxygen to prevent the oxidation and the disruption of the Ti templated GaAs surface. The use of a plasma source during nucleation or template layer deposition can oxidize the GaAs surface creating amorphous Ga and As oxides that can further prevent the nucleation of crystalline oxide films. Consequently, the oxide growth was carried out using molecular oxygen. The oxide nucleation comprised of co-deposition of Sr, Ti and oxygen at a level of $1-3 \times 10^{-8}$ mbar with a substrate temperature of 300°C for a total thickness of 1 unit cell or $\sim 3.9 \text{ \AA}$. This was followed by an annealing at 500°C for 3 minutes after which co-deposition of STO was continued at 500°C until the desired

thickness was achieved. RHEED is used throughout the growth to ensure stoichiometric oxide growth[113].

3.2.2 Results and Discussion

Based on the temperature and As coverage two different As stabilized GaAs nucleation surface identified by RHEED are the $c(4 \times 4)$ appears at low temperature $< 450^\circ\text{C}$ shown in figure 3.1(a) and (2×4) appears at comparatively high temperature $> 500^\circ\text{C}$ shown in figure 3.1(b). During the $\frac{1}{2}$ ML Ti deposition the surface reconstruction changed from $c(4 \times 4)$ to a (2×1) shown in figure 3.1(c) and for $\frac{1}{2}$ ML Sr the surface reconstruction changed from $c(4 \times 4)$ to a (2×2) shown in figure 3.1(e). Template layer formation on (2×4) As stabilized GaAs nucleation surface was also successfully done shown in figure 3.1(d) and (f) to deposit crystalline STO.

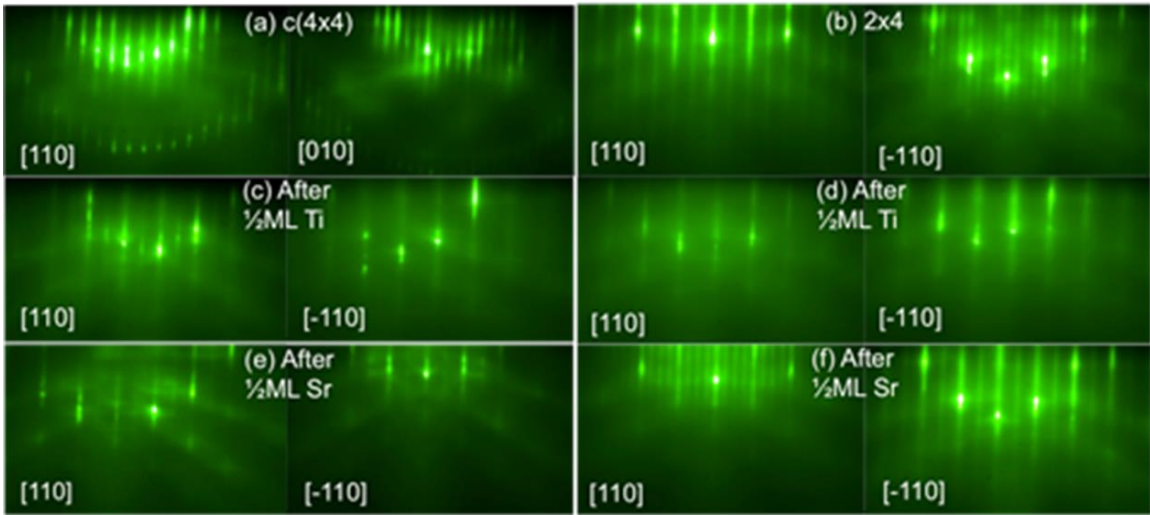


Figure 3.1: (a) RHEED patterns along GaAs [110] and [010] azimuth for $c(4 \times 4)$ As stabilized GaAs surface. (b) RHEED patterns along GaAs [-110] and [110] azimuth for (2×4) As stabilized GaAs surface. (c and d) RHEED pattern shows surface reconstruction changed to a (2×1) after the deposition of the Ti pre-layer along the [-110] and [110] for $c(4 \times 4)$ and (2×4) GaAs surface respectively. (e and f) RHEED pattern shows surface reconstruction changed to a (2×2) after the deposition of the Sr pre-layer along the [-110] and [110] for $c(4 \times 4)$ and (2×4) GaAs surface respectively.

Following the template layer deposition, oxygen was introduced to a level of $1-3 \times 10^{-8}$ mbar and Sr, Ti shutters were also opened. After depositing 1 unit cell of STO, the oxygen valve was closed and the substrate was annealed at 500°C for 3 mins. The growth of the STO layer was then continued using co-deposition but with a higher molecular oxygen level of 1×10^{-7} mbar. Figure 3.2 shows the RHEED pattern along the STO [110] and [010] azimuths after the deposition 100\AA STO layer on GaAs displaying characteristics of a stoichiometric STO growth with well-ordered and smooth surface.

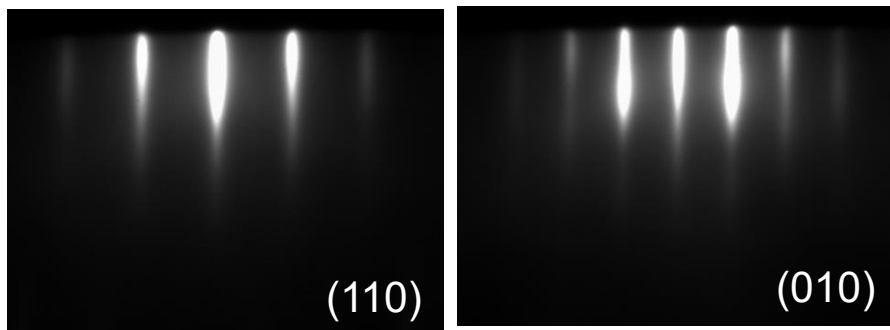


Figure 3.2: RHEED patterns along the [110] and the [010] respectively after the deposition of 100\AA STO.

The crystal structure of the STO/GaAs were determined by XRD. Figure 3.3 shows the theta-2theta XRD survey scan, indicating (001) oriented STO films. No other STO orientations or phases were detected other than peaks attributed from GaAs substrate. This STO/GaAs is used as the virtual substrate for other subsequent oxide growth using pulsed laser deposition presented in this work.

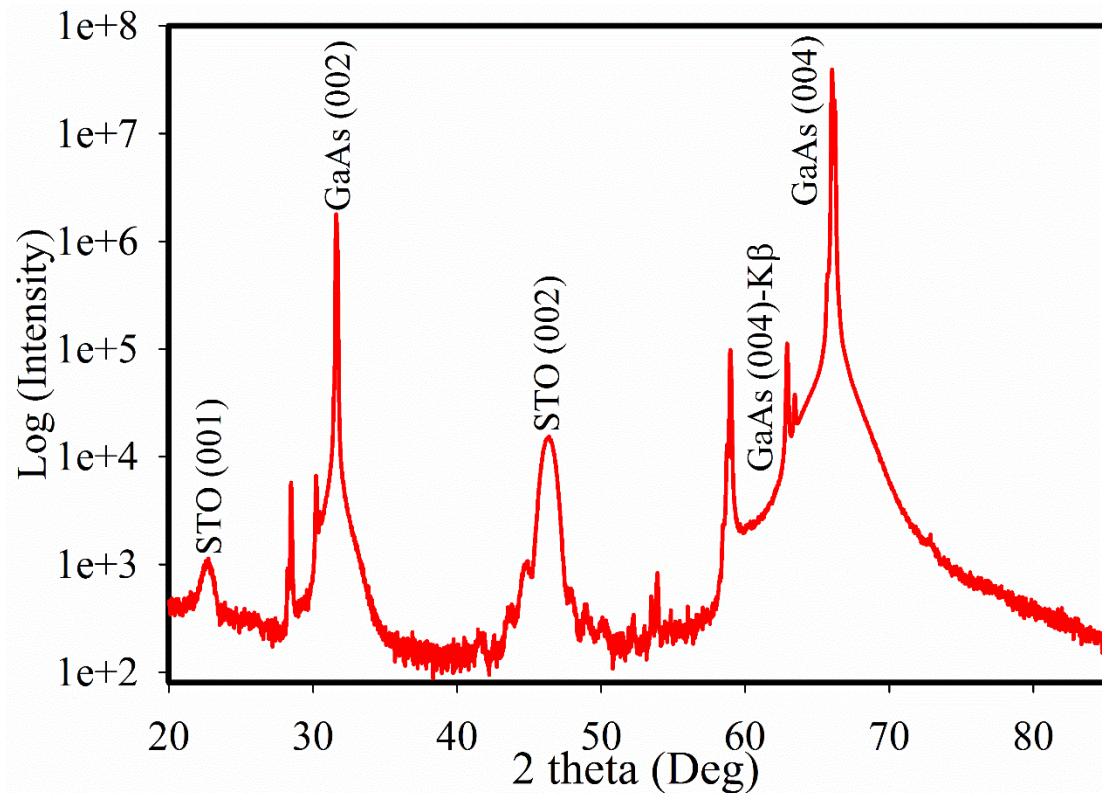


Figure 3.3: XRD theta-2theta scan of the STO on GaAs showing (001) oriented oxide film.

3.3 Experimental Design and Characterization of BFO Growth

BFO films were grown on 5 nm ultrathin STO (001) buffered GaAs (001) by pulsed laser deposition (PLD) using KrF Excimer laser ($\lambda=248$ nm). The STO buffer layer on GaAs was deposited using molecular beam epitaxy (MBE) which is an ideal technique for the nucleation of a crystalline oxide film on semiconductors as it allows for the control of the crystalline surface on exposure to oxygen. The experimental details on the growth of STO on GaAs (001) can be found in previous published reports[11], [114]. For the PLD growth of BFO, the substrate to target distance was approximately 6.8 cm and the BFO thin film was deposited at 600°C, with 100 mTorr oxygen using 300 mJ of Excimer laser energy with 10 Hz laser fluency. After BFO deposition, the sample was in-situ annealed at 500°C for 1 hour under partial oxygen pressure. During growth, the substrate and target

were rotated continuously to provide uniform growth and ablation of the target.

The crystalline structure of the deposited thin films was identified by X-ray diffraction (XRD, Rigaku Smartlab). To determine the Fe and Bi oxidation states, X-ray photoelectron spectroscopy (XPS) was used. The surface morphology and piezoresponse measurements were carried using a scanning probe microscope (Park XE7). To investigate the optical properties, spectroscopic ellipsometry (SE) measurements were taken using a J.A Wollam, M-2000 variable angle ellipsometer. In order to measure the ferroelectric P-E hysteresis loop, circular Pt electrodes were fabricated on the thin films by sputtering through a shadow mask and the ferroelectric hysteresis loop (P-E) were measured using a ferroelectric testing system (Radiant Technologies, USA). The magnetic measurements were taken in a Quantum Design Physical Properties Measurement System (PPMS) using the vibrating sample magnetometer (VSM) option.

3.4 Result and Discussion

Figure 3.4 shows the XRD pattern of a BFO film grown on STO buffered GaAs (001). The distinct peaks of BFO and GaAs in the spectra suggest single-phase films and shows no evidence of secondary phases such as Bi_2O_3 , Fe_2O_3 , and FeO that are found for films grown under non-optimized conditions. Only (001) reflections from BFO films were observed along with the GaAs (001) reflections suggesting that the films are exclusively [001] epitaxial grown. The excellent film crystallinity is further confirmed by the full width at half maximum (FWHM) value of 0.27° for the rocking curve for the BFO (001) peak. For comparison, a range of 0.17° - 0.26° of FWHM was reported for PLD grown BFO films on STO (001) substrates[116], [117].

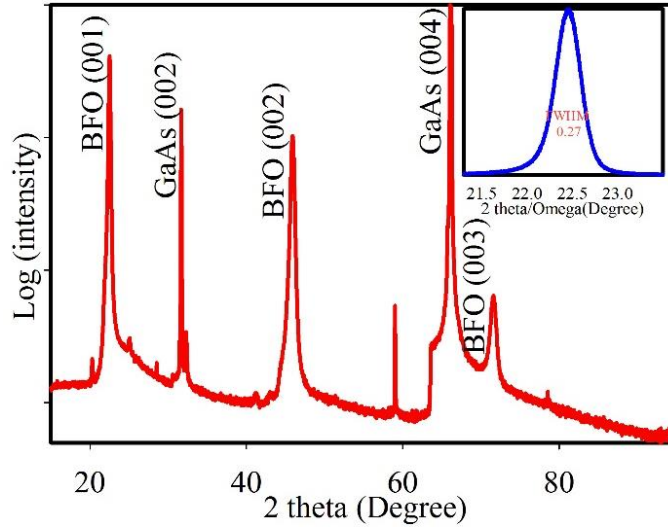


Figure 3.4: XRD pattern of BFO films grown on STO buffered GaAs. The inset shows the rocking curve for the BFO (001) peak.

X-ray photoelectron spectroscopy (XPS) studies were performed, in order to identify the chemical bonding in the BFO thin films. The film surface was contaminated by carbon as the film was exposed in air to transfer from PLD to XPS chamber. Figure 3.5 shows a XPS survey spectrum collected at room temperature for films deposited under the optimized growth conditions. XPS peaks and the corresponding Auger lines of Bi, Fe, O, and C are labeled in figure 3.5. Herein, C 1s peak located at 284.6 eV was used as the criterion to

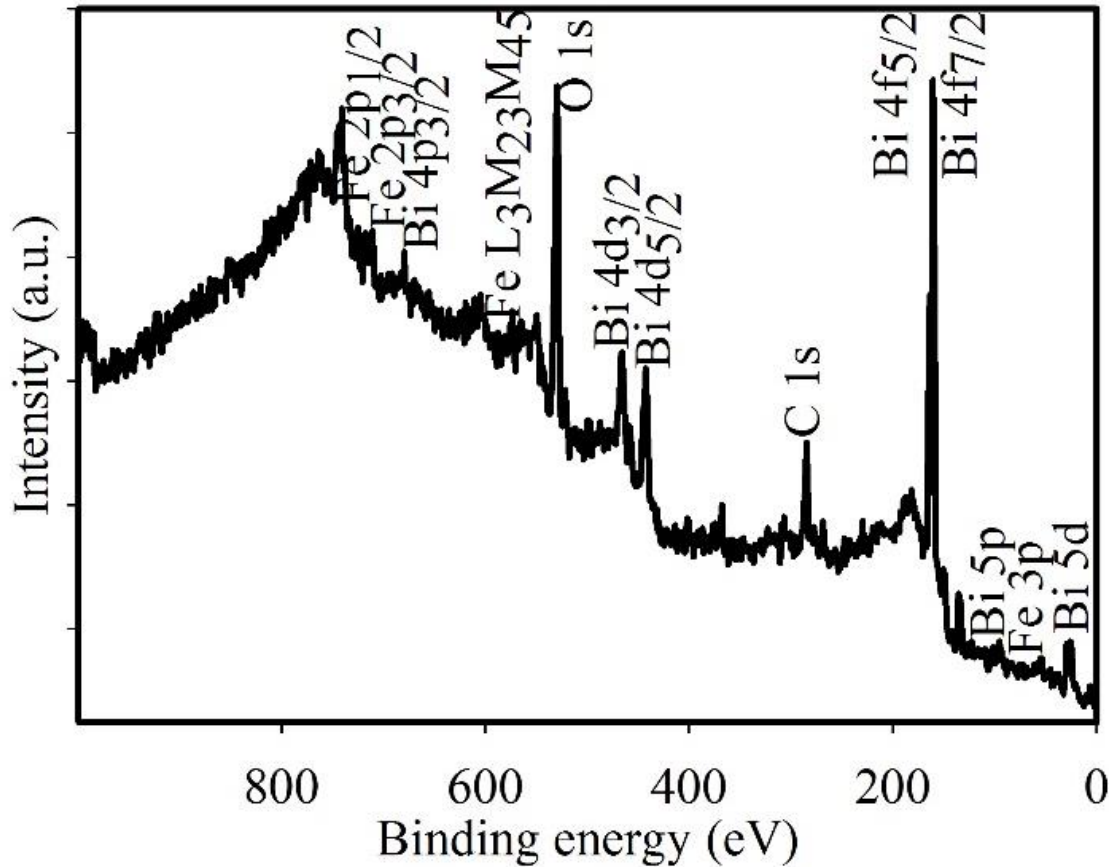


Figure 3.5: XPS survey spectrum performed on a BFO film.

further calibrate the peaks position. Characteristics peaks for Fe 2p_{1/2} (723.69 eV) and Fe 2p_{3/2} (710.33 eV), O 1s (529.7 eV), Bi 4f_{5/2} (163.90 eV) and Bi 4f_{7/2} (158.56 eV) were identified in the high-resolution spectra of Bi 4f, Fe 2p, and O 1s shown in figures 3.6, 3.7 and 3.8, respectively. Each peak of the Bi 4f doublet was fitted to a single Gaussian assigned to Bi-O bonds[118]. The experimental spin-orbit splitting energy ($\Delta_{\text{Bi } 4f}$) of Bi 4f level is 5.34 eV, consistent to the theoretical value of 5.31 eV. Figure 3.7 shows high

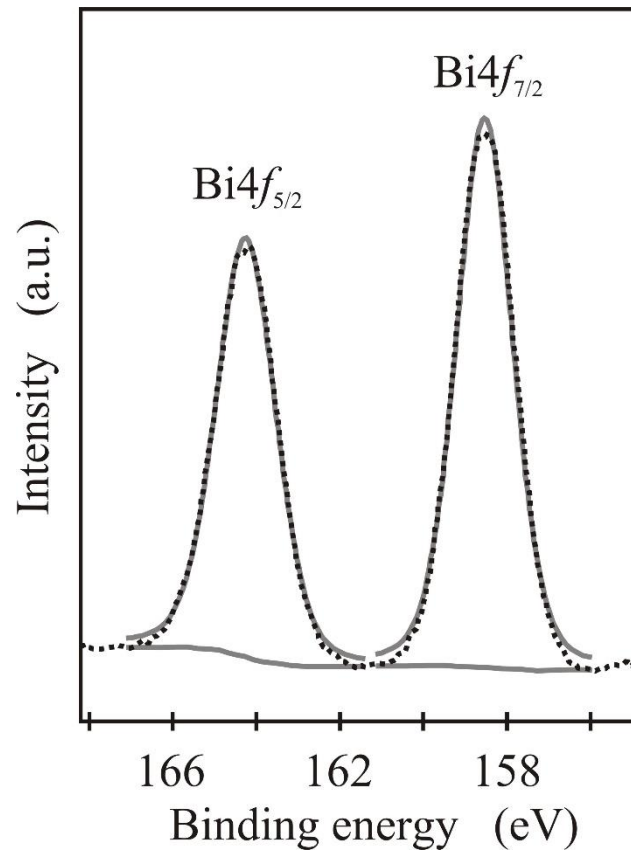


Figure 3.6: High resolution spectrum of Bi 4f core level of BFO films. Solid squares denote experimental data. Solid lines represent the fitting results after Shirley-type background subtraction.

resolution spectrum of Fe 2p doublet consisting of two wide peaks located at 710.33 eV (Fe2p_{3/2}) and 723.69 eV (Fe2p_{1/2}), which are mainly ascribed to Fe-O bonds[119]. Spin-orbit splitting energy of the pure Fe 2p doublet is equal to 13.36 eV, which is compared to theoretical value ($\Delta_{\text{Fe } 2p}$) of 13.6 eV for Fe₂O₃[119]–[122]. Two Gaussians on a Shirley-type background

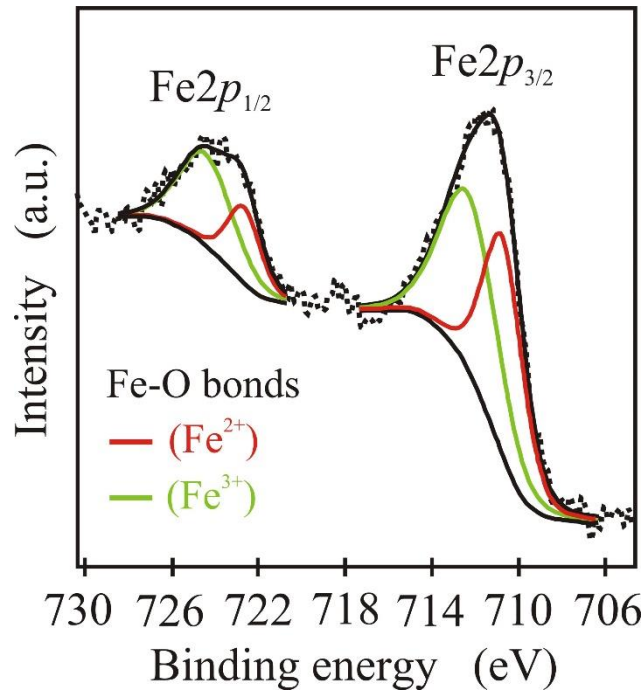


Figure 3.7: High resolution spectrum of Fe 2p core level of BFO films. Solid squares denote experimental data. Two Gaussians on a Shirley-type background were used to fit each peak of the doublet represented by solid colored lines.

were used to deconvolute each peak of the doublet. The components located at 712.51 and 724.75 eV are ascribed to Fe-O bonds for Fe³⁺, while the components located at 711.00 and 722.85 eV may be related to Fe-O bonds for Fe²⁺. The appearance of both the Fe²⁺ and Fe³⁺ state is typically connected with the existence of oxygen vacancy defects and degraded electric properties including increased leakage currents and formation of secondary phases which plays an important role in the magnetic and electric properties of the films[123]. The O 1s peak is a convolution of three peaks located at 529.61, 531.36 and 533.37 eV as shown in figure 3.8. The highest binding energy component (533.37 eV) can be attributed to

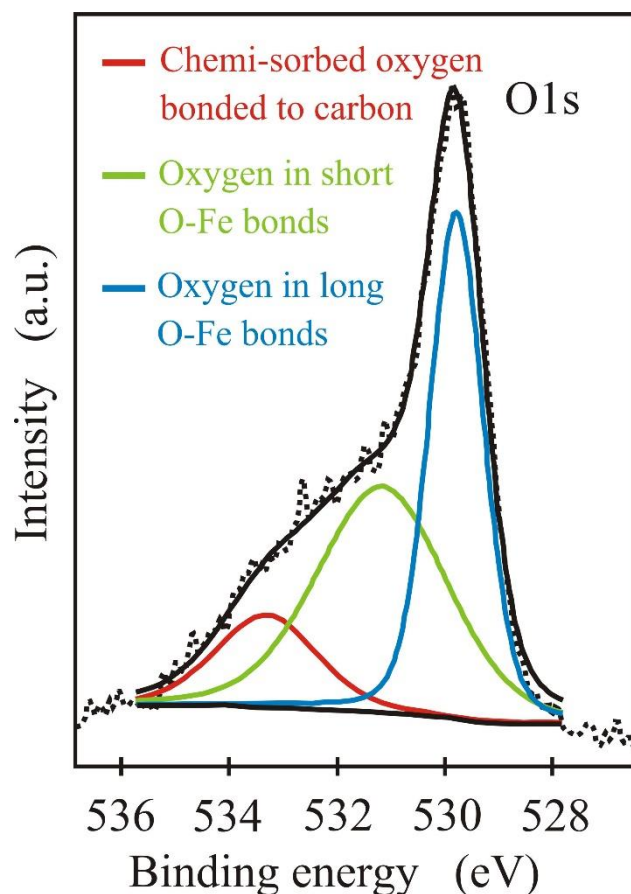


Figure 3.8: High resolution spectrum of O 1s core level of BFO films. Solid squares denote experimental data. The O 1s peak is a convolution of three peaks after Shirley-type background subtraction represented by solid colored lines.

oxygen bonded to carbon, C-OH, C-O-C, or the adsorbed oxygen linked to carbon on the surface of the film[121]. In this study, the other two components of O 1s in BFO that are observed near 530 eV are attributed to the two kinds of O-Fe bonds were created by the distortion of Fe-O bond in the unit cell. One was a long O-Fe bond and the other was a short bond which also have been confirmed by high-resolution neutron diffraction studies[121]. It is harder to emit the O 1s photoelectron from the tightly bonded O-Fe than it is to emit loosely bonded O-Fe, so O 1s photoelectrons from short O-Fe bond have low kinetic energy, and hence a higher binding energy at 531.36 eV. Similarly, the lower BE O 1s component at 529.61 eV originates from oxygen in long O-Fe bonds.

Atomic force microscopy in a piezoresponse force microscope (PFM) mode was employed to determine the surface morphologies and piezoelectric responses of the BFO thin films. PFM is a valuable tool for direct observation of nanoscale domains. Amplitude and phase information obtained in PFM analysis illustrate the ferroelectric polarization direction, strength, switching ability and domain structure of the ferroelectric order. In

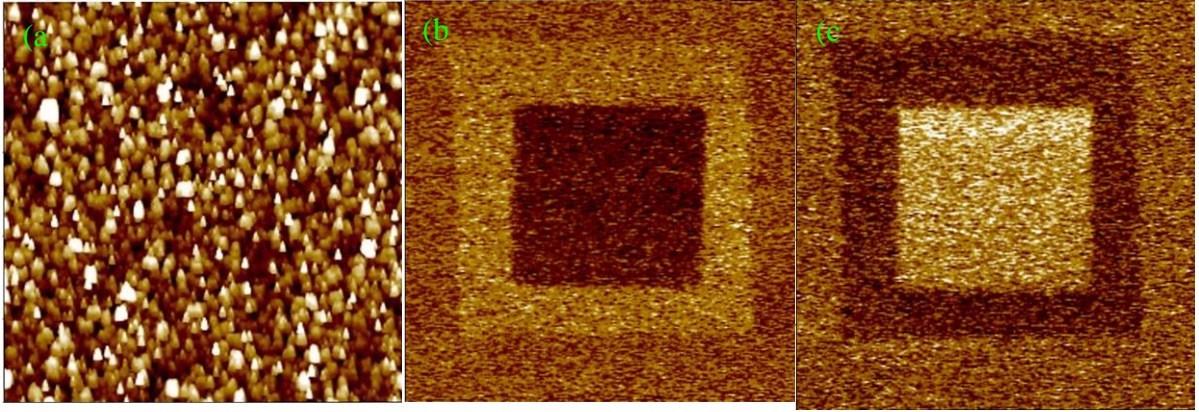


Figure 3.9: 12 x 12 μm^2 micrographs showing (a) topography, (b) PFM out-of-plane phase, and (c) out-of-plane amplitude of BFO thin film.

bulk, BFO ferroelectric behavior is realized by Bi ions displacement relative to the FeO_6 octahedra; therefore, the BFO films shows ferroelectric polarization along the body diagonals ($\langle 111 \rangle$). However, if the BFO crystal structure were tetragonal, the polarization direction would be expected to be along the ($\langle 001 \rangle$)[116], [124]. PFM measurements were carried out on the thin film grown under optimum conditions with a conducting platinum probe tip operated at a velocity of 1.80 $\mu\text{m}/\text{s}$ and a resonance frequency of around 24.5 kHz with locking bandwidth of 200 Hz. 12x12 μm^2 micrographs showing topography, PFM out-of-plane (OP) phase, and OP amplitude of BFO thin film are shown in figure 3.9. BFO surface morphology is flat and smooth without obvious cracks or discontinuities as

shown in figure 3.9 (a). The corresponding rms roughness is ~ 4 nm which suggests island growth instead of layer-by-layer growth mode[125].

PFM measurements were carried out in the following sequence: films were first poled by scanning over an $8 \times 8 \mu\text{m}^2$ area under a dc bias of -10 V applied to the tip; followed by a second $5 \times 5 \mu\text{m}^2$ scan with an applied bias of $+10$ V; a final $12 \times 12 \mu\text{m}^2$ scan was performed with no external bias. During the whole sequence the sample was kept grounded. Figures 3.9 (b) and 3.9 (c) show the OP PFM phase and amplitude images, respectively. Phase and

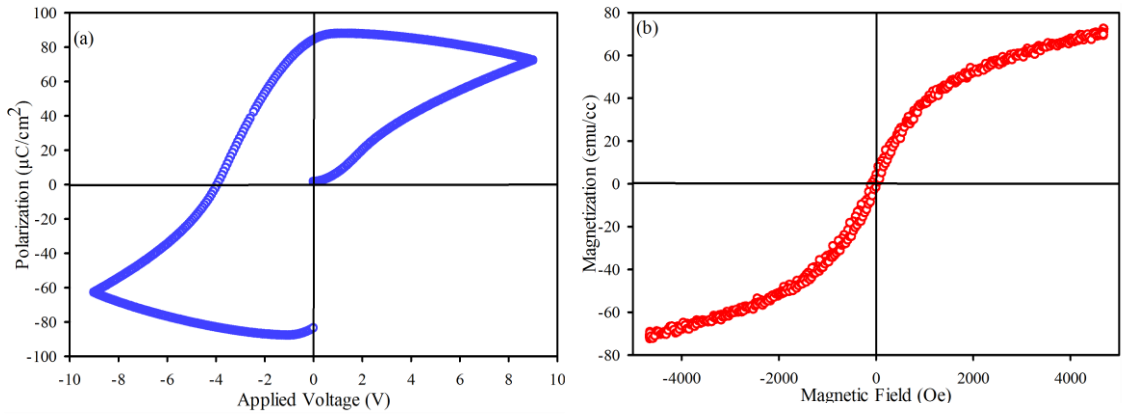


Figure 3.10: (a) Ferroelectric and (b) magnetic hysteresis loop measured at room temperature for the BiFeO_3 thin film.

amplitude images color contrasts clearly show domains orientations. In the positive and negative biasing regions, the domains are switching in opposite directions, while in the no biased region they are randomly oriented. The surface morphology of the films are highly dependent on the growth conditions, including deposition temperature and oxygen partial pressure[126]. These parameters were optimized for both surface morphology and electrical properties. While the growth of BFO on oxide substrate can result in films with improved surface morphology, the growth of BFO on III-V semiconductors has a substrate temperature limitation to avoid degradation of the semiconductor. Growth temperature of

used in this study was limited to 600°C with a post deposition annealing temperature of 500°C. Nevertheless, this low growth temperature appears to have a negligible effect on the oxidation the cations as evidence by the XPS investigation.

Using a ferroelectric tester, the polarization versus electric field (P-E) hysteresis loops of the BFO thin films were measured at room temperature by sweeping the voltage from -9 to +9 V at a frequency of 1 kHz. The polarization versus applied voltage showed a well-saturated hysteresis characteristic with a maximum polarization (P_{\max}) of $\sim 90 \mu\text{C}/\text{cm}^2$ (figure 3.10 (a)). The magnetic nature of the thin film was investigated by means of a VSM at room temperature with a maximum magnetic field of 5 kOe strength applied parallel to the film. Figure 3.10 (b) shows the magnetization as a function of the magnetic field. The diamagnetic background due to the GaAs/STO substrate has been subtracted from the data. It is observed that the magnetization increases following a closely linear relationship from -2 kOe to +2 kOe and thereafter, as expected tends to reach saturated state. This behavior suggests that the BFO thin film is antiferromagnetic (AFM) up to a field of 2 kOe[126], [127]. From the M-H dependence, the saturation magnetization M_s per unit volume was determined to be $72 \text{ emu}/\text{cm}^3$. Our films exhibit magnetization values comparable to the $150 \text{ emu}/\text{cm}^3$ for BFO (70 nm) thin film on STO substrate grown by PLD, and $180 \text{ emu}/\text{cm}^3$ for BFO (40 nm) thin film grown by MBE[28], [128]–[131], because the saturation magnetization (M_s) decreases with the BFO film thickness increases and is consistent with the G-type AF due to the spin spiral modulation of 62 nm that is reported in bulk BFO.

Spectroscopic ellipsometry (SE) technique was used to investigate the optical properties and thickness of BFO thin films by determining the ellipsometric parameters Ψ and Δ as a function of wavelengths (200-1000 nm) and incident angles (65° , 70° and 75°)

at room temperature, as shown in figure 3.11. The measured ellipsometric data were fitted to the corresponding optical model and by varying the parameters of the models in a step by step fitting procedure, the root mean square error (RMSE) was minimized. This is expressed as :[128]

$$MSE = \sqrt{\frac{1}{2N-M} \sum_{i=0}^N \left[\left(\frac{\psi_i^{mod} - \psi_i^{exp}}{\sigma_{\psi,i}} \right)^2 + \left(\frac{\Delta_i^{mod} - \Delta_i^{exp}}{\sigma_{\Delta,i}} \right)^2 \right]} = \sqrt{\frac{1}{2N-M} \chi^2} \dots\dots\dots 3.1$$

Here, N is the number of (Ψ , Δ) pairs, M is the number of free variables in the model and σ is the standard deviations, and ‘exp’ and ‘mod’ represent the experimental and the calculated data, respectively[128]. A six-medium optical model consisting of a semi-infinite GaAs substrate/amorphous gallium oxide/STO ultrathin buffer layer/BFO film/surface roughness/air ambient structure was considered to investigate the BFO thin film. The formation of amorphous Ga₂O₃ at the STO/GaAs interface is due to the fact that PLD growth process utilizes a higher oxygen pressure (>4 orders of magnitude than conventional MBE) during growth and the inter-diffusion of oxygen through the oxide films causes oxidation at the interface and converting some of the GaAs into Ga₂O₃. The BFO dielectric functions are described by four Tauc-Lorentz oscillator models whereas the surface roughness layer is modeled based on a Bruggeman effective medium approximation compared of a medium of 50% BFO and 50% voids. Our fitted/model generated ellipsometric parameters (Ψ and Δ) with very low RMSE value showing a good agreement with the measured data, as presented in figure 3.11; it also yielded a BFO film thickness of 216.23±0.05 nm and a roughness layer of 4.80±0.04 nm.

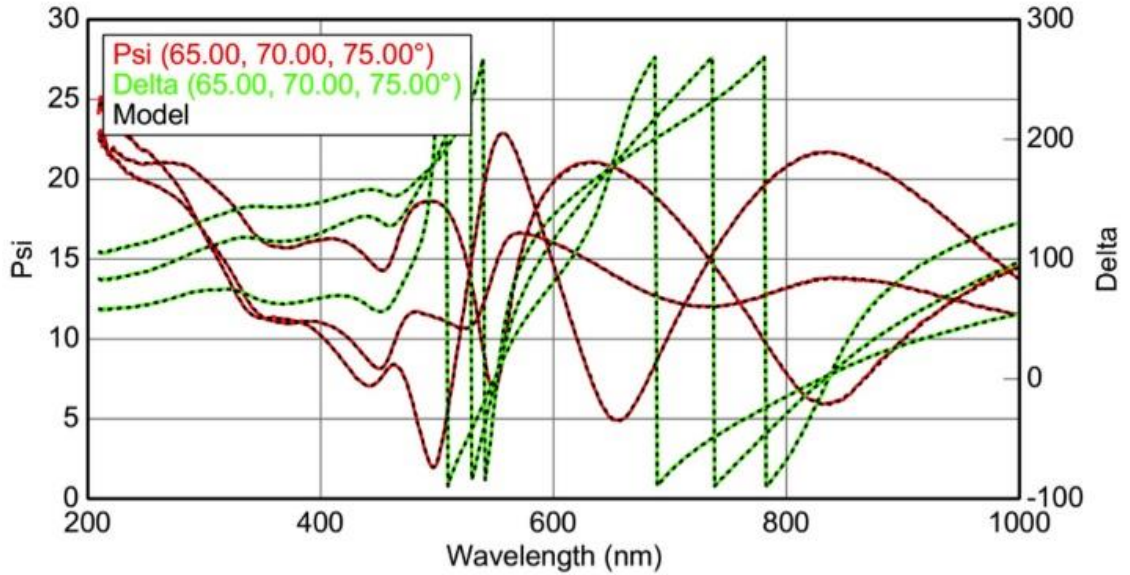


Figure 3.11: The measured and fitted ellipsometric spectra for the BFO film.

The film thickness and roughness is consistent with the thickness and root mean square roughness measurement from the profilometer, AFM and TEM.

Further analysis of the obtained optical constants (n & k) of the BFO thin film was performed were shown in figure 3.12 to derive a quantitative structure property relationship to better understand the effect of microstructure on the optical properties. For BFO, the absorption spectra followed the standard power law of the form

$$(\alpha h\nu)^2 = B(h\nu - E_g)^{1/2} \dots\dots\dots 3.2$$

where α is the absorption co-efficient and $h\nu$ is the photon energy. The bandgap (E_g) is obtained by extrapolating the linear portion of $(\alpha h\nu)^2=0$ at the absorption edge resulting in a direct gap of ~ 2.70 eV as shown in figure 3.12. It is known that the bandgap of BFO thin film is highly sensitive to the quality and strain in the heteroepitaxial structure[130]. The bandgap value of 2.70 eV obtained is in good agreement with other reported values

shows in Table I. The bandgap of BFO on DyScO₃ (DSO) is almost the same as that on SrRuO₃ (SRO) and is smaller than that on STO. It is noted that the in-plane (IP) pseudocubic lattice parameter for DSO and SRO is 3.946 and 3.923 Å [131], respectively, while STO has a cubic lattice parameter of 3.905 Å [132]. The compressive strain for the BFO thin film deposited on STO substrate is larger than that on SRO and DSO because the IP pseudocubic lattice parameter for BFO is 3.965 Å [133]. Thus, the more compressive strain imposed by the heteroepitaxial structure, the larger bandgap for the BFO thin film, which agrees with our result.

TABLE I. Bandgap of BFO thin film on different substrate prepared by PLD.

Bandgap (eV)	Substrate	Film Thickness (nm)
2.68	SRO buffered STO	99.19
2.67	DSO	100
2.70 (This work)	STO buffered GaAs	216

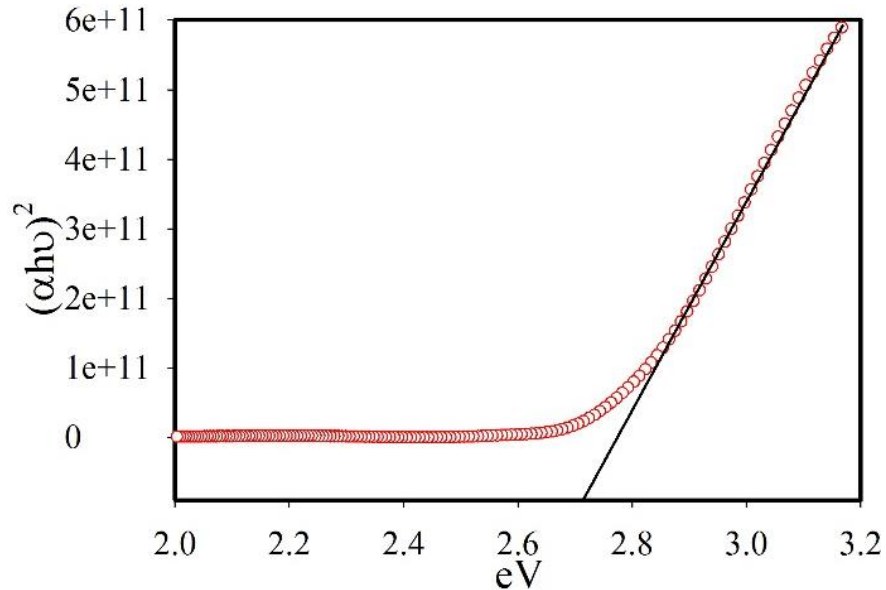


Figure 3.12: Plots of $(\alpha \cdot E)^2$ vs photon energy E for the BFO thin film. The linear extrapolation of $(\alpha \cdot E)^2$ to 0 gives band gap of 2.70 eV for the BFO film.

3.5 Conclusion

The details of the growth of epitaxial BFO films on STO buffered GaAs (001) by PLD were outlined. The optimized growth conditions are discussed in this chapter. Ferroelectric switching is clearly observed in our films with $P_{\max} \sim 90 \mu\text{C}/\text{cm}^2$. On the other hand, magnetic characterization showed that the films are anti-ferromagnetic with saturated magnetization of $72 \text{ emu}/\text{cm}^3$ and coercivity of about 120 Oe. The BFO film thickness and surface roughness were estimated as 216.23 and 4.80 nm, respectively. The optical constants of the BFO film were determined and through Tauc-Lorentz model analysis, a bandgap of 2.70 eV was obtained, which is in agreement with the bandgap values reported by various groups for BFO thin film grown by PLD. Our results demonstrated the feasibility for developing room temperature magnetoelectric coupling-based devices integrated onto III-V semiconductor. This might add an important component in the field of multifunctional devices with many applications. The optical results discussed here might also be useful in understanding the optical properties of the BFO thin film and its possible impact on identifying its applications in optoelectronics.

IV. BiFeO₃/La_{0.7}Sr_{0.3}MnO₃ HETEROSTRUCTURES WITH III-V SEMICONDUCTOR

4.1 Introduction

Multifunctional oxides from state-of-the-art thin film growth techniques has created new fundamental physical phenomena at different engineered interfaces due to the capability of artificially depositing atomically perfect and lattice-matched heterostructures[134]. The spin and charge degrees of freedom combined with the emergence of exciting properties at heterostructures is intriguing not only for the fundamental physics, but also due to their potential applications in future system-on-a-chip devices. Transition metals oxides, such as the manganites, cuprates and newly added multiferroics, provides an interesting playground to investigate the interactions of charge[135], spin[136], orbital[137] and lattice degrees of freedom at those hetero-interfaces, which ultimately could lead towards novel states of matter. Researchers are currently discovering a variety of fascinating physical phenomenon in combination with probable applications for devices which require small currents and magnetic field for operation such as sensors, magnetic memory and spintronics[137], [138]. Successively, these emerging properties could direct us to a pathway for lower power/energy devices with smaller feature sizes[4].

By utilizing the intrinsic magneto-electric coupling (MEC) coefficient, BFO offers an excellent way of controlling the electrical polarization using a magnetic field or vice versa[139]–[142]. However, the MEC coefficient in bulk BFO material is insignificant due to the small net magnetic moment in bulk BFO[143]. Surprisingly, the condition varies severely when BFO is deposited as epitaxial thin films where the FE polarization rises

considerably and MEC coupling becomes appreciable[143].

However, a different approach for stronger MEC coefficient could be achieved by using multiferroics (FE-AFM) and FM thin films in a bilayer structure where the AFM and FE ordering of the multiferroic coupled inherently with each other as well as coupled with the FM ordering extrinsically. The mechanism for coupling between AFM and FM is exchange bias or exchange anisotropy[140]. Significant exchange bias because of orbital reconstruction at the interface between multiferroic (FE-AFM) BFO and ferromagnetic LSMO makes them two perfect aspirants for this type of exchange bias based device applications. Control of FM spin alignment by an electric field when BFO is in close contact with a ferromagnet $\text{Co}_{0.9}\text{Fe}_{0.1}$ was shown by Chu et al.[144]. Exchange bias (H_{EB}) controlled by electric field from BFO/LSMO interface has been demonstrated by Wu et al.[140] and the interface magnetism between BFO/LSMO heteroepitaxially integrated on Si (100) was shown by Rao et al.[143]. Furthermore, exchange bias/exchange anisotropy has been utilized in multiple applications such as recording media, permanent magnets, and anisotropic magnetoresistance was used to stabilize the magnetization of soft ferromagnetic layer in recording heads[36], [134].

Another intriguing aspect of BFO/LSMO heterostructures based devices is related to the possibility of non-volatile memory (NVM) elements. This also known as the resistive random access memory (ReRAM) which obtained notable research attention for NVM devices beyond the 10 nm technology node because it could open new design topologies[145]. The progress of ReRAM depends on the appropriate choice of materials such as organics, solid electrolytes, oxides, ferroelectrics and multiferroics[145]–[148]. However, ReRAMs based on solid electrolytes typically depends on chemical processes or

destructive electroforming process and could lead to physical damage to the device due to heat formation during the chemical reaction[149]. On the other hand, simple ferroelectric ReRAM are limited by the need for a destructive read and reset operation[7]. Resistive switching behavior in BFO/LSMO heterostructure has attracted considerable attention because the ferromagnetically coupled ferroelectric domain walls (DWs) are more conductive in BFO than a simple ferroelectric material, thus facilitating longer life time and faster operation. And it opens a possibility for combining spintronics and ferroelectricity which offers additional degrees of freedom for BFO/LSMO based multifunctional devices[150].

These breakthrough investigations on BFO/LSMO heterostructure for exchange bias and NVM devices will be attractive for the next generation memory devices which allow for writing electrically and reading magnetically. These heterostructures have solely been deposited on substrates which are perfectly lattice matched with the grown films such as DyScO₃ (DSO), NdGaO₃ (NGO), SrTiO₃ (STO) and Nb doped STO (NSTO). Unfortunately, these insulating substrates are not compatible with the existing complementary metal-oxide-semiconductor (CMOS) based technological applications. In this chapter, the potential of BFO/LSMO heterostructures deposited on STO buffered GaAs (001) for NVM and field effect device applications will be evaluated.

4.2 Experimental

4.2.1 Thin Film Deposition and Device Fabrication

In this chapter, BFO/LSMO/STO/GaAs (001) heterostructures were successfully grown and optimized the growth conditions for different layers. This work was facilitated by the deposition of an epitaxial 5 nm STO (001) buffer layer on GaAs (001) by molecular

beam epitaxy (MBE). For the crystalline oxide growth on semiconductor, MBE is an ideal deposition technique for nucleation because during the growth MBE can control the exposure of the semiconductor surface to oxygen[112]. The LSMO (001) and BFO (001) bilayer were deposited by pulsed laser deposition (PLD) using KrF excimer laser ($\lambda=248$ nm) on STO buffered GaAs (001) substrate. The focused laser beam irradiates the circular stoichiometric targets with a laser energy density of ~ 2.5 J/cm² at a repetition rate of 10 Hz in an oxygen ambiance of 100 mTorr and the temperature was maintained at 600°C during the deposition process. The samples were annealed at 500 °C for 30 min under the same O₂ pressure during the growth and cooled down slowly under partial O₂ pressure after the annealing. The PLD system consists of a multi-target assembly for up to six targets which are rotated during growth and can be indexed to the target of interest in line with the laser beam. During growth, the substrate and target are rotated continuously to provide uniform growth and ablation.

For multiferroic field effect device high quality 10 x 10 mm² STO (5 nm) buffered GaAs substrate were used. The device structure was then patterned by depositing BFO (100 nm) /LSMO (3 nm-20 nm) heterostructures using two different shadow mask. The first shadow mask is to deposit the LSMO channel layer and the second shadow mask is to deposit the BFO as gate dielectric. Finally, gate and channel electrodes (2 nm Ti layer and a 100 nm Au layer) were deposited using contact photolithography followed by a lift-off process.

4.2.2 Characterizations

To investigate the crystalline structure of deposited heterostructure, XRD pattern was recorded using a Rigaku SmartLab X-ray diffractometer (Cu K α radiation) at an operating voltage of 40 kV and a current of 44 mA. Topographical, morphological and

compositional studies were performed using a high-resolution transmission electron microscope (HRTEM, JEOL 2010F) with a point-to-point resolution of 1.8 Å and operated at 200 KV. The epitaxial relationships and quality of the interfaces were determined by HRTEM images from cross sections of the sample. Focused ion beam (FIB) technique was employed for TEM sample preparation. SPECS-made XPS spectrometer with monochromatic Al/Mg anode source was used for the surface elemental analysis and to identify the Fe valence state. To determine binding energy, characteristic kinetic energy of the emitted electrons was collected with a pass energy of 50 eV and C 1s peak located at 284.6 eV is used as the criterion to further calibrate the peaks position. To measure the surface morphology and ferroelectric characteristics at room temperature, piezoresponse force microscopy (PFM) measurements were carried using a scanning probe microscope (Park XE7). In order to investigate the polarization switching behavior of BFO, a dc bias of 0 and ± 10 V was applied on BFO films using a conducting platinum probe tip operated at a velocity of 1.80 $\mu\text{m/s}$ and a resonance frequency of around 24.5 kHz with locking bandwidth of 200 Hz. Ferroelectric P-V measurement was performed using Precision II (Radiant Technologies, Albuquerque, NM). The temperature and magnetic-field dependent magnetization measurements were carried out by utilizing the vibrating sample magnetometer (VSM) module of Quantum Design Physical Properties Measurement System (PPMS). It should be noted that diamagnetic background due to GaAs/STO substrate has been subtracted from all the data that are presented in this work. From different heterostructures, sample size of ~ 4 mm X 4 mm was used for magnetization hysteresis (M-H) measurement. The magnetic field paths were varied from 0 \rightarrow 2000 \rightarrow 0 \rightarrow -2000 \rightarrow 0 \rightarrow 2000 Oe in zero field cooled, positive and negative field cooled M-H

measurements when the magnetic field was kept parallel to the film plane for all the samples reported here. Semiconductor parameter analyzer were utilized to conduct the electric properties measurement at room temperature.

4.3 Results and Discussions

The crystal structure of BFO/LSMO heterostructures grown by PLD on 5 nm STO buffered GaAs (001) were characterized by X-ray diffraction (XRD) as shown in figure 4.1. From the θ - 2θ scan, it can be seen that only (001) and (002) peaks of the BFO, LSMO and GaAs are present, indicating that both the BFO and LSMO are c-axis oriented with respect to normal to the substrate[151]. No STO peaks were observed in the scan because of the overlap with the peaks of BFO and LSMO films and lower intensity of the STO peaks due to a thickness of only 5 nm. High quality films formation was further confirmed because there were no appearance of secondary/impurity peaks in the XRD spectra.

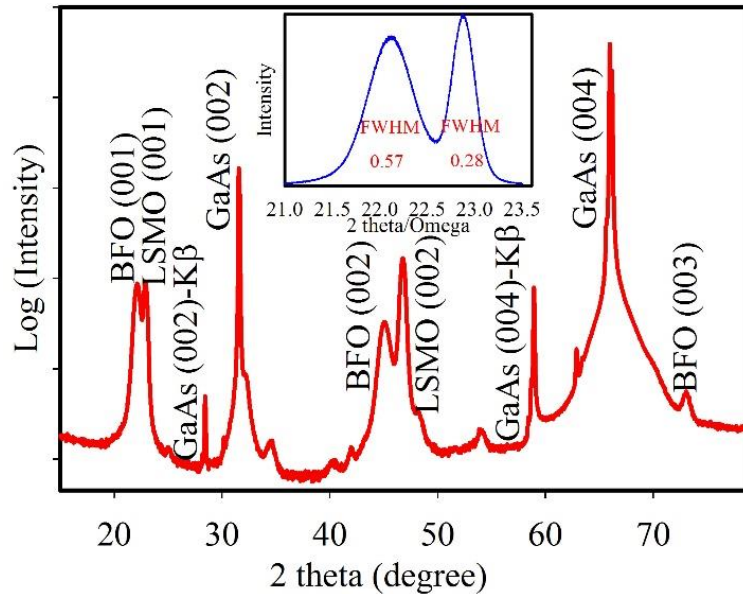


Figure 4.1: Shows the typical θ - 2θ XRD pattern BFO/LSMO/5 nm STO/GaAs sample which indicating high quality, single phase (001) oriented oxide films. X-ray $k\beta$ emissions are also identified. The inset of figure 4.1 shows the rocking curve of the BFO-LSMO (001) peak. The rocking curve shows FWHM of 0.57°C for BFO (001) and 0.28°C for LSMO (001) diffraction peak.

Inset of figure 4.1 shows the rocking curve of BFO-LSMO (001) peak, where the full width at half-maximum (FWHM) is about 0.57°C and 0.28°C respectively, comparable to the best BFO and LSMO films deposited on STO substrates[143], [152].

To elucidate the structure, chemistry, and quality of interfaces, high-resolution transmission electron microscopy (HRTEM) were employed. Figure 4.2 (a) is a typical bright-field cross-section transmission electron microscopy (TEM) image of BFO/LSMO/STO/GaAs heterostructure. The thickness of BFO and LSMO are estimated to be ~ 10 and 90 nm, respectively. Figure 4.2 (b, c and d) shows typical HRTEM images taken at the LSMO/STO/Ga₂O₃/GaAs, BFO/LSMO and LSMO/STO/Ga₂O₃ interfaces, respectively. The inset of figure 4.2 (d) shows the elemental compositions measured by EDS. While most of the interfaces are sharp and clean, there is a layer of ~ 10 nm amorphous Ga₂O₃ formation at the STO/GaAs interface. Prior studies of the STO/GaAs interface reveal a sharp crystalline transition after the growth of STO using MBE. Since the PLD growth process utilizes a higher oxygen pressure ($\sim >4$ orders of magnitude) during growth, the inter-diffusion of oxygen through the oxide films caused oxidation of the Ga and converting some of the GaAs into Ga₂O₃.

Figure 4.3 (a) shows the PFM topographical image of a $12 \times 12 \mu\text{m}^2$ scan region of BFO thin film deposited on LSMO/STO/GaAs heterostructure. BFO surface morphology is flat and smooth without obvious cracks or discontinuities and a scanning electron microscopic (SEM) image shows a uniform surface of the sample. To realize the polarization switching ability, PFM measurements were carried out in the following

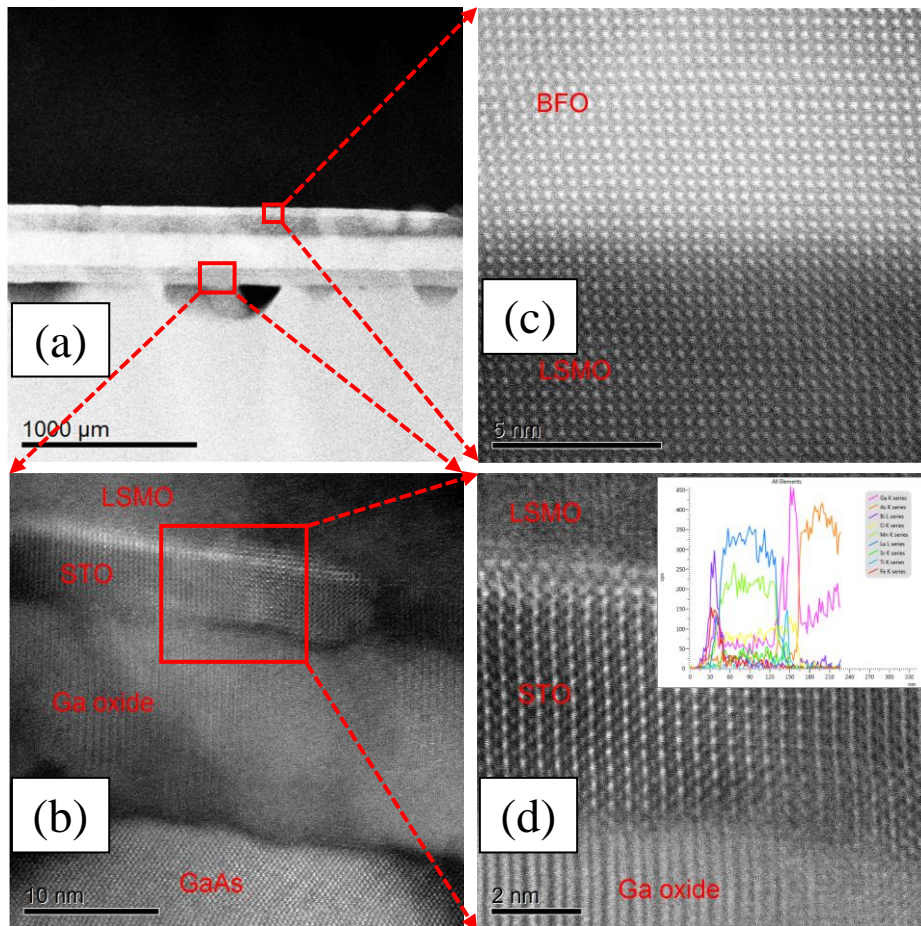


Figure 4.2: (a) Bright field cross-section TEM image of BFO/LSMO/STO/GaAs heterostructure. (b) HRTEM image of LSMO/STO/Ga₂O₃/GaAs interface. (c) HRTEM image of BFO (10 nm)/LSMO (90 nm) interface and (d) shows the HRTEM of LSMO/STO/Ga₂O₃ interface.

sequence: films were first poled by scanning over an 8x8 μm² area under a dc bias of -10 V applied to the tip; followed by a second 5x5 μm² scan with an applied bias of +10 V; a final 12x12 μm² scan was performed with no external bias. During the whole sequence sample was kept grounded. Figures 4.3 (b) and 4.3 (c) show the PFM phase and amplitude images, respectively. The changes in color contrasts present for both negative and positive poled regions represent the direct indication of polarization switching behavior in BFO.

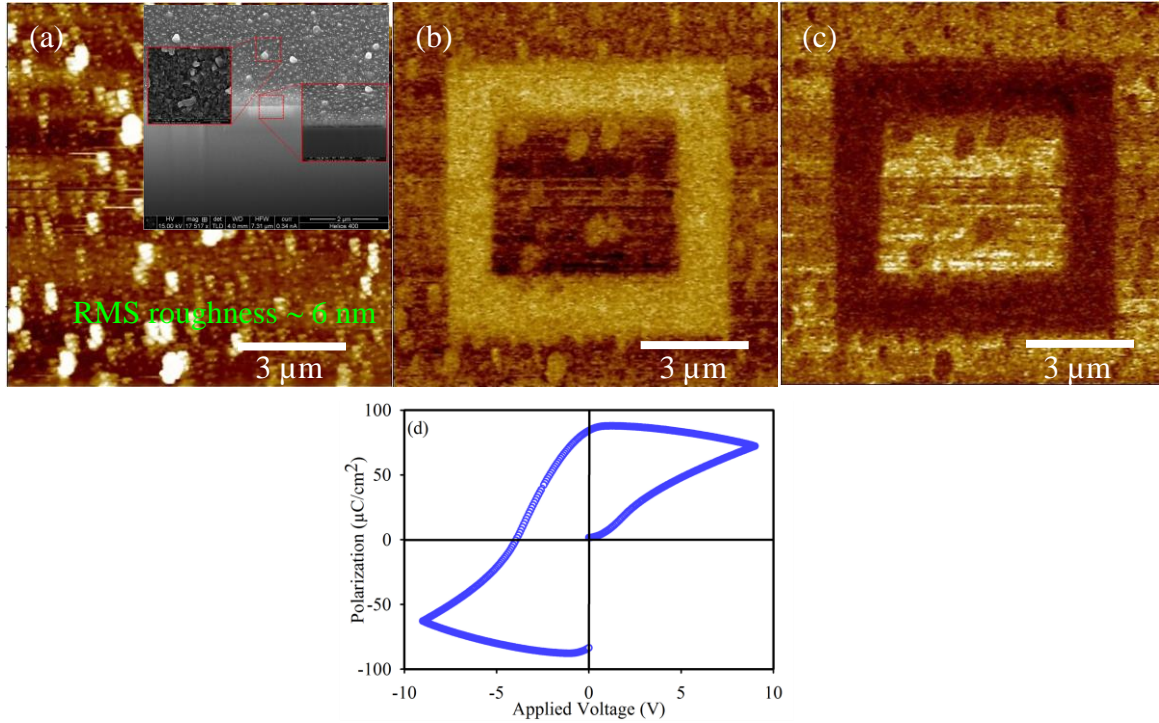


Figure 4.3: Ferroelectric domain switching observation of BFO/LSMO/STO/GaAs heterostructure. (a) Surface topography and inset shows SEM image of uniform sample surface, (b) PFM phase and (c) amplitude after poling with ± 10 V. (d) Room-temperature polarization-voltage hysteresis loops using top electrode from electrical measurements. Our film offers low coercive voltage and high remnant polarization, which are indispensable for low-power and high density non-volatile memory applications.

The achievement of polarization switching in multiferroic thin films is particularly significant in order to realize its capability for rewriting and changing states in NVM devices [145], [153]. The polarization-voltage (P-V) hysteresis loop for BFO/LSMO bilayer thin films shown in figure 4.3(d), depicts a square hysteresis loop for BFO/LSMO heterostructure. The well-saturated hysteresis characteristics with a maximum polarization (P_{\max}) of $\sim 90 \mu\text{C}/\text{cm}^2$ was found but the coercive voltage was found only 4.0 V. The P-V measurement indicates low leakage current in BFO films which considered an essential criterion for realizing high retention in NVM devices. Thus, PFM outcomes shown in figure 4.3 ensures that BFO will provide expected read/write operation since a full

polarization switching was observed in an iterative process and the ferroelectric domains are not pinned in the devices.

The magnetic properties of BFO/LSMO/STO/GaAs heterostructures were examined with variation of temperature and magnetic field. Zero field cooling (ZFC) and field cooling (FC) magnetization versus temperature (M-T) curves of heterostructures were displayed in figure 4.4. During the magnetic measurement, field kept parallel along the samples and information were recorded in the heating cycle while maintaining a constant field of 300 Oe. The reported Curie temperature (T_C) \sim 350 K for our heterostructures was not observed since our PPMS (VSM) measurement is limited to 310 K only[143], [154]. However, a blocking temperature of \sim 63 K was obtained at which ZFC and FC curves split. Magnetization versus field (M-H) hysteresis curves of the heterostructures were measured subsequently by cooling the samples in a magnetic field of ± 2000 Oe, kept parallel to film plane. At low temperatures, the BFO/LSMO heterostructure exhibits, a

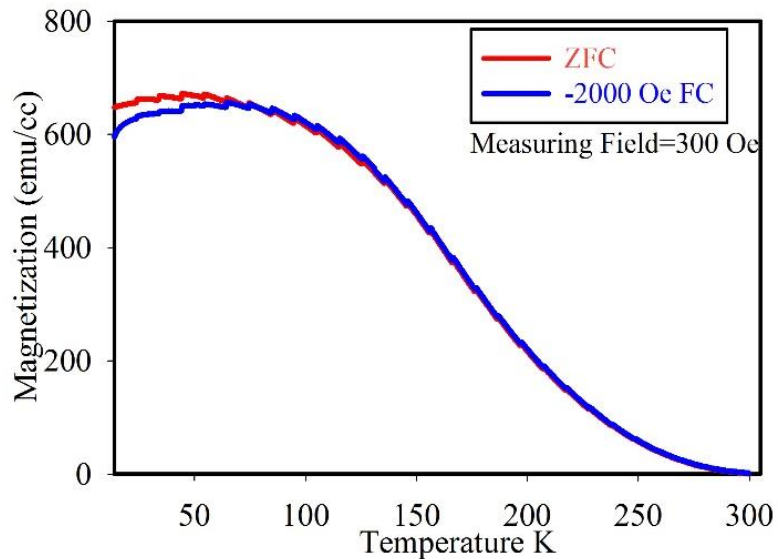


Figure 4.4: M-T curves of BFO/LSMO/STO/GaAs heterostructure. The samples were cooled under -2000 Oe field and data were collected during the warming cycle under the measuring field of 300 Oe.

large enhancement in magnetic moment and coercive field, a shift of the hysteresis loop (exchange bias) and magnetic hysteresis loop squareness also observed. The M-H loop shifted towards reverse direction of the cooling field, as expected from conventional exchange bias behavior, and suggests ferromagnetic alignment between the pinned, uncompensated spins in the antiferromagnet and the spins of the ferromagnet[36], [44], [134]. These results were very consistent over many heterostructures with LSMO thickness varies in the range of 3-18 nm and demonstrated exchange bias behavior as presented in figure 4.5. The amount of M-H loop shift due to exchange bias effect at the interface thoroughly decreased with LSMO thickness which is logical for typical exchange bias originating from the AFM-FM interface[36], [140], [155]. To verify that this magnetic hysteresis loop shift is solely from AFM-FM interface, a different heterostructure by replacing BFO layer with the same thickness of $\text{Pb}_{1.1}\text{Zr}_{0.53}\text{Ti}_{0.47}\text{O}_3$ (PZT) was measured and the M-H curve of this sample indicates no noticeable shift after being field cooled. Though exchange bias interactions were realized within BFO/LSMO interface but it was not observed in a single LSMO layer or PZT/LSMO heterostructure. Actually, exchange bias shifts are only exists in interface within ferromagnetic LSMO together with the ferroelectric-antiferromagnetic BFO and not with the ferroelectric PZT indicates to the fundamental role that the antiferromagnetic properties of the BFO play in controlling the behavior of such heterostructures. Moreover, a thorough investigation of the enhancement of coercive field (H_C) due to the variation of temperature and the exchange bias shifts (H_{EB}) with LSMO thickness in the BFO/LSMO heterostructures are given in figure 4.5 (c) and 4.5 (d) respectively, offers supplementary perception into the fundamental physics and emergence of coupling effects in these heterostructures. To quantify the exchange bias, the

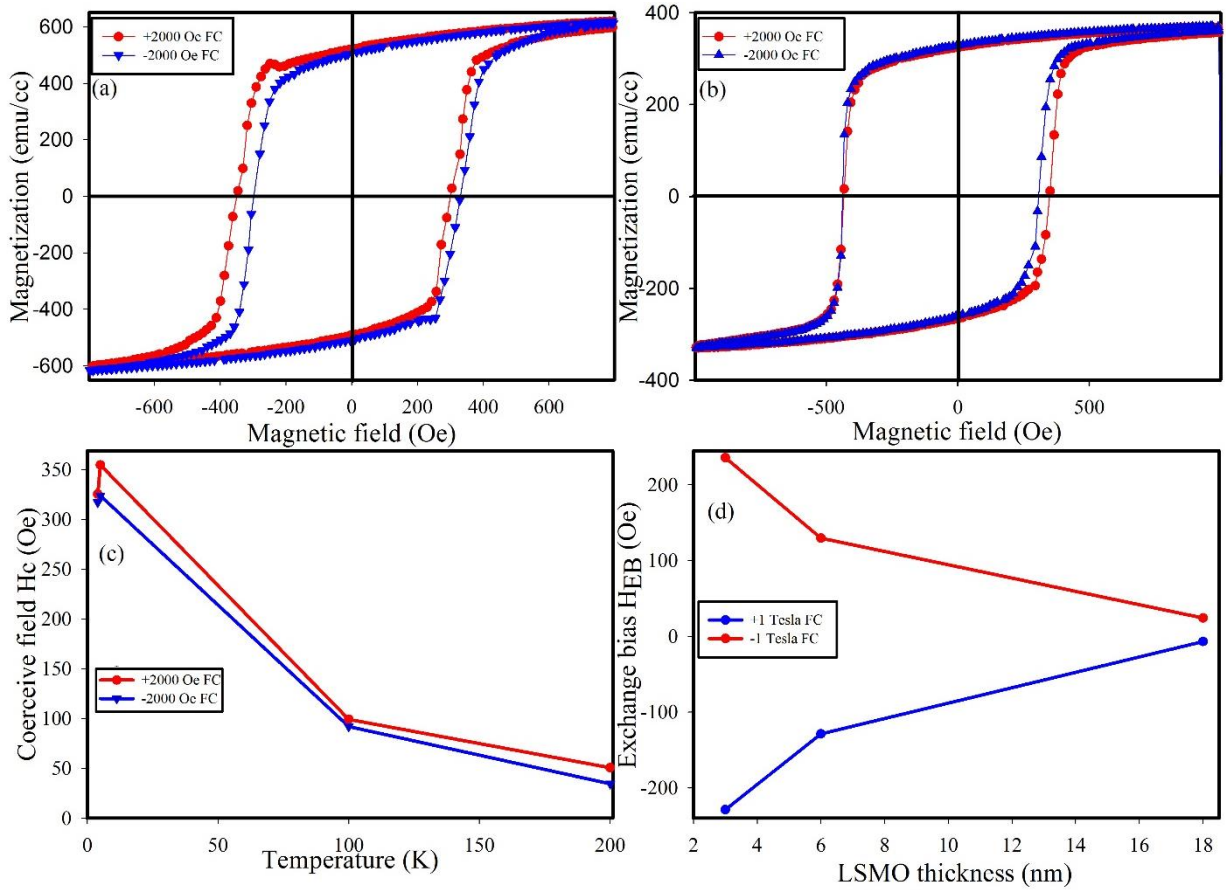


Figure 4.5: (a) Magnetic hysteresis curves measured on BFO/LSMO/STO/GaAs heterostructure after cooling the sample under ± 2000 Oe at 4K. Also, there is a shift in FC, M-H loop. (b) Magnetic hysteresis curves measured on PZT/LSMO/STO/GaAs heterostructure after cooling the sample under ± 2000 Oe fields. The magnetic moment practically remains the same, inferring the strong contribution of interface effect of BFO on LSMO. No significant FC, M-H loop shift and no change in magnetic moment are observed from PZT/LSMO interface. (c, d) Temperature dependence of the coercive field H_c enhancements and LSMO thickness dependence of exchange bias shifts H_{EB} measured at 5K.

exchange bias field (H_{EB}) and coercive field (H_c) was identified as $(H_{C1}+H_{C2})/2$ and $(H_{C1}-H_{C2})/2$ respectively, where H_{C1} and H_{C2} denotes the positive and negative coercive field[36], [156]. After a certain high temperature, magnetic properties are only dependent on the LSMO thin layer and there is no observable difference in the magnetic properties of other heterostructures. The thickness of the ferromagnetic layer and exchange bias field are

inversely proportional to each other. For single LSMO thin film with a thickness less than 5 nm exhibits a narrow coercive field with a transition temperature above room temperature but the coercive field as well as the transition temperature alters significantly if the LSMO thickness reduced below 5 nm[134]. This is usually explained by taking into account a strain-induced movement of MnO_6 octahedra according to the Jahn-Teller distortion theory[134], [157]. A bulk-like transport/magnetic properties has revealed by ultrathin LSMO films down to a thickness of 5 nm due to the progressive change of metallic behavior towards semiconducting (32 Å) and vanishing the ferromagnetism property (12 Å), reported recently[158].

It is essential to mention that, exchange bias effect in BFO/LSMO interface is significantly different from prior studied other metallic ferromagnets in contact with BFO[30], [159]. For example, hetrostructures of conventional ferromagnets (CoFe) which are exchange coupled with BFO shows tremendous capability to tune their exchange interaction by changing the domain structure of the BFO film only. Prior studies have shown the capability to make the so-called stripe-like (71° domain walls) and mosaic-like (109° domain walls) BFO films by regulating the growth rate of the BFO layer and a direct relationship between the amount of the exchange bias shifts and the density of certain types of domain walls was observed[159]. The BFO domain structure dependency of exchange coupling effect is not detected in BFO/LSMO heterostructures. Heterostructures other than BFO/LSMO, exchange bias shifts are also noticed irrespective of the BFO domain structure at temperature less than 120 K. However, the appearance of exchange bias at this low temperature is another essential inequality among BFO/LSMO and the formerly studied BFO/ $\text{Co}_{0.9}\text{Fe}_{0.1}$ heterostructures which indicates to a basic discrepancy in the nature of

exchange bias coupling. There is no obvious difference in the magnitude of exchange bias of BFO/Co_{0.9}Fe_{0.1} heterostructures during temperature dependence studies from 300 to 5 K were realized irrespective of the underlying BFO domain structure. This alteration can be attributed to the existence of a native ferromagnetic state within BFO/LSMO interface as well as a transition of antiferrodistortive phase[139], [160].

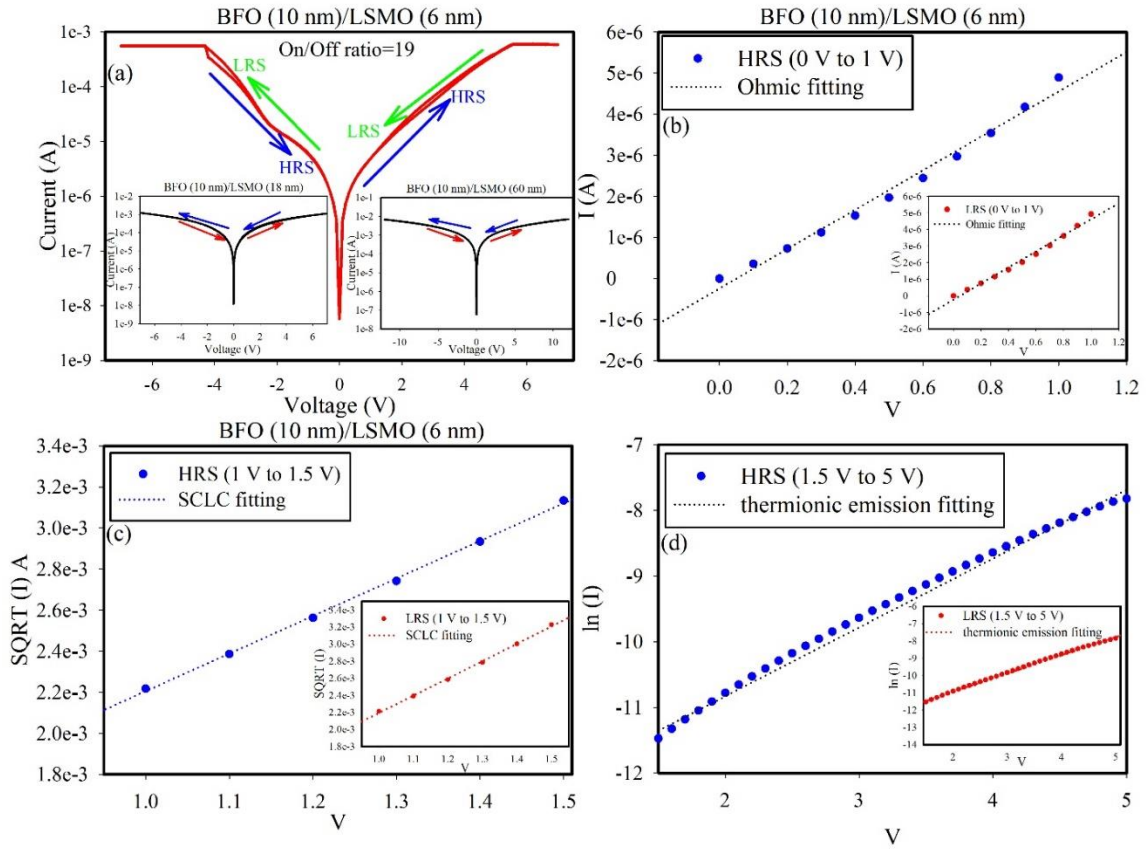


Figure 4.6: (a) Current-voltage switching characteristics for 10 nm BFO deposited on 6 nm, 18 nm and 60 nm of LSMO. Carrier injection mechanisms for resistive switching by fitting both the HRS and LRS I-V curves revealed (b) Ohmic type conduction ($I \propto V$), (c) space charge limited conduction ($I \propto V^\alpha$ where $\alpha \geq 2$) and (d) thermionic emission ($\ln I \propto V$).

Resistive switching behavior of Au/Ti/BFO/LSMO/STO/GaAs based memory devices at room temperature is shown in figure 4.6 (a). Figure 4.6 (a) shows the I-V characteristics of the BFO (10 nm)/LSMO (6 nm), BFO (10 nm)/LSMO (18 nm) and BFO

(10 nm)/LSMO (60 nm) heterostructures on GaAs respectively. No switching hysteresis is observed for the BFO (10 nm)/LSMO (18 nm) and BFO (10 nm)/LSMO (60 nm) heterostructures. Only BFO (10 nm)/LSMO (6 nm) heterostructure shows the clear opening of hysteresis with a shift in the current, which confirms the resistive switching behavior. The applied potential was altered from $0 \rightarrow 7$ V, $7 \rightarrow 0$ V, $0 \rightarrow -7$ V and $-7 \rightarrow 0$ V, were known as high resistive state (HRS), low resistive state (LRS), LRS, and HRS respectively. Current-voltage (I-V) hysteresis curve was obtained in the BFO/LSMO heterostructure devices integrated with GaAs. Originally, the device remained in the virgin state or in HRS prior to any external bias and it was still in HRS when the external bias on the device varied from $0 \rightarrow 7$ V. It was found that the current suddenly increased at 4.0 V when the voltage was driven back from $7 \rightarrow 0$ V and this increment in current can be stated as LRS and the 4.0 V is denoted as a set voltage. The device will have retained this LRS during the whole voltage cycle from $7 \rightarrow 0$ V and $0 \rightarrow -7$ V. The device can be switched from LRS to HRS at -4 V when the voltage was varied from $-7 \rightarrow 0$ V. The device remained at the HRS state during the whole voltage cycle from $-4 \rightarrow 7$ V, and the -4 V can be denoted as a reset voltage. The device can be switched from HRS to LRS again when further 4 V was applied during the voltage cycle from $7 \rightarrow 0$ V. The measured set/reset voltage was obtained at ± 4 V, which is considerably lower when weighed with different ferroelectric or oxides based NVM devices where ~ 5 V was required as a set/reset voltage[146], [161]–[163].

The measured low set/reset voltage could direct us towards NVM devices which requires low-power consumption. Our devices are safe from the development of conductive bridge filaments or other electroforming process because large current and voltage are required for such a destructive process. Hence, our devices are free from thermal damage

and thus enhances the reliability of the NVM devices[145], [149]. To examine the comprehensive behavior of resistive switching, these I-V characteristics fitted to various possible carrier injection mechanism such as Ohmic conduction ($I \propto V$), thermionic emission ($\ln I \propto V$), space charge limited current ($I \propto V^\alpha$ where $\alpha \geq 2$), Poole-Frenkel emission ($\ln(I/V) \propto V^{1/2}$), and Fowler-Nordheim tunnelling ($I \propto V^2 \exp(-E_a/V)$), where E_a is the kinetic energy of the charge carriers[164]. Figure 4.6 (b-d) shows the conduction mechanisms by fitting both the HRS and LRS I-V curves. The Ohmic conduction was responsible for current transport when the voltage varied from $0 \rightarrow 1$ V for both the HRS and LRS shown in figure 4.6 (b). However, figure 4.6 (c) shows the space charge limited conduction (SCLC) liability when the voltage was varied from $1 \rightarrow 1.5$ V. And finally, both the thermionic (TE) and thermionic field emission (TFE) were accountable when voltage varied from $1.5 \rightarrow 5$ V shown in figure 4.6 (d).

Moreover, transistor type action for BFO/LSMO heterostructure based devices was demonstrated using simple ferroelectric field-effect transistor (FeFET) structures. P-type LSMO channel layer and BFO multiferroic as a gate dielectric were grown on STO buffered GaAs by PLD using two different shadow mask. Figure 4.7 (a) shows a cross-sectional schematic illustration of the BFO/LSMO based FeFET. The gate length, source-drain spacing, and the length of the source/drain electrode were 1, 5, and 1.2 μm respectively. Figure 4.8 (a) and (b) shows the DC output I-V and transfer characteristics respectively for BFO/LSMO heterostructure based FeFET. The drain current (I_d) was efficiently controlled

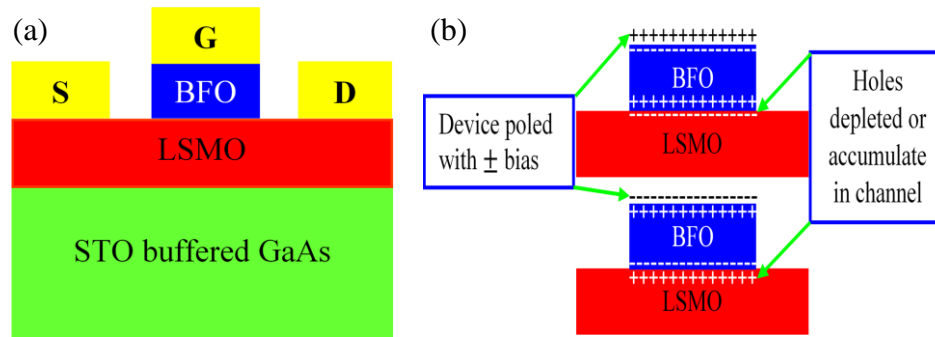


Figure 4.7: (a) Cross-sectional schematic illustration of the device. (b) Schematic diagram of a simplified model for the field effect in a p-type ferroelectric FET.

by gate voltage (V_g) with a sharp pinch-off characteristic. The device demonstrated a maximum I_d of 31.74 mA at a drain voltage (V_d) of 7 V and a V_g of ± 5 V. The drain leakage current (I_{off}) during off state was as small as 1.67 mA, resulting in a high on/off ratio of about ~ 19 . The I_{off} was analogous to the gate leakage current, specifying that leakage through the multiferroic BFO film was negligible. Additionally, most of gate leakage current may possibly have ascribed to the large electrode pad, and the ideal leakage

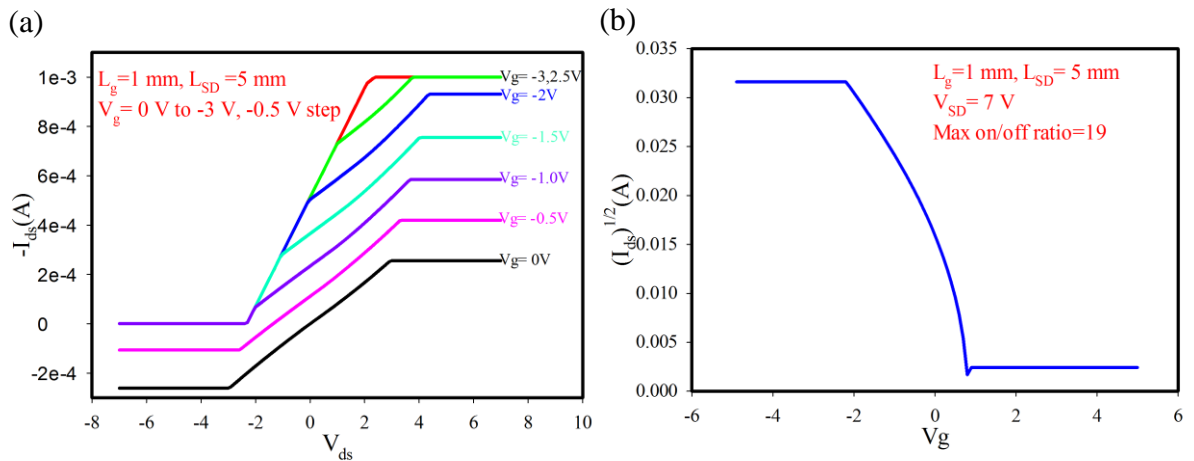


Figure 4.8: (a) DC output I-V curves. (b) Transfer characteristics of the device.

through the gate multiferroic could be decrease by at least one order of magnitude. Thus, the I_{off} can be successfully repressed simply by adjusting the device architecture. In order

to prove that the channel modulation realized in figure 4.8 can possibly be ascribed due to a field effect, the following argument can be taken into account. Since the channel material LSMO is p-type then holes are the majority carriers in the channel. Now, if a positive voltage is applied to the gate multiferroic then the electric dipole moments will point downward into the channel. This arrangement will efficiently support the accumulation of positive charge on the bottom part of the multiferroic that will incline to be recompensed by the formation of negative carriers in the channel, thus depleting the channel of positive holes. Hence, it would be presumed that channel resistance increases when the multiferroic is positively biased and decreases when it is negatively biased. So, the device obviously performs as one would assume if the channel modulation was the result of a field effect. This result exhibits that a significantly improved, non-volatile ferroelectric field effect device can be fabricated from BFO/LSMO heterostructures where the magnetoresistive manganite serves as the channel semiconductor and multiferroic BFO as the gate dielectric. The improved interfacial phenomenon affiliated with the multiferroic-manganate (BFO/LSMO) interaction permits the fabrication of field effect devices where channel resistance varies at least a factor of 3 with high retention time.

V. BiFeO₃/La_{0.7}Sr_{0.3}MnO₃ SUPERLATTICES FOR ENHANCED INTERFACE INDUCED PROPERTIES

5.1 Introduction

Multifunctional complex oxide thin film heterostructures have received a great deal of attention as a result of their built-in competition among charge, spin, orbital and lattice degrees of freedom which could lead to exciting physical properties. These properties are important for application in various areas of electrical, optical, spintronic and next generation memory devices[1], [6], [7], [165]–[169]. However, single phase BFO possess a small magnetoelectric coupling between its ferroelectric-antiferromagnetic (FE-AFM) properties which makes it unsuitable for device applications[170]. Moreover, finding materials which exhibit several ferroic order simultaneously with strong ferromagnetism and ferroelectricity at room temperature remains at the preliminary stage of basic research[138]. Consequently, many techniques are being developed to increase the magnetoelectric coupling coefficient of BFO by modifying the exchange interaction when a ferromagnetic material is coupled with the antiferromagnetic properties in BFO[170].

The transition metal oxide La_{0.7}Sr_{0.3}MnO₃ (LSMO) is a well-known ferromagnetic (FM) oxide which is an excellent candidate for spintronic devices, due to high-ferromagnetic Curie temperature of $T_C=370$ K with charge carriers that could be 100% spin polarized, when combined with BFO, strong magnetoelectric coupling in heterostructures of BFO and LSMO is possible[139], [140], [165], [170]. Orbital reconstruction or hybridization at the interface between Fe³⁺ or Fe²⁺ of multiferroic (FE-AFM) BFO and Mn³⁺ or Mn⁴⁺ of ferromagnetic LSMO makes them two perfect candidates for device applications based on exchange bias[139], [165], [167], [171]. Previous experimental work

clearly found an emergent interfacial exchange bias at the BFO/LSMO interface[139], [140], [167]. Control of the FM spin alignment by an electric field when BFO is in close contact with ferromagnetic $\text{Co}_{0.9}\text{Fe}_{0.1}$ has been demonstrated by Chu et al.[144]. Similarly, the exchange bias (H_{EB}) controlled by electric field at the BFO/LSMO interface was demonstrated by Wu et al.[140] and the corresponding interface magnetism heteroepitaxially integrated on Si (100) was shown by Rao et al.[143] and on GaAs (001) was shown by Rahman et al.[167]. So far, interfacial exchange bias study was limited to BFO/LSMO bilayer structure only. The use of an epitaxial superlattices (SLs) of BFO/LSMO could further enhance the interfacial physical properties due to an increase of magnetic frustration, charge transfer, and orbital reconstruction across a number of interfaces compared to the epitaxially grown a single bilayer BFO/LSMO heterostructure[172]–[174]. Specifically, high quality interfaces and repetitive layers with nanoscale thicknesses of SLs have been found to be accountable for significant enhancement of exchange bias interaction at BFO/LSMO interfaces of the multilayer system[175].

In this chapter, systematically fabricated and studied of a series of epitaxial multiferroic/manganite superlattices composed of ultrathin BFO and LSMO layers monolithically integrated on SrTiO_3 buffered GaAs (001) substrate is outlined. It also consists rigorously studied magnetic properties for all the SLs structures and observed sizable low temperature magnetism with hysteresis loop in the SLs down to a BFO/LSMO layer thickness of few unit cells (u.c.), accompanied by drastically enhancement of coercive field of more than 1800 Oe. Furthermore, a remarkable enhanced exchange bias around $\sim \pm 850$ Oe was observed in the SLs which can be attributed to the strong magnetic coupling

across the BFO/LSMO interfaces.

5.2 Experimental

Epitaxial [(BFO)_m/(LSMO)_n]_N SLs as schematically shown in figure 5.1 where m is the number of u.c. of BFO and n is the number of u.c. of LSMO, repeated N times, were grown on (001) STO buffered (001) GaAs substrate using pulsed laser deposition (PLD). This work was facilitated by the deposition of an epitaxial 8 nm STO (001) buffer layer on GaAs (001) by molecular beam epitaxy (MBE). The LSMO and BFO repetitive layers were deposited by pulsed laser deposition (PLD) using KrF excimer laser ($\lambda = 248$ nm). The focused laser beam irradiated the circular stoichiometric targets with a laser energy density of ~ 2.5 Jcm⁻² at a repetition rate of 10 Hz in an oxygen ambient of 100 mTorr while the substrate temperature was maintained at 600 °C during the deposition process. The samples were then annealed at 500 °C for 30 min under the same O₂ pressure used during the growth, and finally cooled slowly under partial O₂ pressure after annealing. The BFO and LSMO layers have been designed to have the same thickness with a stacking period number (N=1, 2, 4, 8, 16, 32 and 64) as shown in figure 5.1.

To investigate the crystalline structure of our SLs, X-ray diffraction measurements were recorded using a Rigaku SmartLab X-ray diffractometer (Cu K α radiation) at an operating voltage of 40 kV and a current of 44 mA. The temperature and magnetic-field dependent magnetization measurements of BFO/LSMO SLs were carried out by utilizing the vibrating sample magnetometer (VSM) module of Quantum Design Physical Properties Measurement System (PPMS). The diamagnetic background contribution due to STO/GaAs substrate has been subtracted from all the data that are presented in this work. From the different SLs, a sample size of ~ 4 mm X 4 mm was used for magnetization

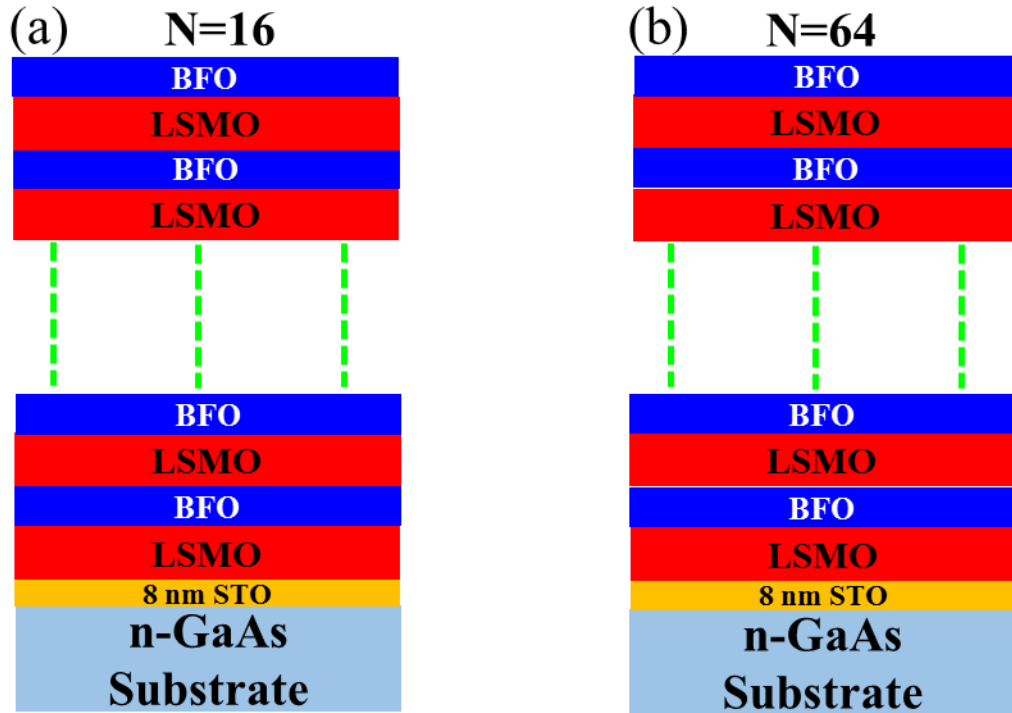


Figure 5.1: The sketch of the formula of BFO/LSMO superlattice structure. (a) BFO/LSMO superlattice with 16 stacking period with thicknesses of BFO=4.8 nm and LSMO=6.6 nm, (b) BFO/LSMO superlattice with 64 stacking period with thicknesses of BFO=1.2 nm and LSMO=1.6 nm respectively.

hysteresis (M–H) measurements. For the field-cooled (FC) and zero-field-cooled (ZFC) magnetization measurements, the sample was cooled down from 310 K to low temperature with and without the magnetic field parallel to the film plane, respectively. Both ZFC and FC magnetization versus temperature (M-T) curves were measured during the warming process.

The room temperature resistive switching characteristics of BFO/LSMO superlattices were carried out from top circular contacts which are about 1 mm apart from each other and I-V characteristics were measured by a semiconductor device analyzer (Keysight B1500A).

5.3 Results and Discussion

Figure 5.2 shows the typical XRD pattern of the as deposited $[(\text{BFO})_m/(\text{LSMO})_n]_N$ multilayered thin films on the 8 nm STO (001) buffered GaAs (001) substrate with different stacking periodic combinations (N). Only (001) oriented peaks appear in the 2θ -Omega scans for both the thin films and the substrates, indicating that the multilayered thin films have highly c-axis texture growth, or c-axis normal to the substrate surfaces. The full width at half maximum of the rocking curve around (001) plane for BFO and LSMO is 0.50 and 0.23 for N=1 and 0.72, 0.30 for N=2 films, respectively. As stacking number N reaches 32,

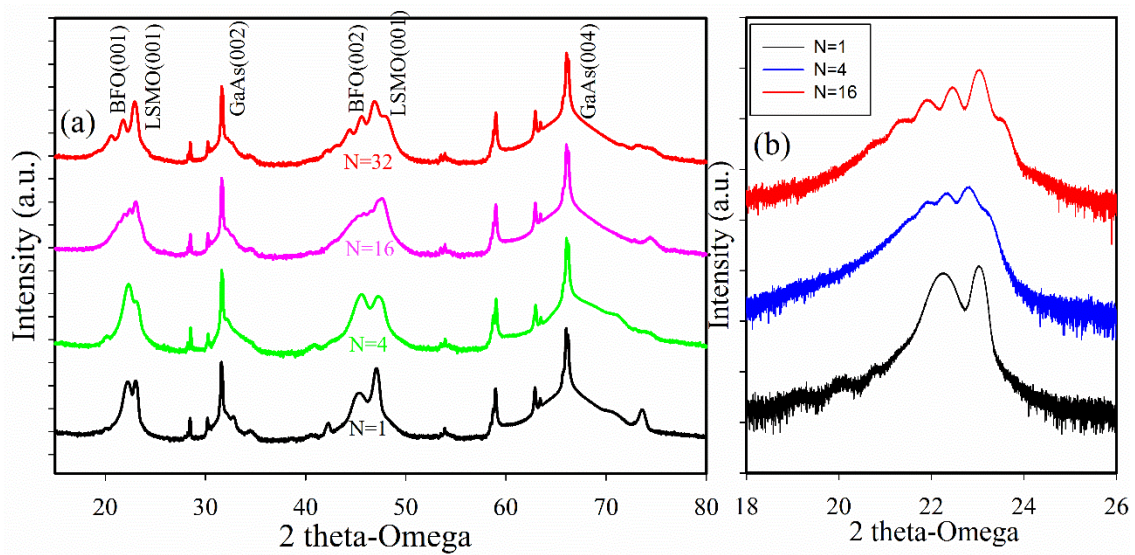


Figure 5.2: (a) Typical X-ray diffraction pattern of the as-grown BFO/LSMO superlattices deposited on STO (001) buffered GaAs (001) substrates with a same total deposition time but different N and (b) shows the rocking curve of superlattices with N=1, 4 and 16 around (001) plane.

the FWHM is 0.39 and 0.29 for (001) plane of BFO and LSMO respectively, indicates that it has good single crystallinity and epitaxial quality. It can be clearly seen that the XRD patterns have two sets of peaks when N is 1, one is from BFO and the other is from LSMO. With the increase of N to 4, 8, 16, 32 and 64, the satellite peaks appear, suggesting good interface structures and strong interface effects. The peaks at $2\theta \approx 21.87, 21.47$ and 23.50°

were identified as the satellite peaks for N=16. Thus, the multilayer thickness can be estimated from these satellite peaks using the standard formula $L = [\lambda_{Cu(K\alpha)} / (\sin\theta_{n+1} - \sin\theta_n)]$ [176], [177], where $\lambda_{Cu(K\alpha)}$ is the wavelength of the Cu(K α) radiation and n corresponds to the nth satellite peak [177]–[180]. Therefore, the thickness of every periodic layer (L) was found to be about 9.9 nm, giving the overall multilayer thickness of about 158.9 nm for N=16. This result is in good agreement with the multilayer design. The ϕ scans were also employed to study the epitaxial quality and the in-plane relationship between the multilayer and the substrate [167]. The ϕ peaks for the BFO (-101) are observed to be oriented 45° with respect to the GaAs (-202) and both the reflections are 90° apart from each other, which clearly indicates the presence of four-fold symmetry and demonstrates the device quality epitaxial film. The epitaxial relationship can be represented as BFO (001) // LSMO (001) // STO (001) // GaAs (001) or BFO [100] // LSMO [100] // STO [100] // GaAs [110], which agrees with the previous TEM results [167].

In figure 5.3 (a) show the magnetization versus magnetic field (M-Oe) of BFO/LSMO superlattices with N=1, 4, 16 and 64, measured at 5 K after cooling. The zero-field cooling (ZFC) and field cooling (FC) magnetization versus temperature (M-T) are presented in figure 5.3 (b). For all the field cooled magnetic measurement, the magnetic field was kept parallel to the samples. For the field cooled M-T measurement, data were collected during the warming cycle after the samples were cooled under the field of ± 1 Tesla. The Curie temperature for similar heterostructures is reported to be about 350 K which was not observed in our superlattices since our PPMS (VSM) measurement was limited to 310 K only [143], [167]. However, a variation in blocking temperature was obtained at which ZFC and FC of M-T curves split. Blocking temperature usually

resembles the temperature beyond which exchange bias shift or spin polarization effect disappears. The superlattice with increasing stacking periods shows a significantly higher blocking temperature comparing the BFO/LSMO bilayer heterostructure.

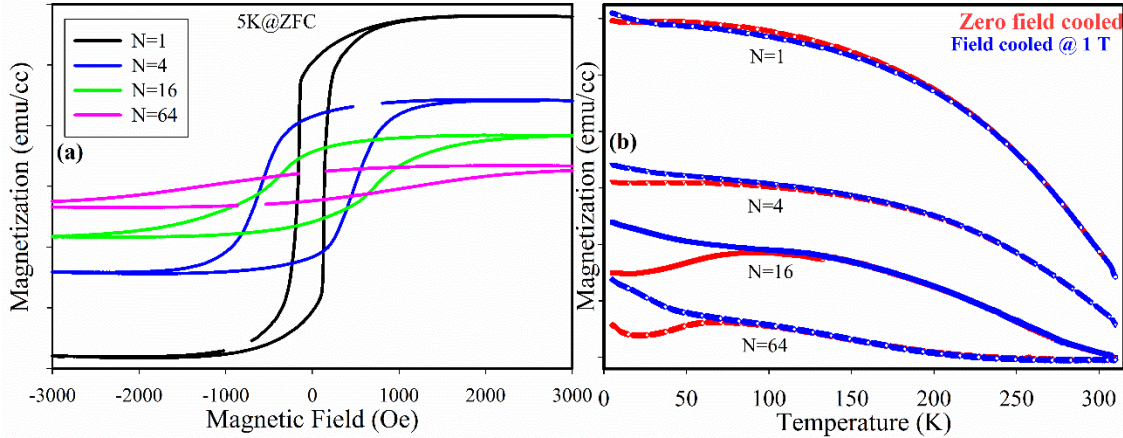


Figure 5.3: (a) Magnetic moment vs field hysteresis loop for BFO/LSMO superlattices with zero field cooling and (b) Zero field cooled and field cooled magnetic moment vs temperature curves for various superlattices.

In figure 5.3 (a), the magnetization curve of the superlattices shows a distinct enhancement of the coercive fields and a decrease in the saturation magnetization (M_s) with an increase of the stacking period. This could be explained by an increase of the existence of uncompensated moments or spins either pinned to ferromagnetic or antiferromagnetic layers at the interface[181], [182]. Moreover, the decrease of M_s is likely to be due to the formation of a strain induced layer in BFO through a Jahn-Teller (JT) effect in response to the LSMO layer or continuous increment of AFM-FM dragging between BFO and LSMO layer at the interface with increasing number of superlattice period[181]. Figure 5.3 (c) & 5.3 (d) shows the magnetization hysteresis loop of the superlattices measured at 5 K with in plane magnetic field after field cooling. The superlattice structures shows a distinct enhancement of the coercive field and, most significantly an enhanced shift of the

hysteresis loop is also observed with increasing stacking period. The shift of the hysteresis

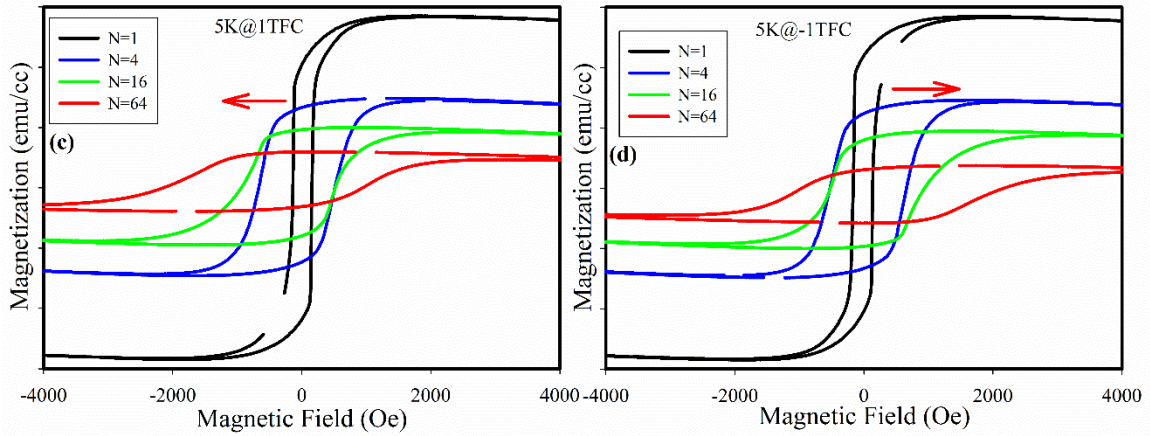


Figure 5.3: Magnetic moment vs field hysteresis loop for BFO/LSMO superlattices during field cooling with (c) +1 Tesla and (d) -1 Tesla.

loop is opposite to the direction of the cooling field, as expected from typical exchange bias behavior, and suggests ferromagnetic arrangement between the pinned, uncompensated spins of the antiferromagnetic BFO and the spins of the ferromagnetic LSMO[36], [44], [134]. Intrinsic Dzyaloshinskii-Moriya interaction and ferroelectric polarization has also been mentioned as a probable mechanism[183]. More detailed analysis of the dependence of exchange bias shift and coercive field enhancement with increasing periodicity of the superlattice structures are given in figure 5.4 (a) - (f) respectively. The shift in the M-H loop due to the exchange bias effect at the interface, significantly increased with increasing number of superlattice period as expected for typical exchange bias originating from the AFM-FM interfaces[36], [140], [155], [167]. With small number of period the magnetic properties are determined by the thick LSMO layer and a small difference can be observed between the coercive field and exchange bias shift. A much more drastic increase in H_C as high as ± 1800 Oe and H_{EB} as high as ± 850 Oe were observed if the number of period increases or decrease the thickness of

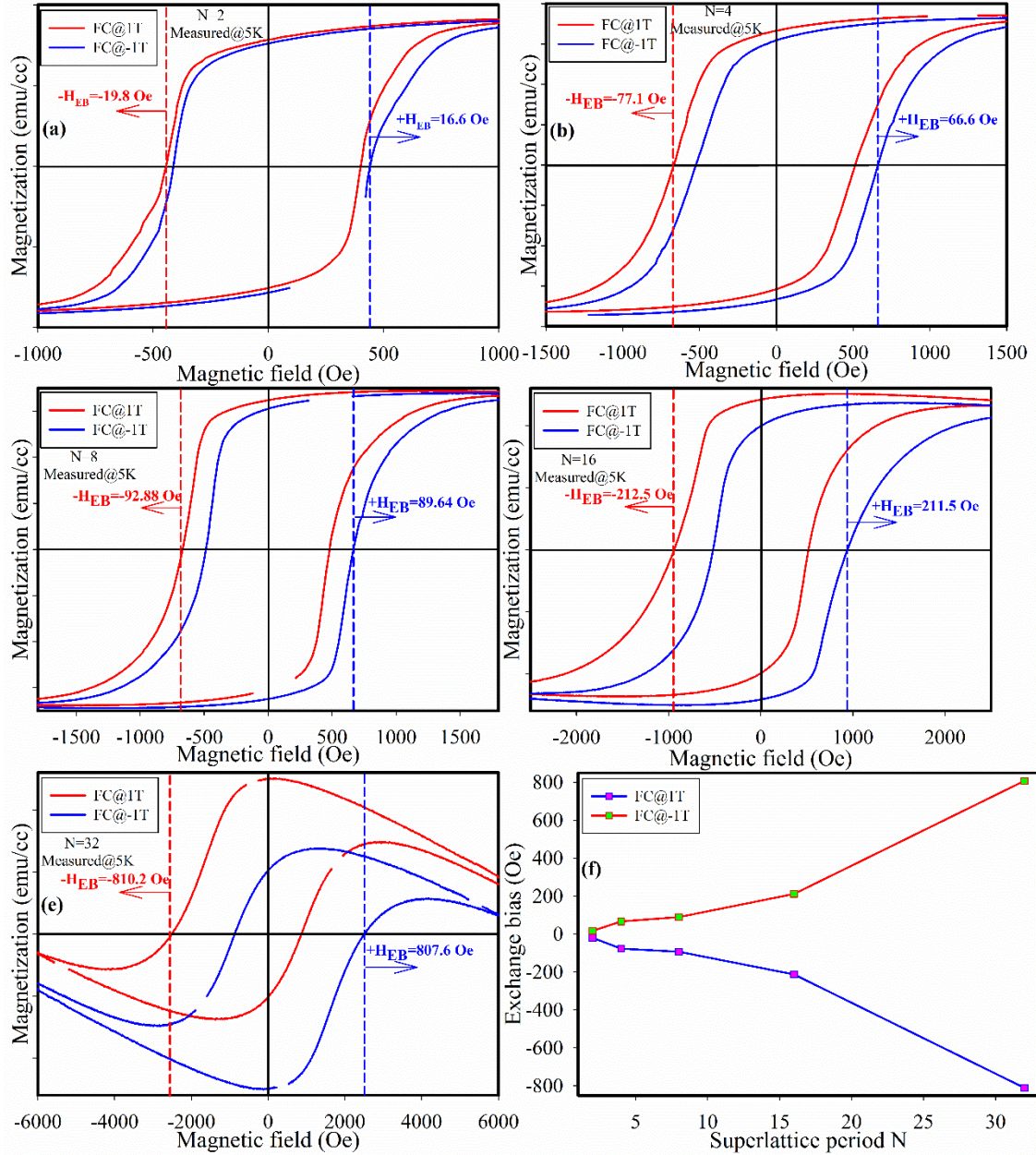


Figure 5.4: Magnetic hysteresis loop shifting or exchange bias for BFO/LSMO superlattices with (a) N=2, (b) N=4, (c) N=8, (d) N=16, (e) N=32 stacking period number and (f) shows the amount of exchange bias variation with N.

BFO/LSMO layer. The thickness of the ferromagnetic layer and exchange bias field are inversely proportional to each other. Single LSMO films exhibit a narrow coercive field with a transition above room temperature but the coercive field as well as the transition

temperature change significantly if the LSMO thickness is reduced below 5 nm[134]. This is usually explained by considering a strain-induced movement of MnO_6 octahedra according to the Jahn-Teller distortion theory[134], [157]. For quantification, it is computed the exchange bias field (H_{EB}) and coercive field (H_C) as $(H^+ + H^-)/2$ and $(H^+ - H^-)/2$ respectively, where H^+ and H^- denote the positive and negative coercive fields[36], [181]. Theoretically, exchange bias coupling cannot exist below the critical thickness of the antiferromagnetic layer[134], [184]. However, the variation of exchange bias as a function of antiferromagnetic thickness can be different from one material to another depending on the antiferromagnet anisotropy[45].

5.4 Resistive Switching in BFO/LSMO Superlattices

As a result of limitations of silicon-based technologies due to aggressive scaling to comply with Moore's law, research is driven to explore novel devices structures, technologies and materials to continue developing smaller, faster, cheaper, and more capable electronic devices[184]–[186]. Multifunctional oxides monolithically integrated onto semiconductors are becoming important because it offers a prospect for devices development that addresses the CMOS “end of roadmap” concerns by adding functionalities to Si-based devices[12]. Devices which reproducibly switch their resistance state between a high resistance state (HRS) and a low resistance state (LRS) with respect to the voltage sweep known as Resistive Random Access Memory (ReRAM) or memristor[145], [148], [149], [161], [187].

Resistive switching can be categorized as unipolar where switching mechanism does not rely on the polarity of voltage and current signal or bipolar where switching solely relies on the applied voltage polarity[185], [188]. Several reports have shown bipolar

resistive switching characteristics of ReRAMs based on BFO materials deposited on SrRuO₃[161], Nb-doped SrTiO₃[163], as well as Pt-coated Si substrate[149]. Due to high leakage current and high dielectric loss of BFO with applied electric field, ReRAMs devices based BFO only shows poor retention and endurance characteristics. In addition, ReRAM devices must have high ON/OFF ratio for fast reliable operation but simple BFO based ReRAM devices are limited for high speed and low-power memory applications due to its low ON/OFF ratio[149], [161], [163], [189]. It is expected that a unique and potentially stable resistance switching could be achieved throughout transport measurement in a multiferroics-transition metal oxide multilayer heterostructure with few unit cell thick layers.

Motivated by the above, BFO/LSMO superlattices were grown on STO buffered GaAs (001) substrates since GaAs possesses higher saturated electron velocity and mobility than Si allowing ReRAMs to operate at a much higher frequency with less noise. In the superlattices, the ferromagnetic LSMO and antiferromagnetic BFO layers are coupled with each other and by changing the magnetization with a suitably applied magnetic field, exchange bias effects can be observed[167]. In this chapter, BFO/LSMO superlattices as a potential candidate for ReRAM devices having stable resistive switching characteristics were demonstrated.

5.4.1 Electrical Characterization

Consistent bipolar resistive switching at low voltages within the range of -6 V to +6 V is observed in a BFO/LSMO superlattice structure consisting of 32 periods with a thickness of 170 nm. Figure 5.5 (a) and 5.5 (b) shows the same current-voltage (I-V) graph in both linear and logarithmic scale. The voltage was varied from 0 to 6 V, 6 to 0 V, 0 to -

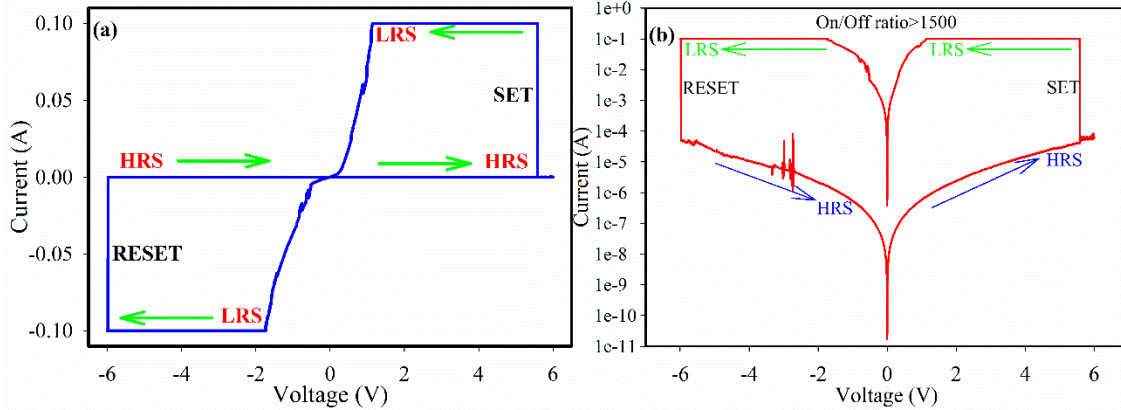


Figure 5.5: Room temperature bipolar resistive switching characteristics of BFO /LSMO superlattice for N=32 at (a) linear scale and (b) logarithmic scale.

6 V and -6 to 0 V, which are referred to as high resistance state (HRS), low resistance state (LRS), LRS, and HRS respectively. To prevent the formation process of conducting filaments between the electrodes, I-V characteristics were measured by low voltage sweeping with a current compliance of 100 mA set at the semiconductor device analyzer. The electroforming process needs to be eliminated to obtain stable and reproducible resistive switching with high retention time. To minimize the probability of dielectric break down of the device due to leakage current, a compliance current of 100 mA was used. The memory device was in HRS or virgin state when there is no applied bias. When the positive voltage was applied on the device, it was remained in HRS for 0 to 6 V. It was found that when voltage start decreasing from 6 V, current suddenly increased from 5×10^{-5} A to 9.8×10^{-2} A at 5.5 V. Increase in this current at 5.5 V can be referred to as LRS and the 5.5 V is referred as a SET voltage. The device remained in the LRS for decreasing voltage up to -6 V. The device is then switched from LRS to HRS at -6 V and the state changes from LRS to HRS at ~ -5.9 V. The device remained at the HRS state for increasing voltage from -5.9 to 0 V. The device can be triggered again from HRS to LRS state when +5.5 V was

applied at the electrode. To observe stable resistive switching, the above measurement steps were repeated for 20 times. The sequence of the applied bias voltage is shown by the arrows on the figure 5.5. This sequence of changing the resistance state from HRS-LRS-HRS is a typical representation of bipolar resistive switching[185], [190]. The set/reset voltage was found to be +5.5 V and -5.9 V, which is comparable with reports on other ferroelectric or oxides based memory devices[146], [161]–[163], [167]. In this study, low SET/RESET voltage of the ReRAM devices integrated with III-V semiconductor could lead us to future memory devices having low-power dissipation. It is important to mention that these devices are free from the development of conducting bridge filaments or any other electroforming process during SET/RESET operation. The present approach of device design using BFO/LSMO superlattices gives us low SET/RESET voltages that enhances reliability of the ReRAM devices by reducing the possibility of device failure from thermal damage due to electroforming process that is the case for some oxides and solid electrolytes based resistive NVM devices. This is a simple demonstration of a non-filament forming ReRAM and the operating voltage can be further reduced by scaling.

To examine the current conduction mechanism of BFO/LSMO superlattice based ReRAMs, I-V characteristics were analyzed to determine the conduction mechanisms. Such conduction mechanism includes as Ohmic conduction ($I \propto V$), Thermionic emission ($\ln I \propto V$), Space charge limited conduction ($I \propto V^\alpha$, where $\alpha \geq 2$), Poole-Frenkel emission [$\ln(I/V) \propto V^{1/2}$] and Fowler-Nordheim tunneling [$I \propto V^2 \exp(-E_a/V)$, where E_a is the kinetic energy of the charge carriers][145], [164], [167]. The device shown in figure 5.5 the conduction mechanisms were determined by fitting both the HRS and LRS I-V curves and it was found that space charge limited conduction (SCLC) mechanism is primarily

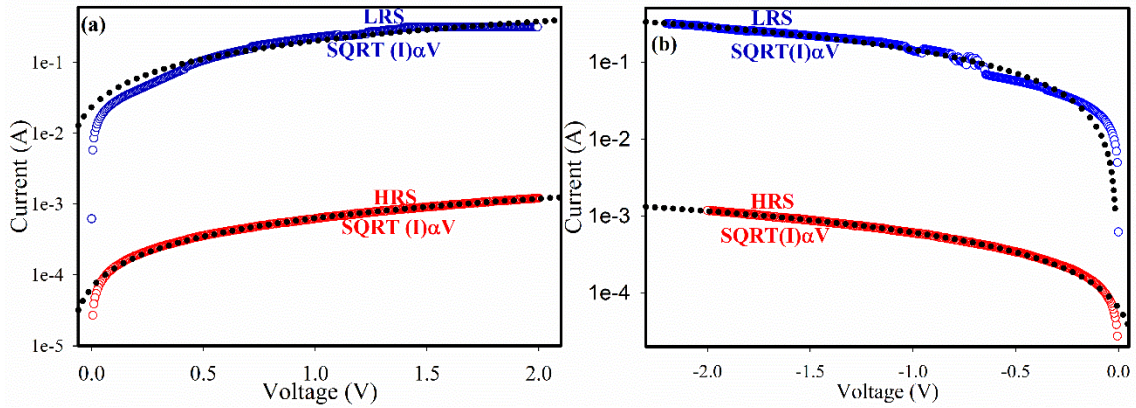


Figure 5.6: Carrier injection mechanism of BFO/LSMO superlattice in logarithmic scales during (a) positive voltage sweep and (b) negative voltage sweep.

responsible for resistive switching. I-V plots for both the positive and negative voltages with fitting in logarithmic scale are depicted in figure 5.6 (a) and (b). During the positive voltage sweeping, initial region of the plot followed the linear Ohmic behavior and then it follows the space charge limited conduction. In contrast, the fitting of the LRS is complicated and exhibited a combination of Ohmic region, thermionic emission and space charge limited conduction. However, during the negative voltage sweeping the conduction mechanism of LRS and HRS is similar to the HRS part of the positive voltage region. High ON/OFF ratio is desirable to obtain high reliability and performance for next generation ReRAM based NVM devices. Here the HRS region can be referred as off state, while, the LRS region can be considered as on state. It is interesting to note that the maximum ON/OFF ratio was found to be around $\sim >1500$. This ON/OFF ratio from the superlattice based devices are believed to be highest when compared with other simple ferroelectric NVM devices[161], [163], [191]. ReRAM devices based on BFO nanostructures offers small ON/OFF ratio (~ 500) comparing with the BFO/LSMO SLs[147]. Even though, the reported ON/OFF ratio was $\sim 10^4$ for Pt/BFO/Nb-STO based ReRAM by Hu et al.[146],

the authors fabricated their device on Nb-STO substrate which is not manufacturable and compatible with current CMOS technology. It is noteworthy to mention that these are the very first BFO/LSMO superlattice based ReRAM devices that are fabricated on GaAs (001) substrate and they present a strong potential for next generation low-power applications.

In conclusion, BFO/LSMO superlattices can be used to provide stable bipolar resistive switching behaviors with very high ON/OFF ratio. Merging of a superlattice structure with the low dimensionality of the individual layers can be used to obtain an improved bipolar resistive switching compared to simple single or bilayer structures. For such device, the memory window that is provided by the ON and OFF state would certainly permit the development of a fast and reliable memory for future data storage applications.

VI. CONCLUSION AND FUTURE WORK

6.1 Conclusion

The main objective of this research is to design, study and fabricate several thin film multifunctional hetero-structures which are potentially important for magnetic tunnel junction, multiferroic tunnel junction and magneto-electric devices. In particular, four different approaches to achieve epitaxial multifunctional heterostructures was investigated, as shown in Figure 6.1 (a) growth of multiferroics (MF) on STO buffered III-V semiconductor substrate; (b) growth of MF on epitaxial layer of conductive oxide on a STO buffered III-V semiconductor substrate; (c) growth of MF on epitaxial layer of ferromagnetic (FM) on a STO buffered III-V Semiconductor substrate; (d) growth of ferroelectric (FE) on epitaxial layer of FM on a III-V semiconductor substrate.

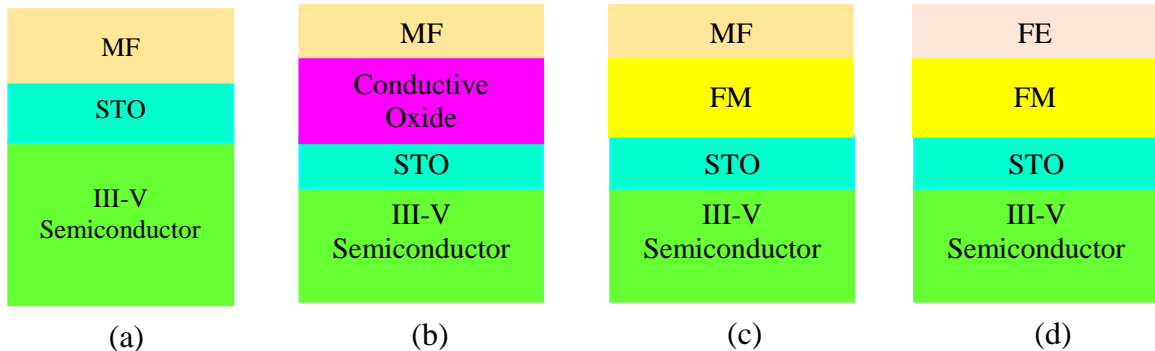


Figure 6.1: Four approaches used to integrate multifunctional oxide with III-V semiconductor.

6.2 Contributions of This Work

1. **Rahman, Md Shafiqur**, Susmita Ghose, Liang Hong, Juan S. Rojas-Ramirez, R. Droopad, “BiFeO₃/La_{0.7}Sr_{0.3}MnO₃ superlattice hetero-structures for enhanced interface induced properties”, (Manuscript in preparation).
2. Susmita Ghose, **Md. Shafiqur Rahman**, J. S. Rojas-Ramirez, R. Droopad, “Growth and Characterization of β -Ga₂O₃ thin film by Molecular Beam Epitaxy for Deep-UV photodetector”, (submitted).

3. **Rahman, Md Shafiqur**, Susmita Ghose, Liang Hong, Pradip Dhungana, Abbas Fahami, Javad R. Gatabi, Juan S. Rojas-Ramirez et al. "Integration of BiFeO₃/La_{0.7}Sr_{0.3}MnO₃ heterostructures with III–V semiconductors for low-power non-volatile memory and multiferroic field effect transistors." *Journal of Materials Chemistry C* 4, no. 43 (2016): 10386-10394.
4. **Rahman, Md Shafiqur**, Susmita Ghose, Javad R. Gatabi, Juan S. Rojas-Ramirez, R. K. Pandey, and Ravi Droopad. "Heteroepitaxial growth and characterization of BiFeO₃ thin films on GaAs." *Materials Research Express* 3, no. 10 (2016): 106408.
5. Gatabi, Javad R., **Shafiqur Rahman**, Ana Amaro, Taylor Nash, Juan Rojas-Ramirez, R. K. Pandey, and Ravi Droopad. "Tuning electrical properties of PZT film deposited by Pulsed Laser Deposition." *Ceramics International* 43, no. 8 (2017): 6008-6012.
6. Ghose, Susmita, **Md Shafiqur Rahman**, Juan Salvador Rojas-Ramirez, Manuel Caro, Ravi Droopad, Abraham Arias, and Nicola Nedev. "Structural and optical properties of β -Ga₂O₃ thin films grown by plasma-assisted molecular beam epitaxy." *Journal of Vacuum Science & Technology B, Nanotechnology and Microelectronics: Materials, Processing, Measurement, and Phenomena* 34, no. 2 (2016): 02L109.
7. Gatabi, Javad, Kevin Lyon, **Shafiqur Rahman**, Manuel Caro, Juan Rojas-Ramirez, Joelson Cott-Garcia, Ravi Droopad, and Byounggak Lee. "Functional materials integrated on III–V semiconductors." *Microelectronic Engineering* 147 (2015): 117-121.

6.3 Future Work

These alternate techniques of exploring single-phase multiferroics was done to find efficient approach to develop the magneto-electric based devices where multiferroics are placed to affect magnetism[39].

Several researchers have mentioned that the electric control of exchange bias is an essential

first step to utilize this technique. If exchange bias shift is achievable by external electric field, then the magnetization of FM material can be switched easily and magneto-electric coupling can be achieved accordingly shown in figure 6.2. Magneto-electric random access memory (MeRAM), has appeared as a probable alternative for current memory devices

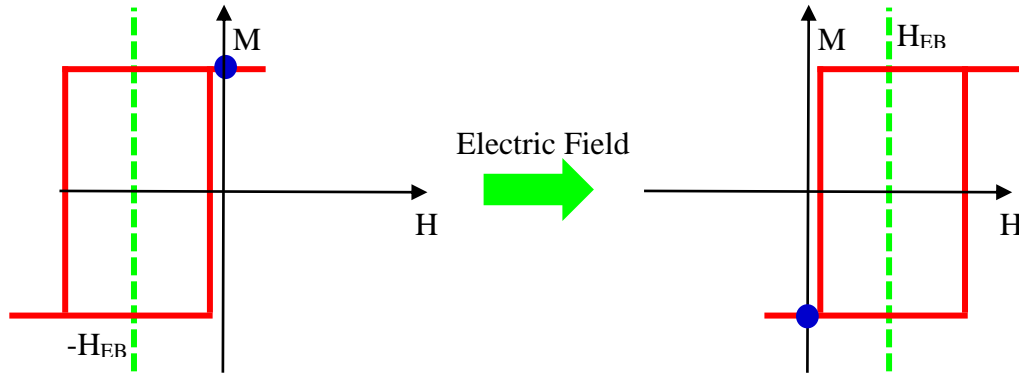


Figure 6.2: A schematic illustrating the control of magnetization in a ferromagnetic material from the electric control of exchange bias.

that offers low power consumption in write operations and non-destructive reading[7]. The concept of MeRAM was first enumerated using the combination of tunnel electro-resistance (TER) and tunnel magneto-resistance (TMR) effects in magneto-electric tunnel junctions (METJ) by Zhuravlev et al.[192]. A schematic of possible MeRAM device structure is depicted in figure 6.3 below[7], where two FM layers are usually segregated by insulating barrier. So depending on the magnetization configuration or spin alignment of the two FM layers (parallel or antiparallel), there is an expectation for low or high resistance state which is also similar to TMR effect. Moreover, a multiferroic (FE-AFM) layer is positioned in the bottom of two FM layer. Now the ferroelectric polarization could be switched by electric field applied across the multiferroic layer will reverse the spin state

at the interface of the AFM only if the magneto-electric coupling is strong enough in the

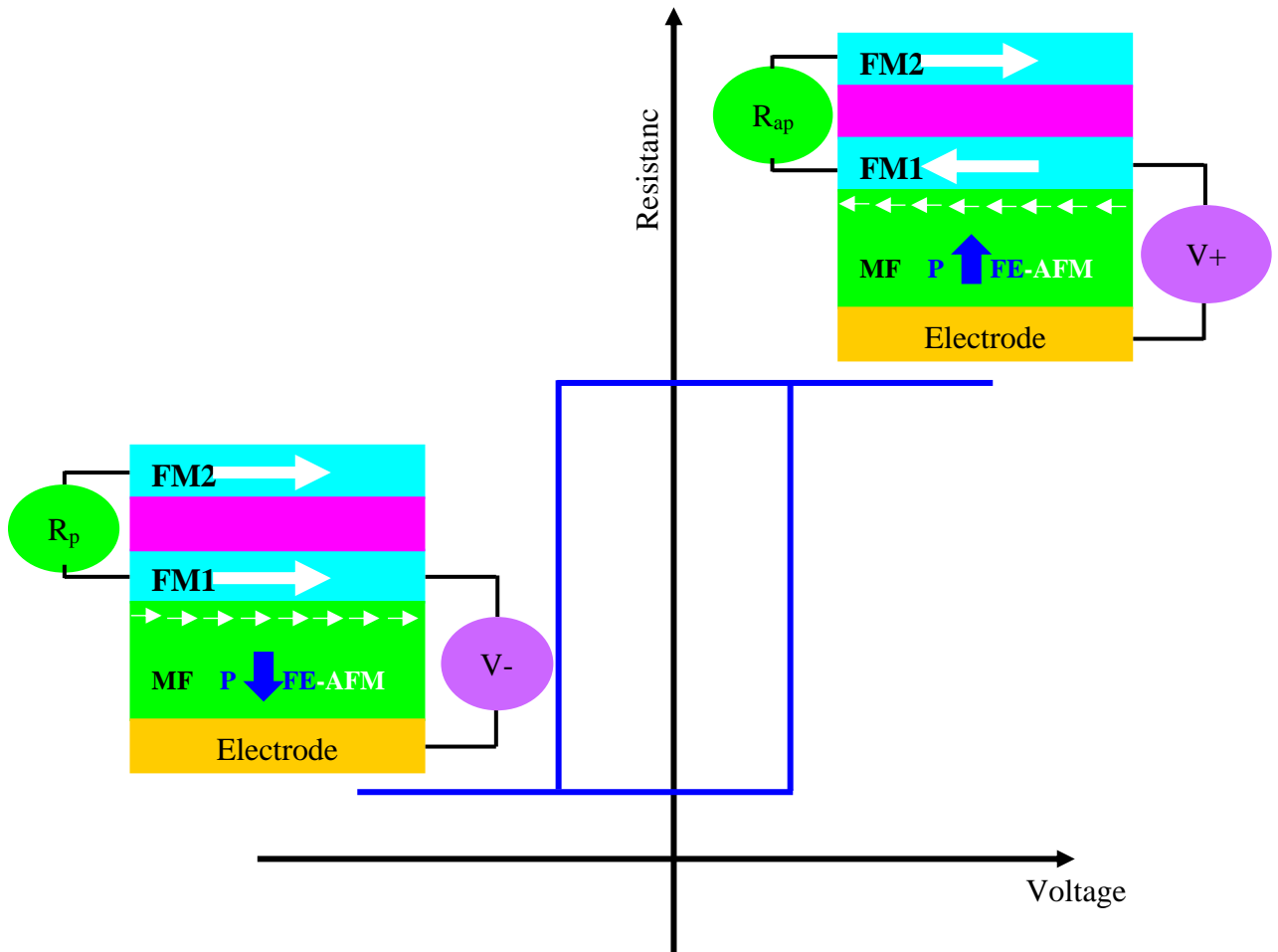


Figure 6.3: Sketch of a possible MeRAM element where two ferromagnetic layers (FM1 & FM2) are aligned. Low or high resistance state depends on the magnetic spin arrangement (parallel or antiparallel) of the FM layers. A bottom FM layer is on the multiferroic layer and if the magnetization of the bottom FM layer is coupled to the spins in the multiferroic (small white arrows) and if the magneto-electric coupling is strong enough, reversing the ferroelectric polarization P in the multiferroic changes the magnetic spin arrangement in the trilayer from parallel to antiparallel, and the resistance from R_p to antiparallel (R_{AP}).

multiferroic layer. This may form the basis of switching the magnetization configuration of bottom FM layer, with resulting parallel to antiparallel arrangement of spin directions in the two FM layers. This will reverse the junction resistance from low to high due to switching in magnetic spin arrangements. Here, it is essential to mention that instead of

using a larger current only an electric field is used to control the magnetic spin arrangement (parallel-antiparallel) which is a key advantage of MeRAM than MRAM. Therefore, for low power operation of memory or spintronic devices the ferroelectric control of spin polarization is crucial. Even though few researchers have gained considerable success to control exchange bias using electric field, but they use different materials and device structures which have its own unique limitations for operation. For example, Laukhin et al. showed irreversibly suppressed exchange bias using multiferroic YMnO₃/permalloy bilayers[193], and He et al. showed reversible switching among two different exchange bias states by the application of electric field using Cr₂O₃ coupled to Pd/Co multilayers[194].

REFERENCES

- [1] H. Béa, M. Gajek, M. Bibes, and A. Barthélémy, “Spintronics with multiferroics,” *J. Phys. Condens. Matter*, vol. 20, no. 43, p. 434221, 2008.
- [2] H. Schmid, “Multi-ferroic magnetoelectrics,” *Ferroelectrics*, vol. 162, no. 1, pp. 317–338, 1994.
- [3] N. A. Spaldin and M. Fiebig, “The renaissance of magnetoelectric multiferroics,” *Science (80-.)*, vol. 309, no. 5733, pp. 391–392, 2005.
- [4] W. Eerenstein, N. D. Mathur, and J. F. Scott, “Multiferroic and magnetoelectric materials,” *Nature*, vol. 442, no. 7104, pp. 759–765, 2006.
- [5] N. Izyumskaya, Y. Alivov, and H. Morkoc, “Oxides, oxides, and more oxides: High- κ oxides, ferroelectrics, ferromagnetics, and multiferroics,” *Crit. Rev. Solid State Mater. Sci.*, vol. 34, no. 3–4, pp. 89–179, 2009.
- [6] M. Gajek, M. Bibes, S. Fusil, K. Bouzehouane, J. Fontcuberta, A. Barthélémy, and A. Fert, “Tunnel junctions with multiferroic barriers,” *Nat. Mater.*, vol. 6, no. 4, pp. 296–302, 2007.
- [7] M. Bibes and A. Barthélémy, “Towards a magnetoelectric memory,” *Nat. Mater.*, vol. 7, pp. 425–426, 2008.
- [8] N. A. Hill, “Why Are There so Few Magnetic Ferroelectrics?,” pp. 6694–6709, 2000.
- [9] C.-W. Nan, M. I. Bichurin, S. Dong, D. Viehland, and G. Srinivasan, “Multiferroic magnetoelectric composites: historical perspective, status, and future directions,” *J. Appl. Phys.*, vol. 103, no. 3, p. 1, 2008.
- [10] R. A. McKee, F. J. Walker, and M. F. Chisholm, “Crystalline oxides on silicon: the first five monolayers,” *Phys. Rev. Lett.*, vol. 81, no. 14, p. 3014, 1998.
- [11] R. Droopad, Z. Yu, H. Li, Y. Liang, C. Overgaard, A. Demkov, X. Zhang, K. Moore, K. Eisenbeiser, and M. Hu, “Development of integrated heterostructures on silicon by MBE,” *J. Cryst. Growth*, vol. 251, no. 1, pp. 638–644, 2003.
- [12] R. Droopad and B. Lee, “Heterointegration of Dissimilar Materials,” DTIC Document, 2015.
- [13] V. Wadhawan, *Introduction to ferroic materials*. CRC Press, 2000.

- [14] M. E. Lines and A. M. Glass, *Principles and applications of ferroelectrics and related materials*. Oxford university press, 1977.
- [15] R. P. Feynman, R. B. Leighton, and M. Sands, “The feynman lectures on physics; vol. i,” *Am. J. Phys.*, vol. 33, no. 9, pp. 750–752, 1965.
- [16] A. Aird and E. K. H. Salje, “Sheet superconductivity in twin walls: experimental evidence of,” *J. Phys. Condens. Matter*, vol. 10, no. 22, p. L377, 1998.
- [17] M. Fiebig, “Revival of the magnetoelectric effect,” *J. Phys. D. Appl. Phys.*, vol. 38, no. 8, p. R123, 2005.
- [18] W. F. Brown Jr, R. M. Hornreich, and S. Shtrikman, “Upper bound on the magnetoelectric susceptibility,” *Phys. Rev.*, vol. 168, no. 2, p. 574, 1968.
- [19] M. P. Curie, “phénomènes physiques les considérations sur la symétrie fami-lières aux cristallographes.,” 1894.
- [20] D. N. Astrov, “Magnetoelectric effect in chromium oxide,” *Sov. Phys. JETP*, vol. 13, no. 4, pp. 729–733, 1961.
- [21] Y. Benveniste, “A new approach to the application of Mori-Tanaka’s theory in composite materials,” *Mech. Mater.*, vol. 6, no. 2, pp. 147–157, 1987.
- [22] T. Kimura, T. Goto, H. Shintani, K. Ishizaka, T. Arima, and Y. Tokura, “Magnetic control of ferroelectric polarization,” *Nature*, vol. 426, no. 6962, pp. 55–58, 2003.
- [23] N. Hur, S. Park, P. A. Sharma, J. S. Ahn, S. Guha, and S. W. Cheong, “Electric polarization reversal and memory in a multiferroic material induced by magnetic fields,” *Nature*, vol. 429, no. 6990, pp. 392–395, 2004.
- [24] J. Zhang, “Growth and characterization of magnetoelectric and multiferroic oxide thin films.” The Hong Kong Polytechnic University, 2009.
- [25] O. Heyer, N. Hollmann, I. Klassen, S. Jodlauk, L. Bohatý, P. Becker, J. A. Mydosh, T. Lorenz, and D. Khomskii, “A new multiferroic material: MnWO_4 ,” *J. Phys. Condens. matter*, vol. 18, no. 39, p. L471, 2006.
- [26] S. Lee, A. Pirogov, M. Kang, K.-H. Jang, M. Yonemura, T. Kamiyama, S.-W. Cheong, F. Gozzo, N. Shin, and H. Kimura, “Giant magneto-elastic coupling in multiferroic hexagonal manganites,” *Nature*, vol. 451, no. 7180, pp. 805–808, 2008.
- [27] M. A. Subramanian, T. He, J. Chen, N. S. Rogado, T. G. Calvarese, and A. W. Sleight, “Giant room-temperature magnetodielectric response in the electronic ferroelectric LuFe_2O_4 ,” *Adv. Mater.*, vol. 18, no. 13, pp. 1737–1739, 2006.

- [28] J. Wang, J. B. Neaton, H. Zheng, V. Nagarajan, S. B. Ogale, B. Liu, D. Viehland, V. Vaithyanathan, D. G. Schlom, and U. V. Waghmare, "Epitaxial BiFeO₃ multiferroic thin film heterostructures," *Science* (80-.), vol. 299, no. 5613, pp. 1719–1722, 2003.
- [29] T. Zhao, A. Scholl, F. Zavaliche, K. Lee, M. Barry, A. Doran, M. P. Cruz, Y. H. Chu, C. Ederer, and N. A. Spaldin, "Electrical control of antiferromagnetic domains in multiferroic BiFeO₃ films at room temperature," *Nat. Mater.*, vol. 5, no. 10, pp. 823–829, 2006.
- [30] H. Béa, M. Bibes, F. Ott, B. Dupé, X.-H. Zhu, S. Petit, S. Fusil, C. Deranlot, K. Bouzehouane, and A. Barthélémy, "Mechanisms of exchange bias with multiferroic BiFeO₃ epitaxial thin films," *Phys. Rev. Lett.*, vol. 100, no. 1, p. 17204, 2008.
- [31] N. Mathur, "Materials science: A desirable wind up," *Nature*, vol. 454, no. 7204, pp. 591–592, 2008.
- [32] Y. E. Roginskaya, Y. Y. Tomashpol'Skii, Y. N. Venevtsev, V. M. Petrov, and G. S. Zhdanov, "The nature of the dielectric and magnetic properties of BiFeO₃," *Sov. J. Exp. Theor. Phys.*, vol. 23, p. 47, 1966.
- [33] T. Kimura, G. Lawes, and A. P. Ramirez, "Electric polarization rotation in a hexaferrite with long-wavelength magnetic structures," *Phys. Rev. Lett.*, vol. 94, no. 13, p. 137201, 2005.
- [34] Y.-H. Chu, L. W. Martin, M. B. Holcomb, and R. Ramesh, "Controlling magnetism with multiferroics," *Mater. Today*, vol. 10, no. 10, pp. 16–23, 2007.
- [35] H. Béa, M. Bibes, A. Barthélémy, K. Bouzehouane, E. Jacquet, A. Khodan, J.-P. Contour, S. Fusil, F. Wyczisk, and A. Forget, "Influence of parasitic phases on the properties of BiFeO₃ epitaxial thin films," *arXiv Prepr. cond-mat/0504631*, 2005.
- [36] J. Nogués and I. K. Schuller, "Exchange bias," *J. Magn. Magn. Mater.*, vol. 192, no. 2, pp. 203–232, 1999.
- [37] W. H. Meiklejohn and C. P. Bean, "New magnetic anisotropy," *Phys. Rev.*, vol. 102, no. 5, p. 1413, 1956.
- [38] R. Ramesh and N. A. Spaldin, "Multiferroics: progress and prospects in thin films," *Nat. Mater.*, vol. 6, no. 1, pp. 21–29, 2007.
- [39] C. A. F. Vaz, "Electric field control of magnetism in multiferroic heterostructures," *J. Phys. Condens. Matter*, vol. 24, no. 33, p. 333201, 2012.

- [40] M. Kiwi, “Exchange bias theory,” *J. Magn. Magn. Mater.*, vol. 234, no. 3, pp. 584–595, 2001.
- [41] J. Nogués, J. Sort, V. Langlais, V. Skumryev, S. Surinach, J. S. Muñoz, and M. D. Baró, “Exchange bias in nanostructures,” *Phys. Rep.*, vol. 422, no. 3, pp. 65–117, 2005.
- [42] D. Mauri, H. C. Siegmann, P. S. Bagus, and E. Kay, “Simple model for thin ferromagnetic films exchange coupled to an antiferromagnetic substrate,” *J. Appl. Phys.*, vol. 62, no. 7, pp. 3047–3049, 1987.
- [43] A. P. Malozemoff, “Random-field model of exchange anisotropy at rough ferromagnetic-antiferromagnetic interfaces,” *Phys. Rev. B*, vol. 35, no. 7, p. 3679, 1987.
- [44] H. Ohldag, A. Scholl, F. Nolting, E. Arenholz, S. Maat, A. T. Young, M. Carey, and J. Stöhr, “Correlation between exchange bias and pinned interfacial spins,” *Phys. Rev. Lett.*, vol. 91, no. 1, p. 17203, 2003.
- [45] F. Radu and H. Zabel, “Exchange bias effect of ferro-/antiferromagnetic heterostructures,” in *Magnetic heterostructures*, Springer, 2008, pp. 97–184.
- [46] D. L. Smith, *Thin-film deposition: principles and practice*, vol. 108. McGraw-Hill New York etc, 1995.
- [47] M. Ohring, *Materials science of thin films*. Academic press, 2001.
- [48] W. A. Doolittle, A. G. Carver, and W. Henderson, “Molecular beam epitaxy of complex metal-oxides: Where have we come, where are we going, and how are we going to get there?,” *J. Vac. Sci. Technol. B Microelectron. Nanom. Struct. Process. Meas. Phenom.*, vol. 23, no. 3, pp. 1272–1276, 2005.
- [49] A. A. Demkov and A. B. Posadas, *Integration of functional oxides with semiconductors*. Springer, 2014.
- [50] R. F. Bunshah, *Handbook of deposition technologies for films and coatings: science, technology, and applications*. William Andrew, 1994.
- [51] D. Dijkkamp, T. Venkatesan, X. D. Wu, S. A. Shaheen, N. Jisrawi, Y. H. Min-Lee, W. L. McLean, and M. Croft, “Preparation of Y-Ba-Cu oxide superconductor thin films using pulsed laser evaporation from high T_c bulk material,” *Appl. Phys. Lett.*, vol. 51, no. 8, pp. 619–621, 1987.

- [52] D. D. Berkley, B. R. Johnson, N. Anand, K. M. Beauchamp, L. E. Conroy, A. M. Goldman, J. Maps, K. Mauersberger, M. L. Mecartney, and J. Morton, "Ozone processing of MBE grown of YBa/sub2/Cu/sub3/O/sub7-x/films," *IEEE Trans. Magn.*, vol. 25, no. 2, pp. 2522–2525, 1989.
- [53] M. Henini, *Molecular beam epitaxy: from research to mass production*. Newnes, 2012.
- [54] R. F. C. Farrow, *Molecular beam epitaxy: applications to key materials*. Elsevier, 1995.
- [55] C. E. C. Wood, D. Desimone, K. Singer, and G. W. Wicks, "Magnesium-and calcium-doping behavior in molecular-beam epitaxial III-V compounds," *J. Appl. Phys.*, vol. 53, no. 6, pp. 4230–4235, 1982.
- [56] A. Y. Cho, "Growth of III–V semiconductors by molecular beam epitaxy and their properties," *Thin Solid Films*, vol. 100, no. 4, pp. 291–317, 1983.
- [57] T. Y. Kometani and W. Wiegmann, "Measurement of Ga and Al in a molecular-beam epitaxy chamber by atomic absorption spectrometry (AAS)," *J. Vac. Sci. Technol.*, vol. 12, no. 4, pp. 933–936, 1975.
- [58] Y. Wei, X. Hu, Y. Liang, D. C. Jordan, B. Craigo, R. Droopad, Z. Yu, A. Demkov, J. L. Edwards Jr, and W. J. Ooms, "Mechanism of cleaning Si (100) surface using Sr or SrO for the growth of crystalline SrTiO₃ films," *J. Vac. Sci. Technol. B Microelectron. Nanom. Struct. Process. Meas. Phenom.*, vol. 20, no. 4, pp. 1402–1405, 2002.
- [59] J. M. Van Hove, P. P. Chow, A. M. Wowchak, J. J. Klaassen, R. Hickman, and C. Polley, "Molecular beam epitaxy grown InGaN multiple quantum well structures optimized using in situ cathodoluminescence," *J. Vac. Sci. Technol. B Microelectron. Nanom. Struct. Process. Meas. Phenom.*, vol. 16, no. 3, pp. 1286–1288, 1998.
- [60] P. Staib, W. Tappe, and J. P. Contour, "Imaging energy analyzer for RHEED: energy filtered diffraction patterns and in situ electron energy loss spectroscopy," *J. Cryst. Growth*, vol. 201, pp. 45–49, 1999.
- [61] K. Bhatnagar, J. S. Rojas-Ramirez, R. Contreras-Guerrero, M. Caro, and R. Droopad, "Heterointegration of III–V on silicon using a crystalline oxide buffer layer," *J. Cryst. Growth*, vol. 425, pp. 262–267, 2015.
- [62] G. N. Maracas, J. L. Edwards, K. Shiralagi, K. Y. Choi, R. Droopad, B. Johs, and J. A. Woolam, "In situ spectroscopic ellipsometry in molecular beam epitaxy," *J. Vac. Sci. Technol. A Vacuum, Surfaces, Film.*, vol. 10, no. 4, pp. 1832–1839, 1992.

- [63] K. Bhatnagar, J. Rojas-Ramirez, M. Caro, R. Contreras, B. Henninger, and R. Droopad, "In-situ monitoring during MBE growth of InAs based heterostructures," *J. Cryst. Growth*, vol. 425, pp. 16–20, 2015.
- [64] "Oxide MBE Lab | Max Planck Institut für Festkörperforschung." [Online]. Available: https://www.fkf.mpg.de/273938/30_Oxide_MBE_Lab. [Accessed: 21-Apr-2017].
- [65] D. M. Mattox, *Handbook of physical vapor deposition (PVD) processing*. William Andrew, 2010.
- [66] R. Mercier and A. A. Rusterholz, "International Union for Vacuum Science, Technique and Applications Union Internationale pour la Science, la Technique et les Applications du Vide Internationale Union der Forschung, Technik," 1967.
- [67] R. Eason, *Pulsed laser deposition of thin films: applications-led growth of functional materials*. John Wiley & Sons, 2007.
- [68] M. N. R. Ashfold, F. Claeysens, G. M. Fuge, and S. J. Henley, "Pulsed laser ablation and deposition of thin films," *Chem. Soc. Rev.*, vol. 33, no. 1, pp. 23–31, 2004.
- [69] "Adnano UHV Deposition - Lasalle Scientific Inc." [Online]. Available: <http://lasallescscientific.com/adnano-uhv-deposition/>. [Accessed: 21-Apr-2017].
- [70] J. A. Greer, "History and current status of commercial pulsed laser deposition equipment," *J. Phys. D. Appl. Phys.*, vol. 47, no. 3, p. 34005, 2013.
- [71] K. L. Saenger, D. B. Chrisey, and G. K. Hubler, "Pulsed Laser Deposition of Thin Films," *Kluwer, New York*, 1994.
- [72] M. G. Norton and C. B. Carter, "On the optimization of the laser ablation process for the deposition of $\text{YBa}_2\text{Cu}_3\text{O}_{7-\delta}$ thin films," *Phys. C Supercond.*, vol. 172, no. 1, pp. 47–56, 1990.
- [73] L. W. Martin, Y.-H. Chu, and R. Ramesh, "Advances in the growth and characterization of magnetic, ferroelectric, and multiferroic oxide thin films," *Mater. Sci. Eng. R Reports*, vol. 68, no. 4, pp. 89–133, 2010.
- [74] "Sputtering - Wang Li." [Online]. Available: <http://www.wangli.info/sputtering.html>. [Accessed: 21-Apr-2017].
- [75] H. P. Meyers and H. P. Myers, *Introductory solid state physics*. CRC press, 1997.
- [76] T. Mitsunaga, "X-ray thin film measurement techniques II. Out-of-plane diffraction measurements," *Rigaku J.*, vol. 25, no. 1, pp. 7–12, 2009.

- [77] K. Inaba, S. Kobayashi, K. Uehara, A. Okada, S. L. Reddy, and T. Endo, "High Resolution X-Ray Diffraction Analyses of (La,Sr)MnO₃/ZnO/Sapphire(0001) Double Heteroepitaxial Films," 2013.
- [78] K. Inaba, "X-ray thin-film measurement techniques," *Overview. Rigaku J*, vol. 24, no. 1, 2008.
- [79] T. Konya, "X-Ray Thin-Film Measurement Techniques III. High Resolution X-Ray Diffractometry," *Rigaku J.*, vol. 25, no. 2, pp. 1–8, 2009.
- [80] S. Kobayashi and K. Inaba, "X-ray thin-film measurement techniques," *mass Spectrosc. equipped with a Ski. interface*, p. 8, 2012.
- [81] S. Kobayashi, "X-Ray Thin-Film Measurement Techniques IV. In-Plane Diffraction Measurements," *Rigaku J.*, vol. 26, no. 1, pp. 3–11, 2010.
- [82] "Instrumentation - Electron Microanalysis Core Facility - Northern Arizona University." [Online]. Available: <http://nau.edu/cefns/labs/electron-microprobe/glg-510-class-notes/instrumentation/>. [Accessed: 21-Apr-2017].
- [83] J. Goldstein, D. E. Newbury, P. Echlin, D. C. Joy, A. D. Romig Jr, C. E. Lyman, C. Fiori, and E. Lifshin, *Scanning electron microscopy and X-ray microanalysis: a text for biologists, materials scientists, and geologists*. Springer Science & Business Media, 2012.
- [84] P. M. A. Sherwood, *Auger and X-ray photoelectron spectroscopy*, vol. 1. Chichester, England, 1990.
- [85] B. V. Crist, *Handbooks of monochromatic XPS spectra*. XPS International, 1999.
- [86] "UHVL." [Online]. Available: <http://jacobs.physik.uni-saarland.de/english/instrumentation/uhvl.htm>. [Accessed: 21-Apr-2017].
- [87] M. P. Seah and W. A. Dench, "Quantitative electron spectroscopy of surfaces: a standard data base for electron inelastic mean free paths in solids," *Surf. interface Anal.*, vol. 1, no. 1, pp. 2–11, 1979.
- [88] C. J. Powell, "Attenuation lengths of low-energy electrons in solids," *Surf. Sci.*, vol. 44, no. 1, pp. 29–46, 1974.
- [89] A. Jablonski and C. J. Powell, "Practical expressions for the mean escape depth, the information depth, and the effective attenuation length in Auger-electron spectroscopy and x-ray photoelectron spectroscopy," *J. Vac. Sci. Technol. A Vacuum, Surfaces, Film.*, vol. 27, no. 2, pp. 253–261, 2009.

- [90] N. Jalili and K. Laxminarayana, “A review of atomic force microscopy imaging systems: application to molecular metrology and biological sciences,” *Mechatronics*, vol. 14, no. 8, pp. 907–945, 2004.
- [91] R. Waser, H. Keller, and U. Erb, “Nanoelectronics and Information Technology: Advanced Electronic Materials and Novel Devices,” *MRS Bull.*, 2004.
- [92] “AFM — Cellular and Molecular Biomechanics Laboratory.” [Online]. Available: <http://biomechanicalregulation-lab.org/afm/>. [Accessed: 21-Apr-2017].
- [93] R. W. Carpick and M. Salmeron, “Scratching the surface: fundamental investigations of tribology with atomic force microscopy,” *Chem. Rev.*, vol. 97, no. 4, pp. 1163–1194, 1997.
- [94] T. Mitsui, “Ferroelectrics and antiferroelectrics,” in *Springer Handbook of Condensed Matter and Materials Data*, Springer, 2005, pp. 903–938.
- [95] P.-P. Shi, Y.-Y. Tang, P.-F. Li, W.-Q. Liao, Z.-X. Wang, Q. Ye, and R.-G. Xiong, “Symmetry breaking in molecular ferroelectrics,” *Chem. Soc. Rev.*, vol. 45, no. 14, pp. 3811–3827, 2016.
- [96] “Piezoresponse Force Microscopy.” [Online]. Available: <https://www.asylumresearch.com/Applications/PFMAppNote/PFMAppNote.shtml>. [Accessed: 27-Mar-2017].
- [97] “Piezoelectric Force Microscopy (PFM).” [Online]. Available: <http://www.parkafm.com/index.php/park-spm-modes/dielectric-piezoelectric-properties/230-piezoelectric-force-microscopy-pfm>. [Accessed: 27-Mar-2017].
- [98] S. Foner, “Versatile and Sensitive Vibrating-Sample Magnetometer,” *Rev. Sci. Instrum.*, vol. 30, no. 7, pp. 548–557, Jul. 1959.
- [99] K. F. Wang, J.-M. Liu, and Z. F. Ren, “Multiferroicity: the coupling between magnetic and polarization orders,” *Adv. Phys.*, vol. 58, no. 4, pp. 321–448, 2009.
- [100] S. Iakovlev, C.-H. Solterbeck, M. Kuhnke, and M. Es-Souni, “Multiferroic BiFeO₃ thin films processed via chemical solution deposition: Structural and electrical characterization,” *J. Appl. Phys.*, vol. 97, no. 9, p. 94901, 2005.
- [101] R. E. Cohen, “Origin of ferroelectricity in perovskite oxides,” *Nature*, vol. 358, no. 6382, pp. 136–138, 1992.
- [102] G. A. Smolenskii and I. E. Chupis, “Ferroelectromagnets,” *Sov. Phys. Uspekhi*, vol. 25, no. 7, p. 475, 1982.

- [103] F. Kubel and H. Schmid, "Structure of a ferroelectric and ferroelastic monodomain crystal of the perovskite BiFeO_3 ," *Acta Crystallogr. Sect. B Struct. Sci.*, vol. 46, no. 6, pp. 698–702, 1990.
- [104] S. Gupta, A. Sharma, M. Tomar, V. Gupta, M. Pal, R. Guo, and A. Bhalla, "Piezoresponse force microscopy and vibrating sample magnetometer study of single phased Mn induced multiferroic BiFeO_3 thin film," *J. Appl. Phys.*, vol. 111, no. 6, p. 64110, 2012.
- [105] T. Zhao, S. B. Ogale, S. R. Shinde, R. Ramesh, R. Droopad, J. Yu, K. Eisenbeiser, and J. Misewich, "Colossal magnetoresistive manganite-based ferroelectric field-effect transistor on Si," *Appl. Phys. Lett.*, vol. 84, no. 5, pp. 750–752, 2004.
- [106] L. W. Martin, Y.-H. Chu, Q. Zhan, R. Ramesh, S.-J. Han, S. X. Wang, M. Warusawithana, and D. G. Schlom, "Room temperature exchange bias and spin valves based on $\text{BiFeO}_3/\text{SrRuO}_3/\text{SrTiO}_3/\text{Si}$ (001) heterostructures," *Appl. Phys. Lett.*, vol. 91, no. 17, p. 172513, 2007.
- [107] W. B. Luo, J. Zhu, H. Z. Zeng, X. W. Liao, H. Chen, W. L. Zhang, and Y. R. Li, "Effects of $\text{SrTiO}_3/\text{TiO}_2$ buffer layer on structural and electrical properties of BiFeO_3 thin films grown on GaN (0002)," *J. Appl. Phys.*, vol. 109, no. 10, p. 104108, 2011.
- [108] R. Chau, S. Datta, M. Doczy, B. Doyle, B. Jin, J. Kavalieros, A. Majumdar, M. Metz, and M. Radosavljevic, "Benchmarking nanotechnology for high-performance and low-power logic transistor applications," *Nanotechnology, IEEE Trans.*, vol. 4, no. 2, pp. 153–158, 2005.
- [109] G. Y. Gao, Z. B. Yang, W. Huang, H. Z. Zeng, Y. Wang, H. L. W. Chan, W. B. Wu, and J. H. Hao, "Heteroepitaxial growth and multiferroic properties of Mn-doped BiFeO_3 films on SrTiO_3 buffered III–V semiconductor GaAs," *J. Appl. Phys.*, vol. 114, no. 9, p. 94106, 2013.
- [110] W. Huang, J. J. Yang, G. Y. Gao, Y. Lei, J. Zhu, H. Z. Zeng, F. G. Zheng, and J. H. Hao, "Electrical transport and resistance switching characteristics of $\text{BiFeO}_3/\text{Nb}:\text{SrTiO}_3/\text{GaAs}$ heterostructure fabricated by pulsed laser deposition," *Appl. Phys. Lett.*, vol. 105, no. 6, p. 62904, 2014.
- [111] S. Y. Yang, J. Seidel, S. J. Byrnes, P. Shafer, C.-H. Yang, M. D. Rossell, P. Yu, Y.-H. Chu, J. F. Scott, and J. W. Ager, "Above-bandgap voltages from ferroelectric photovoltaic devices," *Nat. Nanotechnol.*, vol. 5, no. 2, pp. 143–147, 2010.
- [112] J. Gatabi, K. Lyon, S. Rahman, M. Caro, J. Rojas-Ramirez, J. Cott-Garcia, R. Droopad, and B. Lee, "Functional materials integrated on III–V semiconductors," *Microelectron. Eng.*, vol. 147, pp. 117–121, 2015.

- [113] R. Contreras-Guerrero, M. Edirisooriya, O. C. Noriega, and R. Droopad, “Interface properties of MBE grown epitaxial oxides on GaAs,” *J. Cryst. Growth*, vol. 378, pp. 238–242, 2013.
- [114] Y. Liang, J. Kulik, T. C. Eschrich, R. Droopad, Z. Yu, and P. Maniar, “Hetero-epitaxy of perovskite oxides on GaAs (001) by molecular beam epitaxy,” *Appl. Phys. Lett.*, vol. 85, no. 7, 2004.
- [115] Z. P. Wu, W. Huang, K. H. Wong, and J. H. Hao, “Structural and dielectric properties of epitaxial SrTiO₃ films grown directly on GaAs substrates by laser molecular beam epitaxy,” *J. Appl. Phys.*, vol. 104, no. 5, p. 54103, 2008.
- [116] F. Zavaliche, S. Y. Yang, T. Zhao, Y. H. Chu, M. P. Cruz, C. B. Eom, and R. Ramesh, “Multiferroic BiFeO₃ films: domain structure and polarization dynamics,” *Phase Transitions*, vol. 79, no. 12, pp. 991–1017, 2006.
- [117] H. Toupet, V. V Shvartsman, F. LeMarrec, P. Borisov, W. Kleemann, and M. Karkut, “Enhanced magnetization in BiFeO₃/BaTiO₃ multilayers: an interface effect?,” *Integr. Ferroelectr.*, vol. 100, no. 1, pp. 165–176, 2008.
- [118] S. Y. Yang, F. Zavaliche, L. Mohaddes-Ardabili, V. Vaithyanathan, D. G. Schlom, Y. J. Lee, Y. H. Chu, M. P. Cruz, Q. Zhan, and T. Zhao, “Metalorganic chemical vapor deposition of lead-free ferroelectric BiFeO₃ films for memory applications,” *Appl. Phys. Lett.*, vol. 87, no. 10, p. 102903, 2005.
- [119] Z. Quan, H. Hu, S. Xu, W. Liu, G. Fang, M. Li, and X. Zhao, “Surface chemical bonding states and ferroelectricity of Ce-doped BiFeO₃ thin films prepared by sol-gel process,” *J. sol-gel Sci. Technol.*, vol. 48, no. 3, pp. 261–266, 2008.
- [120] J. F. Moulder, J. Chastain, and R. C. King, “Handbook of X-ray photoelectron spectroscopy: a reference book of standard spectra for identification and interpretation of XPS data; Physical Electronics: Eden Prairie, MN, 1995,” *There is no Corresp. Rec. this Ref.*, 2000.
- [121] S. Lee and S. Kim, “Electrochemical synthesis and characterization of erbium oxide,” *Ceram. Int.*, vol. 42, no. 16, pp. 18425–18430, 2016.
- [122] R. P. Laughlin, D. A. Currie, R. Contreras-Guerrero, A. Dedigama, W. Priyantha, R. Droopad, N. Theodoropoulou, P. Gao, and X. Pan, “Magnetic and structural properties of BiFeO₃ thin films grown epitaxially on SrTiO₃/Si substrates,” *J. Appl. Phys.*, vol. 113, no. 17, p. 17D919, 2013.

- [123] P. Kharel, S. Talebi, B. Ramachandran, A. Dixit, V. M. Naik, M. B. Sahana, C. Sudakar, R. Naik, M. S. R. Rao, and G. Lawes, “Structural, magnetic, and electrical studies on polycrystalline transition-metal-doped BiFeO₃ thin films,” *J. Phys. Condens. Matter*, vol. 21, no. 3, p. 36001, 2008.
- [124] C. Ederer and N. A. Spaldin, “Effect of epitaxial strain on the spontaneous polarization of thin film ferroelectrics,” *Phys. Rev. Lett.*, vol. 95, no. 25, p. 257601, 2005.
- [125] D. H. A. Blank, G. J. H. M. Rijnders, G. Koster, and H. Rogalla, “A new approach in layer-by-layer growth of oxide materials by pulsed laser deposition,” *J. Electroceramics*, vol. 4, no. 2–3, pp. 311–318, 2000.
- [126] P.-X. Nie, Y.-P. Wang, Y. Yang, G.-L. Yuan, W. Li, and X.-T. Ren, “Epitaxial Growth and Multiferroic Properties of (001)-Oriented BiFeO₃-YMnO₃ Films,” *Energy Harvest. Syst.*, vol. 2, no. 3–4, pp. 157–162, 2015.
- [127] V. R. Palkar, D. C. Kundaliya, S. K. Malik, and S. Bhattacharya, “Magnetoelectricity at room temperature in the Bi_{0.9-x}Tb_xLa_{0.1}FeO₃ system,” *Phys. Rev. B*, vol. 69, no. 21, p. 212102, 2004.
- [128] J. A. Woollam, B. D. Johs, D. W. Doerr, and R. A. Christenson, “Ellipsometer.” Google Patents, 13-Dec-1994.
- [129] G. J. MacDougall, H. M. Christen, W. Siemons, M. D. Biegalski, J. L. Zarestky, S. Liang, E. Dagotto, and S. E. Nagler, “Antiferromagnetic transitions in tetragonal-like BiFeO₃,” *Phys. Rev. B*, vol. 85, no. 10, p. 100406, 2012.
- [130] J. F. Ihlefeld, N. J. Podraza, Z. K. Liu, R. C. Rai, X. Xu, T. Heeg, Y. B. Chen, J. Li, R. W. Collins, and J. L. Musfeldt, “Optical band gap of BiFeO₃ grown by molecular-beam epitaxy,” *Appl. Phys. Lett.*, vol. 92, no. 14, p. 142908, 2008.
- [131] S. R. Basu, L. W. Martin, Y. H. Chu, M. Gajek, R. Ramesh, R. C. Rai, X. Xu, and J. L. Musfeldt, “Photoconductivity in BiFeO₃ thin films,” *Appl. Phys. Lett.*, vol. 92, no. 9, p. 91905, 2008.
- [132] Y. Chu, Q. Zhan, L. W. Martin, M. P. Cruz, P. Yang, G. W. Pabst, F. Zavaliche, S. Yang, J. Zhang, and L. Chen, “Nanoscale domain control in multiferroic BiFeO₃ thin films,” *Adv. Mater.*, vol. 18, no. 17, pp. 2307–2311, 2006.
- [133] C. Himcinschi, I. Vrejoiu, M. Friedrich, L. Ding, C. Cobet, N. Esser, M. Alexe, and D. R. T. Zahn, “Optical characterisation of BiFeO₃ epitaxial thin films grown by pulsed-laser deposition,” *Phys. Status Solidi. C Curr. Top. Solid State Phys.*, vol. 7, no. 2, pp. 296–299, 2010.

- [134] M. Huijben, P. Yu, L. W. Martin, H. J. A. Molegraaf, Y. Chu, M. B. Holcomb, N. Balke, G. Rijnders, and R. Ramesh, “Ultrathin limit of exchange bias coupling at oxide multiferroic/ferromagnetic interfaces,” *Adv. Mater.*, vol. 25, no. 34, pp. 4739–4745, 2013.
- [135] A. Ohtomo and H. Y. Hwang, “A high-mobility electron gas at the $\text{LaAlO}_3/\text{SrTiO}_3$ heterointerface,” *Nature*, vol. 427, no. 6973, pp. 423–426, 2004.
- [136] K. Ueda, H. Tabata, and T. Kawai, “Atomic arrangement and magnetic properties of LaFeO_3 – LaMnO_3 artificial superlattices,” *Phys. Rev. B*, vol. 60, no. 18, p. R12561, 1999.
- [137] M. Kareev, S. Prosandeev, J. Liu, C. Gan, A. Kareev, J. W. Freeland, M. Xiao, and J. Chakhalian, “Atomic control and characterization of surface defect states of TiO_2 terminated SrTiO_3 single crystals,” *Appl. Phys. Lett.*, vol. 93, no. 6, p. 61909, 2008.
- [138] S. Valencia, A. Crassous, L. Bocher, V. Garcia, X. Moya, R. O. Cherifi, C. Deranlot, K. Bouzehouane, S. Fusil, and A. Zobelli, “Interface-induced room-temperature multiferroicity in BaTiO_3 ,” *Nat. Mater.*, vol. 10, no. 10, pp. 753–758, 2011.
- [139] P. Yu, J.-S. Lee, S. Okamoto, M. D. Rossell, M. Huijben, C.-H. Yang, Q. He, J. X. Zhang, S. Y. Yang, and M. J. Lee, “Interface Ferromagnetism and Orbital Reconstruction in BiFeO_3 – $\text{La}_{0.7}\text{Sr}_{0.3}\text{MnO}_3$ Heterostructures,” *Phys. Rev. Lett.*, vol. 105, no. 2, p. 27201, 2010.
- [140] S. M. Wu, S. A. Cybart, P. Yu, M. D. Rossell, J. X. Zhang, R. Ramesh, and R. C. Dynes, “Reversible electric control of exchange bias in a multiferroic field-effect device,” *Nat. Mater.*, vol. 9, no. 9, pp. 756–761, 2010.
- [141] S. M. Wu, S. A. Cybart, D. Yi, J. M. Parker, R. Ramesh, and R. C. Dynes, “Full electric control of exchange bias,” *Phys. Rev. Lett.*, vol. 110, no. 6, p. 67202, 2013.
- [142] J. Ma, J. Hu, Z. Li, and C. Nan, “Recent progress in multiferroic magnetoelectric composites: from bulk to thin films,” *Adv. Mater.*, vol. 23, no. 9, pp. 1062–1087, 2011.
- [143] S. S. Rao, J. T. Prater, F. Wu, C. T. Shelton, J.-P. Maria, and J. Narayan, “Interface magnetism in epitaxial BiFeO_3 – $\text{La}_{0.7}\text{Sr}_{0.3}\text{MnO}_3$ heterostructures integrated on $\text{Si}(100)$,” *Nano Lett.*, vol. 13, no. 12, pp. 5814–5821, 2013.
- [144] Y.-H. Chu, L. W. Martin, M. B. Holcomb, M. Gajek, S.-J. Han, Q. He, N. Balke, C.-H. Yang, D. Lee, and W. Hu, “Electric-field control of local ferromagnetism using a magnetoelectric multiferroic,” *Nat. Mater.*, vol. 7, no. 6, pp. 478–482, 2008.

- [145] S. Kundu, M. Clavel, P. Biswas, B. Chen, H.-C. Song, P. Kumar, N. N. Halder, M. K. Hudait, P. Banerji, and M. Sanghadasa, “Lead-free epitaxial ferroelectric material integration on semiconducting (100) Nb-doped SrTiO₃ for low-power non-volatile memory and efficient ultraviolet ray detection,” *Sci. Rep.*, vol. 5, 2015.
- [146] Z. Hu, Q. Li, M. Li, Q. Wang, Y. Zhu, X. Liu, X. Zhao, Y. Liu, and S. Dong, “Ferroelectric memristor based on Pt/BiFeO₃/Nb-doped SrTiO₃ heterostructure,” *Appl. Phys. Lett.*, vol. 102, no. 10, p. 102901, 2013.
- [147] S. Hong, T. Choi, J. H. Jeon, Y. Kim, H. Lee, H. Joo, I. Hwang, J. Kim, S. Kang, and S. V Kalinin, “Large Resistive Switching in Ferroelectric BiFeO₃ Nano-Island Based Switchable Diodes,” *Adv. Mater.*, vol. 25, no. 16, pp. 2339–2343, 2013.
- [148] S. Gao, C. Song, C. Chen, F. Zeng, and F. Pan, “Dynamic processes of resistive switching in metallic filament-based organic memory devices,” *J. Phys. Chem. C*, vol. 116, no. 33, pp. 17955–17959, 2012.
- [149] Y. Shuai, X. Ou, W. Luo, A. Mücklich, D. Bürger, S. Zhou, C. Wu, Y. Chen, W. Zhang, and M. Helm, “Key concepts behind forming-free resistive switching incorporated with rectifying transport properties,” *Sci. Rep.*, vol. 3, 2013.
- [150] N. Feng, H. Yu, L. Huang, W. Zhong, and Z. Shi, “Performance analysis of a magnetic-g geared linear permanent magnet generator for wave energy conversion,” in *Magnetics Conference (INTERMAG), 2015 IEEE*, 2015, p. 1.
- [151] P. Murugavel, J. H. Lee, J. Y. Jo, H. Y. Sim, J. S. Chung, Y. Jo, and M.-H. Jung, “Structure and ferroelectric properties of epitaxial (1-x)BiFeO₃-xBaTiO₃ solid solution films,” *J. Phys. Condens. Matter*, vol. 20, no. 41, p. 415208, 2008.
- [152] J. Dho, X. Qi, H. Kim, J. L. MacManus-Driscoll, and M. G. Blamire, “Large electric polarization and exchange bias in multiferroic BiFeO₃,” *Adv. Mater.*, vol. 18, no. 11, pp. 1445–1448, 2006.
- [153] C. Dubourdieu, J. Bruley, T. M. Arruda, A. Posadas, J. Jordan-Sweet, M. M. Frank, E. Cartier, D. J. Frank, S. V Kalinin, and A. A. Demkov, “Switching of ferroelectric polarization in epitaxial BaTiO₃ films on silicon without a conducting bottom electrode,” *Nat. Nanotechnol.*, vol. 8, no. 10, pp. 748–754, 2013.
- [154] J.-S. Lee, D. A. Arena, P. Yu, C. S. Nelson, R. Fan, C. J. Kinane, S. Langridge, M. D. Rossell, R. Ramesh, and C.-C. Kao, “Hidden magnetic configuration in epitaxial La_{1-x}Sr_xMnO₃ films,” *Phys. Rev. Lett.*, vol. 105, no. 25, p. 257204, 2010.
- [155] A. E. Berkowitz and K. Takano, “Exchange anisotropy—a review,” *J. Magn. Magn. Mater.*, vol. 200, no. 1, pp. 552–570, 1999.

- [156] K. D. Sung, Y. A. Park, M. S. Seo, Y. Jo, N. Hur, and J. H. Jung, “Observation of intriguing exchange bias in BiFeO₃ thin films,” *J. Appl. Phys.*, vol. 112, no. 3, p. 33915, 2012.
- [157] A. J. Millis, T. Darling, and A. Migliori, “Quantifying strain dependence in ‘colossal’ magnetoresistance manganites,” *J. Appl. Phys.*, vol. 83, no. 3, pp. 1588–1591, 1998.
- [158] M. Huijben, L. W. Martin, Y.-H. Chu, M. B. Holcomb, P. Yu, G. Rijnders, D. H. A. Blank, and R. Ramesh, “Critical thickness and orbital ordering in ultrathin La_{0.7}Sr_{0.3}MnO₃ films,” *Phys. Rev. B*, vol. 78, no. 9, p. 94413, 2008.
- [159] L. W. Martin, Y.-H. Chu, M. B. Holcomb, M. Huijben, P. Yu, S.-J. Han, D. Lee, S. X. Wang, and R. Ramesh, “Nanoscale control of exchange bias with BiFeO₃ thin films,” *Nano Lett.*, vol. 8, no. 7, pp. 2050–2055, 2008.
- [160] A. Y. Borisevich, H. J. Chang, M. Huijben, M. P. Oxley, S. Okamoto, M. K. Niranjani, J. D. Burton, E. Y. Tsybal, Y.-H. Chu, and P. Yu, “Suppression of octahedral tilts and associated changes in electronic properties at epitaxial oxide heterostructure interfaces,” *Phys. Rev. Lett.*, vol. 105, no. 8, p. 87204, 2010.
- [161] C. Wang, K. Jin, Z. Xu, L. Wang, C. Ge, H. Lu, H. Guo, M. He, and G. Yang, “Switchable diode effect and ferroelectric resistive switching in epitaxial BiFeO₃ thin films,” *Appl. Phys. Lett.*, vol. 98, no. 19, p. 192901, 2011.
- [162] A. Tsurumaki, H. Yamada, and A. Sawa, “Impact of Bi Deficiencies on Ferroelectric Resistive Switching Characteristics Observed at p-Type Schottky-Like Pt/Bi_{1-δ}FeO₃ Interfaces,” *Adv. Funct. Mater.*, vol. 22, no. 5, pp. 1040–1047, 2012.
- [163] T. L. Qu, Y. G. Zhao, D. Xie, J. P. Shi, Q. P. Chen, and T. L. Ren, “Resistance switching and white-light photovoltaic effects in BiFeO₃/Nb–SrTiO₃ heterojunctions,” *Appl. Phys. Lett.*, vol. 98, no. 17, p. 173507, 2011.
- [164] S. M. Jilani, T. D. Gamot, P. Banerji, and S. Chakraborty, “Studies on resistive switching characteristics of aluminum/graphene oxide/semiconductor nonvolatile memory cells,” *Carbon N. Y.*, vol. 64, pp. 187–196, 2013.
- [165] S. Singh, J. Xiong, A. P. Chen, M. R. Fitzsimmons, and Q. X. Jia, “Field-dependent magnetization of BiFeO₃ in an ultrathin La_{0.7}Sr_{0.3}MnO₃/BiFeO₃ superlattice,” *Phys. Rev. B*, vol. 92, no. 22, p. 224405, 2015.
- [166] D. Sando, P. Hermet, J. Allibe, J. Bourderionnet, S. Fusil, C. Carrétéro, E. Jacquet, J.-C. Mage, D. Dolfi, and A. Barthélémy, “Linear electro-optic effect in multiferroic BiFeO₃ thin films,” *Phys. Rev. B*, vol. 89, no. 19, p. 195106, 2014.

- [167] M. S. Rahman, S. Ghose, L. Hong, P. Dhungana, A. Fahami, J. R. Gatabi, J. S. Rojas-Ramirez, A. Zakhidov, R. F. Klie, and R. K. Pandey, "Integration of BiFeO₃/La_{0.7}Sr_{0.3}MnO₃ heterostructures with III–V semiconductors for low-power non-volatile memory and multiferroic field effect transistors," *J. Mater. Chem. C*, vol. 4, no. 43, pp. 10386–10394, 2016.
- [168] M. S. Rahman, S. Ghose, J. R. Gatabi, J. S. Rojas-Ramirez, R. K. Pandey, and R. Droopad, "Heteroepitaxial growth and characterization of BiFeO₃ thin films on GaAs," *Mater. Res. Express*, vol. 3, no. 10, p. 106408, 2016.
- [169] E. Choi, J. E. Kleibeuker, T. Fix, J. Xiong, C. J. Kinane, D. Arena, S. Langridge, A. Chen, Z. Bi, and J. H. Lee, "Interface-Coupled BiFeO₃/BiMnO₃ Superlattices with Magnetic Transition Temperature up to 410 K," *Adv. Mater. Interfaces*, 2016.
- [170] N. Feng, W. Mi, X. Wang, Y. Cheng, and U. Schwingenschlögl, "Superior Properties of Energetically Stable La_{2/3}Sr_{1/3}MnO₃/Tetragonal BiFeO₃ Multiferroic Superlattices," *ACS Appl. Mater. Interfaces*, vol. 7, no. 19, pp. 10612–10616, 2015.
- [171] S. Okamoto, "Magnetic interaction at an interface between manganite and other transition metal oxides," *Phys. Rev. B*, vol. 82, no. 2, p. 24427, 2010.
- [172] S. J. May, P. J. Ryan, J. L. Robertson, J.-W. Kim, T. S. Santos, E. Karapetrova, J. L. Zarestky, X. Zhai, S. G. E. Te Velthuis, and J. N. Eckstein, "Enhanced ordering temperatures in antiferromagnetic manganite superlattices," *Nat. Mater.*, vol. 8, no. 11, pp. 892–897, 2009.
- [173] H. Y. Hwang, Y. Iwasa, M. Kawasaki, B. Keimer, N. Nagaosa, and Y. Tokura, "Emergent phenomena at oxide interfaces," *Nat. Mater.*, vol. 11, no. 2, pp. 103–113, 2012.
- [174] J. Chakhalian, J. W. Freeland, H.-U. Habermeier, G. Cristiani, G. Khaliullin, M. Van Veenendaal, and B. Keimer, "Orbital reconstruction and covalent bonding at an oxide interface," *Science (80-.)*, vol. 318, no. 5853, pp. 1114–1117, 2007.
- [175] Y. F. Tian, O. I. Lebedev, V. V Roddatis, W. N. Lin, J. F. Ding, S. J. Hu, S. S. Yan, and T. Wu, "Interfacial magnetic coupling in ultrathin all-manganite La_{0.7}Sr_{0.3}MnO₃-TbMnO₃ superlattices," *Appl. Phys. Lett.*, vol. 104, no. 15, p. 152404, 2014.
- [176] M. El Marssi, F. Le Marrec, I. A. Lukyanchuk, and M. G. Karkut, "Ferroelectric transition in an epitaxial barium titanate thin film: Raman spectroscopy and x-ray diffraction study," *J. Appl. Phys.*, vol. 94, no. 5, pp. 3307–3312, 2003.

- [177] M. Liu, C. Ma, G. Collins, J. Liu, C. Chen, A. D. Alemayehu, G. Subramanyam, Y. Ding, J. Chen, and C. Dai, “Ferroelectric BaTiO₃/SrTiO₃ multilayered thin films for room-temperature tunable microwave elements,” *Nanoscale Res. Lett.*, vol. 8, no. 1, p. 338, 2013.
- [178] M. Liu, C. Ma, G. Collins, J. Liu, C. Chen, C. Dai, Y. Lin, L. Shui, F. Xiang, and H. Wang, “Interface engineered BaTiO₃/SrTiO₃ heterostructures with optimized high-frequency dielectric properties,” *ACS Appl. Mater. Interfaces*, vol. 4, no. 11, pp. 5761–5765, 2012.
- [179] X. N. Zhu, X. Xu, Z. Harrell, R. Guo, A. S. Bhalla, M. Zhang, J. Jiang, C. Chen, and X. M. Chen, “Ferroelectric domain structure evolution in Ba(Zr_{0.1}Ti_{0.9})O₃/(Ba_{0.75}Ca_{0.25})TiO₃ heterostructures,” *RSC Adv.*, vol. 5, no. 81, pp. 65811–65817, 2015.
- [180] X. N. Zhu, T. T. Gao, X. Xu, W. Z. Liang, Y. Lin, C. Chen, and X. M. Chen, “Piezoelectric and Dielectric Properties of Multilayered BaTiO₃/(Ba,Ca)TiO₃/CaTiO₃ Thin Films,” *ACS Appl. Mater. Interfaces*, vol. 8, no. 34, pp. 22309–22315, 2016.
- [181] M. Vafaei, S. Finizio, H. Deniz, D. Hesse, H. Zabel, G. Jakob, and M. Kläui, “The effect of interface roughness on exchange bias in La_{0.7}Sr_{0.3}MnO₃–BiFeO₃ heterostructures,” *Appl. Phys. Lett.*, vol. 108, no. 7, p. 72401, 2016.
- [182] S. Brück, G. Schütz, E. Goering, X. Ji, and K. M. Krishnan, “Uncompensated moments in the MnPd/Fe exchange bias system,” *Phys. Rev. Lett.*, vol. 101, no. 12, p. 126402, 2008.
- [183] S. Dong, K. Yamauchi, S. Yunoki, R. Yu, S. Liang, A. Moreo, J.-M. Liu, S. Picozzi, and E. Dagotto, “Exchange bias driven by the Dzyaloshinskii-Moriya interaction and ferroelectric polarization at G-type antiferromagnetic perovskite interfaces,” *Phys. Rev. Lett.*, vol. 103, no. 12, p. 127201, 2009.
- [184] D. Mauri, E. Kay, D. Scholl, and J. K. Howard, “Novel method for determining the anisotropy constant of MnFe in a NiFe/MnFe sandwich,” *J. Appl. Phys.*, vol. 62, no. 7, pp. 2929–2932, 1987.
- [185] S. N. Jammalamadaka, J. Vanacken, and V. V Moshchalkov, “Resistive switching in ultra-thin La_{0.7}Sr_{0.3}MnO₃/SrRuO₃ superlattices,” *Appl. Phys. Lett.*, vol. 105, no. 3, p. 33505, 2014.
- [186] N. Z. Haron and S. Hamdioui, “Why is CMOS scaling coming to an END?,” in *Design and Test Workshop, 2008. IDT 2008. 3rd International*, 2008, pp. 98–103.

- [187] R. Oligschlaeger, R. Waser, R. Meyer, S. Karthäuser, and R. Dittmann, “Resistive switching and data reliability of epitaxial (Ba,Sr)TiO₃ thin films,” *Appl. Phys. Lett.*, vol. 88, no. 4, p. 42901, 2006.
- [188] R. Waser and M. Aono, “Nanoionics-based resistive switching memories,” *Nat. Mater.*, vol. 6, no. 11, pp. 833–840, 2007.
- [189] J. M. Luo, S. P. Lin, Y. Zheng, and B. Wang, “Nonpolar resistive switching in Mn-doped BiFeO₃ thin films by chemical solution deposition,” *Appl. Phys. Lett.*, vol. 101, no. 6, p. 62902, 2012.
- [190] H. Y. Jeong, J. Y. Lee, S.-Y. Choi, and J. W. Kim, “Microscopic origin of bipolar resistive switching of nanoscale titanium oxide thin films,” *Appl. Phys. Lett.*, vol. 95, no. 16, p. 162108, 2009.
- [191] J. Choi, J.-S. Kim, I. Hwang, S. Hong, I.-S. Byun, S.-W. Lee, S.-O. Kang, and B. H. Park, “Different nonvolatile memory effects in epitaxial Pt/PbZr_{0.3}Ti_{0.7}O₃/LSCO heterostructures,” *Appl. Phys. Lett.*, vol. 96, no. 26, p. 262113, 2010.
- [192] M. Y. Zhuravlev, S. S. Jaswal, E. Y. Tsymbal, and R. F. Sabirianov, “Ferroelectric switch for spin injection,” *Appl. Phys. Lett.*, vol. 87, no. 22, p. 222114, 2005.
- [193] V. Laukhin, V. Skumryev, X. Martí, D. Hrabovsky, F. Sánchez, M. V García-Cuenca, C. Ferrater, M. Varela, U. Lüders, and J. F. Bobo, “Electric-field control of exchange bias in multiferroic epitaxial heterostructures,” *Phys. Rev. Lett.*, vol. 97, no. 22, p. 227201, 2006.
- [194] X. He, Y. Wang, N. Wu, A. N. Caruso, E. Vescovo, K. D. Belashchenko, P. A. Dowben, and C. Binek, “Robust isothermal electric control of exchange bias at room temperature,” *Nat. Mater.*, vol. 9, no. 7, pp. 579–585, 2010.